ANALYSIS AND DESIGN OF A HORIZONTAL VIBRATION ISOLATOR HAVING ADJUSTABLE QUASI-ZERO STIFFNESS ALONG MULTIPLE AXES

by

Mehmet Utku Demir

B.S., Mechanical Engineering, Boğaziçi University, 2017

Submitted to the Institute for Graduate Studies in

Science and Engineering in partial fulfillment of

The requirements for the degree of

Master of Science

Graduate Program in Mechanical Engineering

Boğaziçi University

2021

ACKNOWLEDGEMENT

Foremost, I would like to express my deep gratitude to my advisor Prof. Çetin Yılmaz for showing me great patience, devotion and understanding during my entire research studies. I would like to thank him for guiding me through this long marathon with his endless motivation, enthusiasm, immense knowledge and innovative ideas.

Besides, I would like to thank Assoc. Prof. Evren Samur and Assist. Prof. Polat Şendur for giving their precious time to read and evaluate my thesis.

I am grateful to my beloved family for always giving me their emotional support. I owe a lot to my dear mother Filiz Demir and my dear father Erdoğan Demir for completing this thesis.

I am also grateful to Hilal Arslan for her continuous support, motivation, patience and devotion to me during my entire research studies. Finally, I would like to thank to my friends Esra İlke Albar, İlhan Umur Ayberk and Adil Han Orta for their support and encouragement.

This study was supported by TUBITAK with Grant Number 218M475.

ABSTRACT

ANALYSIS AND DESIGN OF A HORIZONTAL VIBRATION ISOLATOR HAVING ADJUSTABLE QUASI-ZERO STIFFNESS ALONG MULTIPLE AXES

In this thesis, stiffness adjustment mechanisms are developed to tune the horizontal (parallel to the ground) stiffness of vibration isolation systems to quasi-zero values along three axes (translational stiffness in the horizontal x and y axes, torsional stiffness in the vertical z-axis) depending on the payload carried. When the elastic beams that support the payload weight are placed in the direction of gravity, the horizontal stiffness of the system decreases as the payload mass increases. Hence, the horizontal natural frequencies of the system decrease, and the isolation performance of the system at low frequencies increases. However, when the supported payload mass decreases, the opposite case occurs. In this study, mechanisms that separately adjust the translational and torsional stiffness are developed so that the natural frequencies are kept at low and constant values even if the payload changes. The developed wire tension mechanism adjusts the translational and torsional stiffness together, while the developed slide mechanism adjusts the torsional stiffness independently from the translational stiffness. Besides, since these mechanisms operate without friction, the isolation bandwidth of the system is very large. To increase the upper limit of the bandwidth above 100 Hz that most systems in the literature cannot surpass, the elastic beams are created with a unique design. Analytical and finite element models show that the system can operate at low frequencies, and a large bandwidth is obtained. The results of these models are validated by experiments. After the design parameters are optimized, the experimental studies performed on the produced system show that the translational and torsional natural frequencies can be adjusted between 0.5 Hz and 1.5 Hz, and the upper limit of the isolation bandwidth can be increased above 100 Hz.

ÖZET

ÇOK EKSENDE SIFIRA YAKIN AYARLANABİLİR DİRENGENLİĞE SAHİP YATAY TİTREŞİM YALITIM SİSTEMİNİN ANALİZİ VE TASARIMI

Bu tezde, titreşim yalıtım sistemlerinin yatay (yere paralel) direngenliğini taşınan yüke bağlı olarak üç eksende birden (yatay x ve y eksenlerinde öteleme direngenliği, dikey z ekseninde burulma direngenliği) sıfıra yakın değerlere ayarlamak amacıyla direngenlik ayar mekanizmaları geliştirilmiştir. Hedefteki yükün taşınması için kullanılan elastik kirişler yerçekimi doğrultusunda yerleştirildiğinde, sistemin yatay direngenliği taşınan yük kütlesi arttıkça azalmaktadır. Bu sayede, sistemin yatay doğal frekansları azalarak sistemin düşük frekanslardaki yalıtım performansı artmaktadır. Öte yandan, desteklenen yük kütlesi azaldığında, tam tersi bir durum ortaya çıkmaktadır. Bu çalışmada, taşınan yüke bağlı olarak sistemin öteleme ve burulma direngenliğini ayrı ayrı ayarlayan mekanizmalar geliştirilerek doğal frekansların düşük ve sabit değerlerde tutlması sağlanmıştır. Geliştirilen tel gerdirme mekanizması, öteleme ve burulma direngenliklerinin birlikte ayarlayabilirken, geliştirilen kızak mekanizması burulma direngenliğinin öteleme direngenliğinden bağımsız olarak ayarlayabilmektedir. Ayrıca bu mekanizmalar sürtünmesiz bir şekilde çalıştığı için sistemin yalıtım bant genişliğini daraltmamaktadır. Sistemin bant genişliğinin üst limitini literatürdeki çoğu sistemin geçemediği 100 Hz üst limitinin üzerine çıkarmak için elastik kirişler özgün bir tasarımla oluşturulmuştur. Analitik ve sonlu elemanlar modelleri, taşınan yük kütlesi değişse bile sistemin düşük frekanslarda ve büyük bir bant genişliğinde çalışabildiğini göstermektedir. Bu modellerin sonuçları deneylerle doğrulanmıştır. Sistemin tasarım parametreleri eniyilendikten sonra, üretilen sistem üzerinde yapılan deneyler, her yükleme koşulunda öteleme ve burulma doğal frekanslarının 0.5 Hz ile 1.5 Hz arasına ayarlanabildiğini ve yalıtım bant genişliğinin üst limitinin 100 Hz'in üzerine çıkarılabildiğini göstermektedir.

TABLE OF CONTENTS

LIST OF FIGURES

LIST OF TABLES

LIST OF SYMBOLS

A	Cross-sectional area of an elastic uniform beam
A_i	Cross-sectional area of the section i of an elastic stepped beam
A_s	Cross-sectional area of the tension wire
c	Wave speed in the tension wire
E	Young's modulus of an elastic uniform beam
E_i	Young's modulus of the section i of an elastic stepped beam
E_k	Kinetic energy of a horizontal-motion isolator with elastic uniform beams
E_p	Potential energy of a horizontal-motion isolator with elastic uniform beams
$f_{s,n}$	n^{th} natural frequency of the tension wire in Hertz
$F(t)$	Harmonic driving force
g	Gravitational acceleration
G	Shear modulus of an elastic uniform beam
G_i	Shear modulus of the section i of an elastic stepped beam
I_p	Cross-sectional polar moment of inertia of an elastic uniform beam
I_{pi}	Cross-sectional polar moment of inertia of the section i of an elastic stepped beam
J_0	Mass polar moment of inertia of the top platform
J_p	Mass polar moment of inertia of a payload
k_{xy}	Translational stiffness of a horizontal-motion isolator
k_{zz}	Torsional stiffness of a horizontal-motion isolator

l	Length of an elastic uniform and stepped beam
l_i	Length of the section i of an elastic stepped beam
l_s	Length of the tension wire
$M(t)$	Harmonic driving moment
m_0	Top platform mass
m_{max}	Maximum payload carrying capacity
m_p	Payload mass
P	Payload weight
P_0	Top platform weight
$P_{cr,n}$	n^{th} critical buckling load of horizontal-motion isolators
r	Radius of an elastic uniform and stepped beam
$r_{i,o}$	Outer radius of the section i of an elastic stepped beam
$r_{i,i}$	Inner radius of the section i of an elastic stepped beam
r_s	Radius of the tension wire
$\bar{r}$	Radial distance of elastic uniform and stepped beams to the central axis
t	Thickness of the thin-walled cylinders
T	Tension force in the wire
$T_{cr,xy}$	Lateral critical buckling tension of horizontal-motion isolators
$T_{cr,zz}$	Torsional critical buckling tension of horizontal-motion isolators
$T_{cr,u}$	Upper critical buckling tension of horizontal-motion isolators
$\bar{T}_{cr,xy}$	Ratio of the numerical to analytical lateral critical buckling tension of horizontal-motion isolators

$\bar{T}_{cr,zz}$	Ratio of the numerical to analytical torsional critical buckling tension of horizontal-motion isolators
T_{max}	Maximum tension force to buckle horizontal-motion isolators
T_o	Optimum tension force to adjust the lowest natural frequency of horizontal-motion isolators to 0.5 Hz
y	Lateral deflection of an elastic uniform beam along its longitudinal axis
y_i	Lateral deflection of the section i of an elastic stepped beam along its longitudinal axis
Y	Maximum amplitude of the forced response for translational vibrations
δ	Lateral deflection of the top platform
δ_{max}	Maximum allowable lateral deflection of the top platform
Θ	Maximum amplitude of the forced response for torsional vibrations
κ	Cross-sectional radius of gyration of an elastic uniform beam
κ_0	Radius of gyration of the top platform
ρ	Density of an elastic uniform beam
ρ_i	Density of the section i of an elastic stepped beam
$\sigma_{i,max}$	Maximum axial stress in the section i of an elastic stepped beam
$\sigma_{s,max}$	Maximum axial stress in the tension wire
ϕ	Angular deflection of an elastic uniform beam along its longitudinal axis
ϕ_i	Angular deflection of the section i of an elastic stepped beam along its longitudinal axis
ω	Excitation frequency
ω_n	n^{th} bending natural frequency of an elastic uniform beam

$\omega_{s,n}$	n^{th} natural frequency of the tension wire in radian
ω_{xy}	Translational natural frequency of horizontal-motion isolators
ω_u	Upper natural frequency of horizontal-motion isolators
ω_{zz}	Torsional natural frequency of horizontal-motion isolators

LIST OF ACCRONYMS / ABBREVIATIONS

FE	Finite Element
FEM	Finite Element Model
QZS	Quasi-Zero-Stiffness

1. INTRODUCTION

1.1. Low-Frequency Vibration Isolation

In order to ensure that vibration-sensitive measuring devices used in industrial activities and laboratory studies can operate without being affected by seismic (ground) motions, low-frequency vibration isolation systems have been proposed in various designs [1-7]. These systems can be used to protect instruments such as gravitational wave detectors, seismographs, laser Doppler vibrometers and atomic force microscopes from low frequencies [1-3]. They can also be used to be pre-isolators for further stages of isolation process [4-5]. To achieve high isolation performance at low frequencies, their natural frequencies can be adjusted to very low values in horizontal [6], vertical [7] and horizontal-vertical [8] directions.

In the most general sense, vibration isolators can be categorized as linear or nonlinear systems. While the stiffness of a linear system is constant at static displacements, the stiffness of a nonlinear system varies according to the amount of static displacements. In order for linear isolation elements such as steel coil springs or rubber bushings to firmly support the target object (payload), the elements must be hard (high stiffness) but also soft (low stiffness) for adequate isolation at low frequencies. To provide an effective isolation, the natural frequency ω_n of the mass-spring system must be much lower than the external excitation frequencies ω ($\sqrt{2}\omega_n \ll \omega$). In a linear system, when the stiffness is low, the static displacement is large at nominal load. On the other hand, although stiffness is low in a nonlinear system, static displacement can be low at nominal load. This contrast has been one of the main reasons for the development of nonlinear vibration isolation systems [9-14]. These nonlinear systems, which can operate at very low frequencies, are known to have quasi-zero-stiffness (QZS). In nonlinear vibration isolation systems with QZS, there is a sub-system that generally exhibits positive stiffness and another sub-system with negative

stiffness. With the combination of these two sub-systems, the overall stiffness of the system can be made quasi-zero at nominal loads [15-16].

QZS isolators can be classified according to whether they are active, semi-active (adaptive) or passive systems. There are different studies in the literature for active [17-21] or semi-active [22-24] QZS systems that aim to stabilize payloads at equilibrium positions and to adjust the stiffness at varying nominal loads. However, active or semi-active systems require an external energy source to operate, and their structures are more complex and expensive than passive systems. Compared to active or semi-active QZS isolators, passive QZS isolators are more preferred in applications where cost and reliability are important [25]. Passive QZS isolators can be categorized into different classes according to their designs. Pre-loaded oblique spring mechanisms [26-28], flexure-based spring mechanisms [29], cam-roller mechanisms [30-32], ball-roller mechanisms [33], buckled beam mechanisms [34,35,36], passive magnetic mechanisms [37-39] and scissors mechanisms [40] can be found in the literature. In addition, negative stiffness systems including pre-loaded leaf springs [8], buckled beams [41] and beam-pulley mechanisms [42] are also available in vibration isolator designs.

Most QZS isolators operate in one direction [27,28,43-47]. However, multi-axis (3 or 6) vibration isolators are needed to isolate vibrations in multiple directions in engineering fields such as high technology manufacturing techniques or micro-vibration control in satellites and space shuttles. Active [18,20,21], semi-active [23] and passive [48-51] systems can be given as examples of studies that show quasi-zero stiffness in multiple directions. However, most multi-axis QZS isolators have articulated (jointed) mechanisms that lead to many resonances at low frequencies due to friction and backlash in the joints. Although the stiffness can be adjusted in these systems, their isolation performance at low frequencies may not be satisfactory due to these resonance peaks, and their potential to be used as low-frequency vibration isolators is reduced.

Multi-axis QSZ vibration isolation systems produced by Minus K do not have joints that create friction [8,52] such that they can operate in very wide frequency ranges. The frequency spectrums of these systems for vertical (along gravity) and horizontal (parallel to ground) vibrations show that they can work at frequencies ranging from 0.5 Hz to 100 Hz. However, they have QZS adjustment mechanisms that only work in the vertical direction. Although the vertical natural frequencies of the system can be tuned to very low and constant values when the supported payload mass changes, the horizontal natural frequencies cannot be adjusted with respect to the payloads. Hence, the horizontal natural frequencies can be decreased to 0.5 Hz only when the systems support large payload masses which are close to the upper limits of their payload carrying capacities.

Recently, Minus K has developed a new vibration isolation system that has horizontal and vertical QZS adjustment mechanisms [53]. The horizontal stiffness of the system is created by the payload-bearing helical spring at the center of the system and vertically oriented elastic stepped beams. The horizontal stiffness is adjusted by axially compressing the stepped beams from their upper ends by means of helical springs that are compressed by turning screw mechanisms. Thus, the positive horizontal stiffness of the payload-bearing spring is reduced by the negative horizontal stiffness of the beams. As a result, the quasi-zero stiffness condition can be achieved in the horizontal directions.

1.2. Isolation Bandwidth Maximization Methods

Figure 1.1(a) shows a horizontal-motion isolator consisting of two elastic uniform beams. When the isolator vibrates horizontally along the x-axis under the action of vertical forces P as shown in Figure 1.1(b), the top platform remains parallel to ground during these vibrations, and the beams can be considered to have clamped-sliding boundary conditions as shown in Figure 1.1(c).

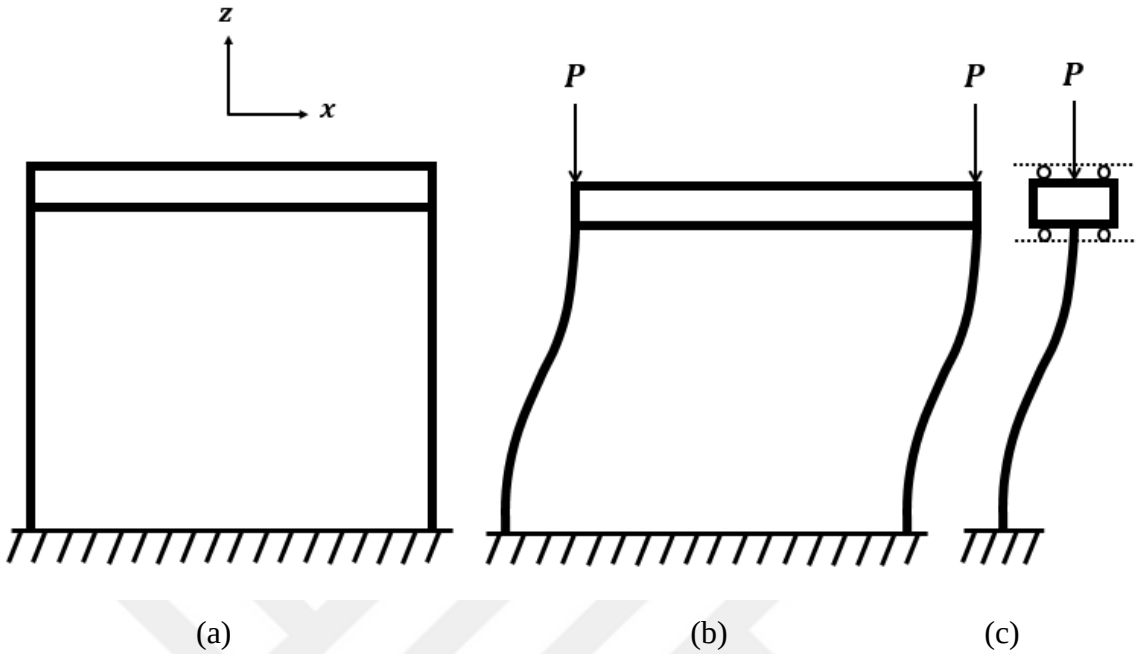

Figure 1. 1. (a) A horizontal-motion isolator consisting of two elastic uniform beams, (b) Horizontal vibration of the isolator under the action of vertical forces P, (c) The clamped-sliding boundary conditions of each beam due to the lateral vibration of the isolator.

If gravity is not taken into account, the general expression for the horizontal natural frequencies of the isolator can be written as [54]

$$\omega_n = {\beta_n}^2 \sqrt{\frac{EI}{\rho A}} \sqrt{1 - \frac{P}{P_{cr,n}}} \tag{1.1}$$

where $n = 1,2,3, \ldots$. In this equation, β_n is a constant depending on the boundary conditions and length l of the beams, EI is the flexural rigidity of the beams, ρA is the mass per unit length of the beams, and $P_{cr,n}$ is the n^{th} critical buckling load of the beams. From Euler's Theory of Column Buckling, it can be found that $P_{cr,n}$ can be written as

$$P_{cr,n} = n^2\pi^2 EI/l^2 \tag{1.2}$$

When $P = P_{cr,1}$, the isolator achieves horizontal quasi-zero-stiffness, and it can be found from Equation 1.1 that $\omega_1 = 0$. For stability purposes, P should be slightly less than $P_{cr,1}$ to achieve very low values of ω_1. When this occurs, the isolator can achieve good vibration isolation performance at low frequencies. To maximize the isolation bandwidth of the isolator, it is necessary to minimize the ratio ω_1/ω_2. Hence, from Equation 1.1, it can be found that

$$\frac{\omega_1}{\omega_2} = \left(\frac{\beta_1}{\beta_2}\right)^2 \sqrt{\left(\frac{P_{cr,2}}{1}\right)\left(\frac{P_{cr,1}-P}{P_{cr,2}-P}\right)} \tag{1.3}$$

In order for the isolator to be in a stable condition, the lowest value of ω_1 can be chosen as 0.5 Hz. Hence, the load P at which $\omega_1 = 0.5$ Hz can be found from Equation 1.1 as

$$P = P_{cr,1}\left(1 - \frac{\pi^2}{{\beta_1}^4}\frac{\rho A}{EI}\right) \tag{1.4}$$

If this value of P is substituted into Equation 1.1, ω_2 becomes

$$\omega_2 = {\beta_2}^2\sqrt{\frac{3EI}{4\rho A} + \frac{\pi^2}{4{\beta_1}^4}} \tag{1.5}$$

As a result, ω_1/ω_2 can be found as

$$\omega_1/\omega_2 = 1/({\beta_2}^2\sqrt{\frac{EI}{\rho A} + \frac{\pi^2}{{\beta_1}^4}}) \tag{1.6}$$

From this equation, it can be concluded that in order to minimize the ratio ω_1/ω_2, the ratio $EI/\rho A$ must be increased. If the same material is used for the beams, then the ratio E/ρ becomes constant, and the ratio ω_1/ω_2 only depends on the ratio I/A where I is the cross-sectional moment of inertia, and A is the cross-sectional area of the beam. The square root of this ratio can be defined as the cross-sectional radius of gyration of the beam denoted by κ. For a solid circular cross-section, $A = \pi r^2$ and $I = \pi r^4/4$ such that $\kappa = \sqrt{I/A} = 0.50r$. If a hollow circular cross-section is used such that the shell thickness t of the beam is $t = cr_d$ where r_d is the outer radius of the beam and where $0 < c < 1$, then $A = \pi({r_d}^2 - (r_d - cr_d)^2)$ and $I = \pi({r_d}^4 - (r_d - cr_d)^4)/4$. Hence, κ becomes

$$\kappa = \frac{r_d}{2}\sqrt{c^2 - 2c + 2} \tag{1.7}$$

If $r_d = r$ and $c = 0.2$, then it becomes that $\kappa = 0.82r$ which is greater than $\kappa = 0.50r$ for the previous case. From this result, it can be concluded that by increasing κ, the isolation bandwidth can be increased. However, when this occurs, the maximum payload bearing capacity of the isolator decreases because of a decrease in $P_{cr,1}$. Besides, if the beams have a hollow circular cross-section, the stress magnitudes at the ends of the beams might approach the yield strength of the beams. Consequently, while it is desired to increase the isolation bandwidth, it is also necessary to keep the maximum payload bearing capacity high and also to keep the stress magnitudes well below the yield strength. It can be seen that if stepped beams are used instead of uniform beams, the isolator can have a greater isolation bandwidth, greater maximum payload bearing capacity and lower stress magnitudes at the ends of the beams. In Chapter 2, the analytical models for the isolators with uniform and stepped beams are given to compare their isolation bandwidths.

If the horizontal-motion isolator is under the action of a payload weight $m_p g$ as shown in Figure 1.2, then the vertical load P in Figure 1.1(b) can be considered as $P = m_p g/2$. When ω_1 is calculated from Equation 1.1, the payload mass m_p is not included in the overall

inertia of the isolator. If it is taken into account, then ω_1 can be assumed to be proportional to

$$\omega_1 \propto \sqrt{\frac{k_0}{m_p}}\sqrt{1-\frac{m_p g/2}{P_{cr,1}}} \tag{1.8}$$

where k_0 is the horizontal stiffness of the isolator when there is no axial load on it. It can be seen from this equation that for smaller m_p values, ω_1 becomes larger, and the isolation performance of the isolator deteriorates at low frequencies. In order to keep ω_1 at low and constant values at smaller m_p values, the horizontal stiffness of the isolator must be decreased. Hence, it is necessary to adjust the horizontal stiffness with respect to changing m_p values. In Chapter 2, the proposed horizontal stiffness adjustment mechanism is applied to the isolators with elastic uniform and elastic stepped beams, and the first two horizontal natural frequencies of the isolators are derived to determine the isolation performances of them in the analytical models.

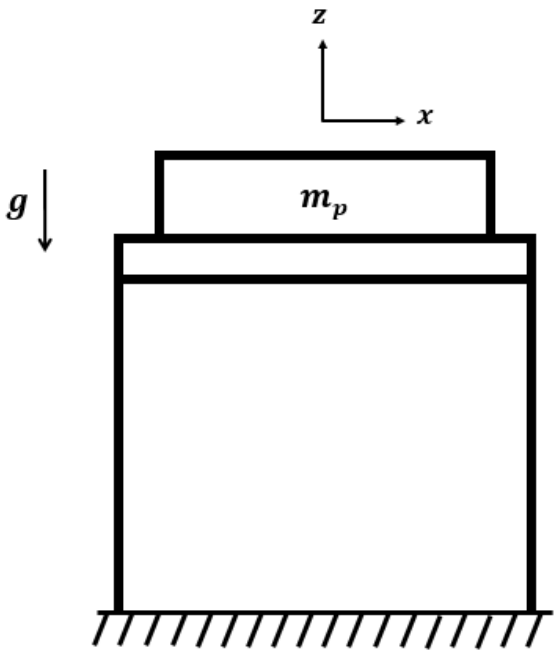

Figure 1. 2. A horizontal-motion isolator under the action of a payload mass m_p when gravity is taken into account.

1.3. Motivation and Research Objective

In this thesis, horizontal stiffness adjustment mechanisms are developed to achieve high isolation performance at low frequencies even if the payload mass supported by a horizontal-motion isolator changes. If the horizontal stiffness of the system can be adjusted with respect to the payload mass supported, the isolation performance of the system can be maintained at smaller payload masses by decreasing the stiffness of the system. It is also important that the system operates without friction to have high isolation performance at low frequencies. The motivations behind this study and the contributions to the literature can be summarized as follows:

- In the literature, although most vertical-motion isolators have stiffness adjustment mechanisms, the vast majority of horizontal-motion isolators have not been designed with these mechanisms. Using the novel wire tension mechanism, the horizontal stiffness of the system can be manually adjusted to quasi-zero values in three axes (translational stiffness in the horizontal x and y axes and torsional stiffness about the vertical z axis) with respect to the payload mass supported. In this way, it is provided that the system can isolate vibrations at very low frequencies in these axes.

- When the translational and torsional natural frequencies are adjusted by the wire tension mechanism, the torsional natural frequency can be further adjusted independently from the translational natural frequencies by using the novel slide mechanism which only changes the torsional stiffness of the system. This two-stage stiffness tuning feature enables that the translational and torsional natural frequencies can be kept very close to each other.

- The isolation bandwidth of the system is increased by using the novel elastic beams with variable cross-sectional area. Since the system works without friction, resonances resulting from friction and backlash in the joints are not observed within the isolation bandwidth. Hence, the system has a very large isolation bandwidth compared to systems in the literature and industry.

- The system can be used to protect mechanical, optical and electronic measuring devices sensitive to ground vibrations at low frequencies without using any external energy source in industrial activities and laboratory studies.

2. PROPOSED WIRE TENSION MECHANISM FOR HORIZONTAL-MOTION ISOLATORS

This chapter consists of three main sections. In Section 2.1, the analytical models are developed to investigate the relationship between the horizontal natural frequencies ω_x, ω_y and ω_{zz} and the wire tension force T applied by the tension mechanism. Then, in Section 2.2, the finite element models (FEM) are developed to validate the analytical results. Finally, in Section 2.3, experimental studies are performed on a prototype isolator to validate the analytical and numerical results. The analytical models focus on two different types of horizontal-motion isolators. While the first system is designed with elastic uniform beams (see Figure 2.1), the second system is designed with elastic stepped beams (see Figure 2.2). These systems are designed with different types of elastic beams in order to compare their isolation bandwidths at low frequencies. Figure 2.1 shows that there are three elastic beams and a wire in the center whose tension can be adjusted.

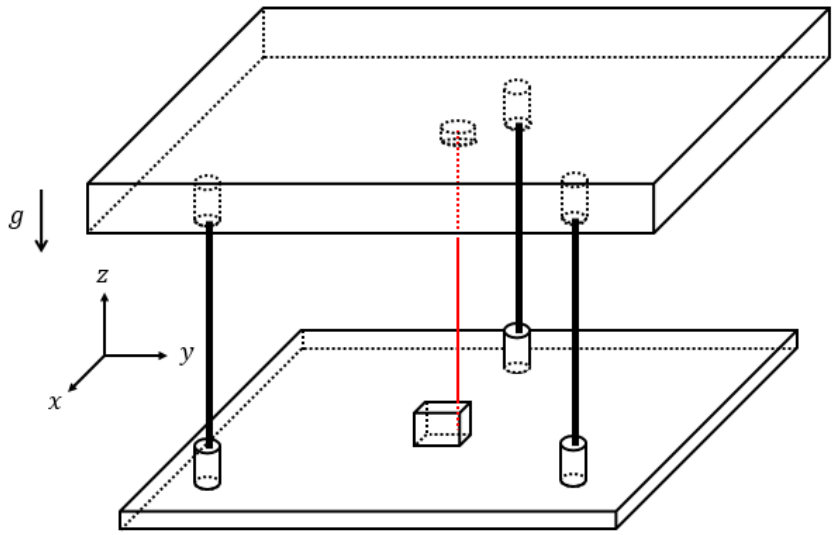

Figure 2.1. The schematic structure of the horizontal-motion isolator with elastic uniform beams. There are 3 elastic beams and there is a wire in the center whose tension can be adjusted.

On the other hand, the horizontal-motion isolator shown in Figure 2.2 has the same number of elastic beams with thin-walled cylinders as their middle sections. Similar to the first case, the wire in the center is used to adjust the tension.

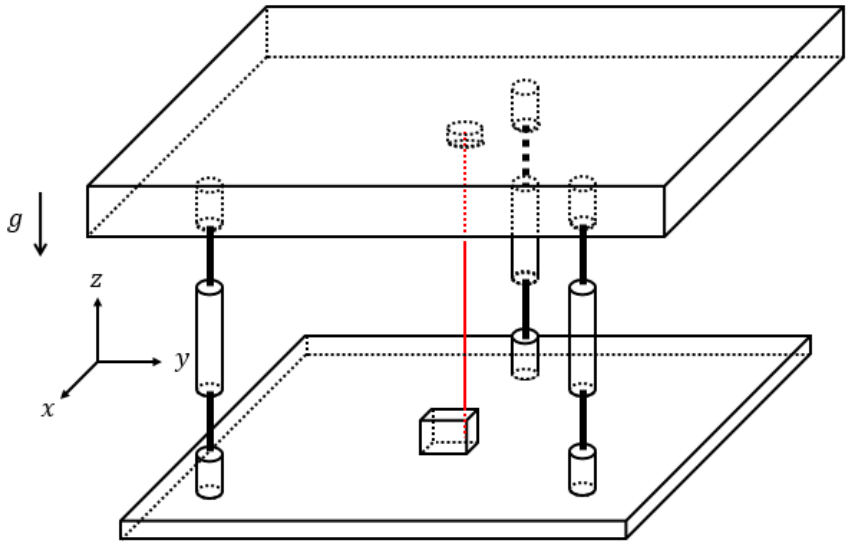

Figure 2.2. The schematic structure of the horizontal-motion isolator with elastic stepped beams. There are 3 elastic stepped beams and there is a wire in the center whose tension can be adjusted.

2.1. Analytical Models

Before the systems shown in Figure 2.1 and Figure 2.2 are analyzed separately in Section 2.1.1 and Section 2.1.2, respectively, it may be fruitful to provide a general technical explanation about them. In both systems, the top platforms can move parallel to ground because their elastic beams are oriented along gravity and connected to the base platform from their lower ends and to the top platform from their upper ends. The translational (k_x, k_y) and torsional (k_{zz}) stiffness of these systems can be adjusted depending on the axial compressive loads applied to the beams. The magnitude of the axial compressive loads results from the top platform weight, the payload weight and the tension force exerted by the

wire in the center. When the wire that is connected to the top platform is tensioned from its lower end, the tension force can be used to adjust the magnitude of the axial compressive loads on the beams. Since the wire is in the center, the tension force applied from a single point on the top platform can create equal axial compressive loads on all the beams. When the payload mass supported by the isolators decreases, the horizontal stiffness of the system increases, and it can be adjusted to quasi-zero values by increasing the tension force in the wire. Therefore, the natural frequencies ω_x, ω_y and ω_{zz} can be kept at very low values even if the payload mass changes.

When the wire tension surpasses the total critical buckling load of the three elastic beams, the beams display negative restoring force. On the other hand, the central wire under tension displays positive restoring force. Moreover, when the top platform deforms horizontally, both the central wire and the elastic beams deform. If the wire is longer than the elastic beams, its deformation angle will be smaller, which results in a smaller positive horizontal restoring force. Consequently, if the tension wire is longer than the beams, it is required to apply less tension force to adjust the horizontal stiffness. In this way, the axial stress magnitudes in the beams and wire can be kept much lower than the yield strengths of these elements. If the tension mechanism is mounted on the upper surface of the base platform as shown in Figure 2.1 and Figure 2.2, the wire can be passed into a groove in the center of the top platform to ensure that its upper end is tied at a point higher than the beams. Alternatively, the tension mechanism can be placed on the lower surface of the base platform, and the wire can be extended through a groove in the platform center. In this way, it is also ensured that the wire is longer than the beams.

When the elastic beams have a circular cross-section, they have the same flexural rigidities in both translational directions ($EI_x = EI_y$) so that they have the same stiffness ($k_x = k_y$) and natural frequencies ($\omega_x = \omega_y$) in these directions. As a result, their translational stiffness and natural frequencies can be denoted as k_{xy} and ω_{xy}, respectively. When these systems support the maximum payload weights at which they lose their elastic stability, the systems have translational quasi-zero-stiffness ($k_{xy} = \omega_{xy} = 0$), and positive

torsional stiffness ($k_{zz} > 0$ and $\omega_{zz} > 0$). Therefore, a tension force is not applied in this situation. However, when the smaller payload mass is supported, it is necessary to apply a tension force in order to reduce k_{xy} and k_{zz} and consequently ω_{xy} and ω_{zz} to very low values.

2.1.1. Horizontal-Motion Isolator with Elastic Uniform Beams

Figure 2.3 and Figure 2.4 show the buckling of the system under two different conditions. In the first condition, the system undergoes lateral buckling; the top platform translates in a random direction in the horizontal xy-plane because the beams are laterally deflected. The critical value of the tension force for this buckling mode is defined as the lateral critical buckling tension force ($T_{cr,xy}$).

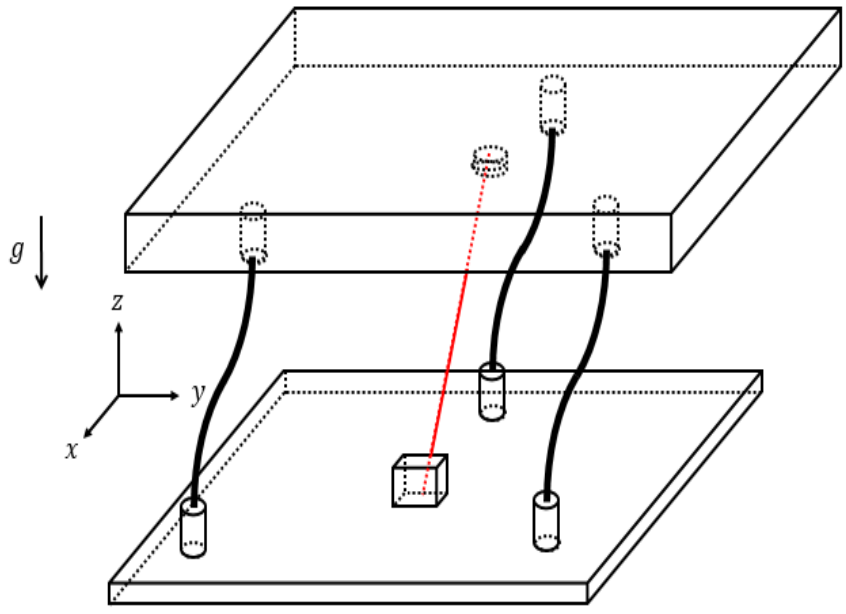

Figure 2.3. Lateral buckling of the system under the action of $T_{cr,xy}$.

In the second condition, the system undergoes torsional buckling; the top platform rotates about its central axis parallel to the vertical z-axis because the beams are laterally and angularly deflected in a simultaneous way. The critical value of the tension force for this mode is defined as the torsional critical buckling tension force ($T_{cr,zz}$).

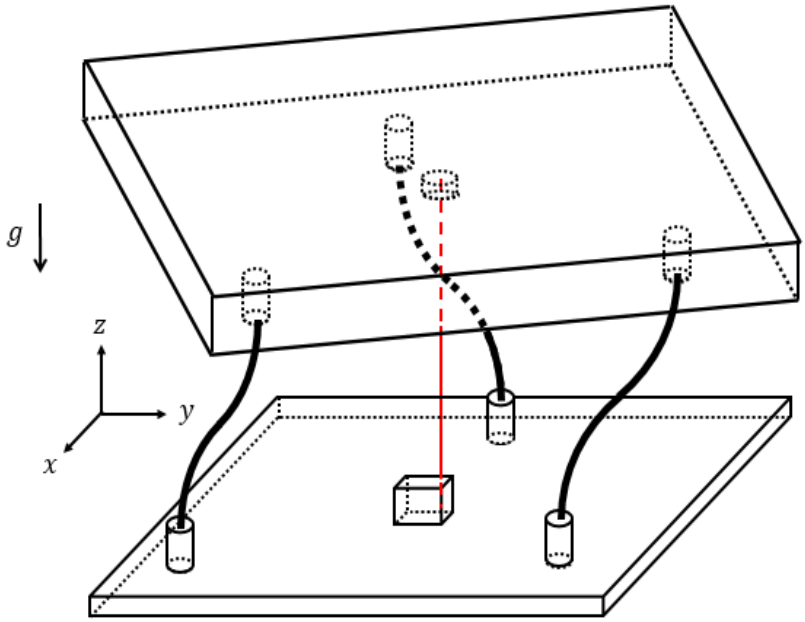

Figure 2.4. Torsional buckling of the system under the action of $T_{cr,zz}$.

If $T_{cr,xy} < T_{cr,zz}$, the system buckles as in the first case and has translational quasi-zero-stiffness ($k_{xy} = 0$). If the opposite occurs, the system buckles as in the second case and has torsional quasi-zero-stiffness ($k_{zz} = 0$). Apart from these two buckling modes shown in Figures 2.3-2.4, Figure 2.5 shows the third buckling mode of the system at which the top platform remains stationary because the beams are deflected laterally as if they have clamped-clamped boundary conditions. The critical value of the tension force for this buckling mode is significantly higher than $T_{cr,xy}$ and $T_{cr,zz}$ and is defined as the upper critical buckling tension force (T_u). Although it is shown that the system undergoes lateral or torsional buckling in any case, it is important to calculate T_u because it can be used to determine the isolation bandwidth of the system.

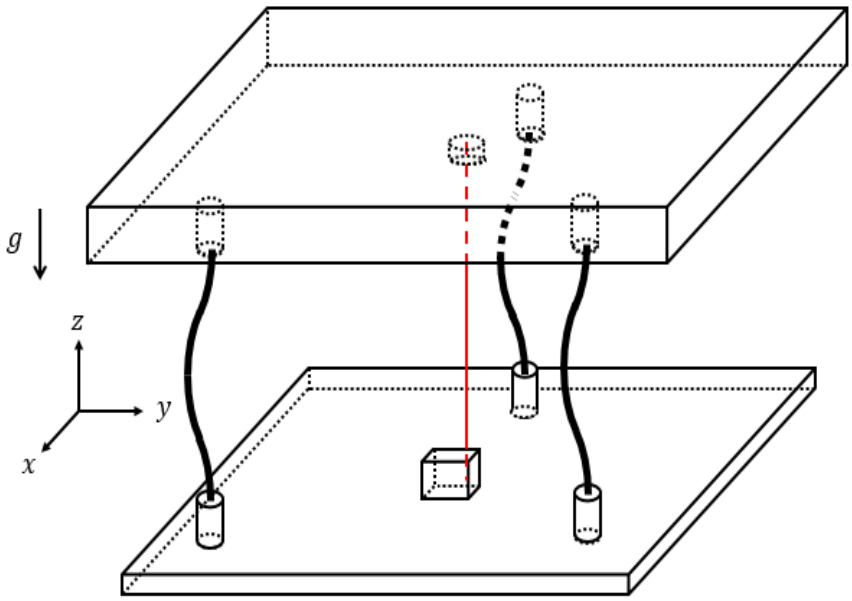

Figure 2.5. Buckling of the system under the action of T_u which is significantly higher than $T_{cr,xy}$ and $T_{cr,zz}$.

The vibrational modes of the system can be also represented by the buckling modes of it shown in Figures 2.3-2.5. While the system is excited by translational ground vibrations at frequencies around the translational natural frequency ω_{xy}, its vibrational mode shape can be characterized as seen in Figure 2.3. Similarly, while it is excited by torsional ground vibrations at frequencies around the torsional natural frequency ω_{zz}, its vibrational mode shape can be characterized as seen in Figure 2.4. Finally, when it is excited by translational or torsional ground vibrations at frequencies around the upper natural frequency ω_u, its vibrational mode shape can be characterized as seen in Figure 2.5.

The natural frequencies of the system (ω_{xy}, ω_{zz} and ω_u) under a given payload and wire tension force can be determined in a similar way of finding the bending natural frequencies of an elastic beam under axial compressive loads by using the energy method [54]. When the lateral vibration mode of the system in Figure 2.3 is examined, the general expression for the lateral deflections of the beams can be written as

$$y = q\left(1 - \cos\frac{\pi x}{l}\right)/2 \tag{2.1}$$

where q is the lateral displacement of the top end of the beams while the bottom ends are fixed and *l* is the length of the beams. For small vibrations, the total axial compressive force on the beams results from the top platform weight ($P_0 = m_0 g$), the payload weight ($P = m_p g$) and the tension force T. Hence, the potential energy of the isolator can be written as

$$E_p = \frac{3EI}{2}\int_0^l \left(\frac{\partial^2 y}{\partial x^2}\right)^2 dx - \left(\frac{P_0+P+T}{2}\right)\int_0^l \left(\frac{\partial y}{\partial x}\right)^2 dx \tag{2.2}$$

The second term in Equation 2.2 represents the diminishing of the energy of compression when the beams expand laterally [54]. Thus, E_p can be found as

$$E_p = \frac{3EI\pi^4}{16l^3}q^2 - \frac{(P_0+P+T)\pi^2}{16l}q^2 \tag{2.3}$$

The kinetic energy of the isolator can be written as

$$E_k = \frac{3\rho A}{2}\int_0^l \left(\frac{\partial y}{\partial t}\right)^2 dx + \left(\frac{m_0+m_p}{2}\right)\dot{q}^2 \tag{2.4}$$

The second term in this equation is the kinetic energy of the top platform and payload. Hence, E_k can be found as

$$E_k = \frac{9\rho Al}{16}\dot{q}^2 + \left(\frac{m_0+m_p}{2}\right)\dot{q}^2 \tag{2.5}$$

Using the Lagrange's equation, the differential equation for the lateral vibrations of the isolator can be written as

$$\frac{d}{dt}\left(\frac{\partial L}{\partial \dot{q}}\right) - \frac{\partial L}{\partial q} = Q \tag{2.6}$$

where $L = E_k - E_p$, and Q is the generalized force (or moment). In this case, Q is the restoring force created by the horizontal component of the tension force T in the wire when the isolator bends. Thus, Q can be taken equal to Tq/l_s where l_s is the length of the wire. As a result, the differential equation for the coordinate q becomes

$$\left(m_0 + m_p + \frac{9\rho A l}{8}\right)\ddot{q} + \left(\frac{3EI\pi^4}{8l^3}\left(1 - \frac{(P_0+P+T)l^2}{3\pi^2 EI}\right) + \frac{T}{l_s}\right)q = 0 \tag{2.7}$$

from which ω_{xy} can be found as

$$\omega_{xy} = \frac{\pi^2}{l^2}\sqrt{\frac{3EI}{9\rho A + 8(m_0+m_p)/l}}\sqrt{1 - \frac{l^2}{3\pi^2 EI}\left(P_0 + P + \left(1 - \frac{8l}{\pi^2 l_s}\right)T\right)} \tag{2.8}$$

In order for ω_{xy} to be zero, the tension force T must be equal to $T_{cr,xy}$ which is found from this equation as

$$T_{cr,xy} = \left(P_{cr,1} - (P_0 + P)\right)\frac{1}{\left(1 - \frac{8l}{\pi^2 l_s}\right)} \tag{2.9}$$

where $P_{cr,1}$ is the first critical buckling force of the isolator when there is no tension force in the wire. Since the isolator has three beams, it can be found from Equation 1.2 that

$P_{cr,1} = 3\pi^2 EI/l^2$. In this equation, if gravity is neglected ($P_0 = P = 0$), $T_{cr,xy}$ becomes greater than $P_{cr,1}$ by the ratio $1/(1 - 8l/\pi^2 l_s)$. In this case, Figure 2.6 shows the change in the ratio $T_{cr,xy}/P_{cr,1}$ with respect to the ratio l_s/l.

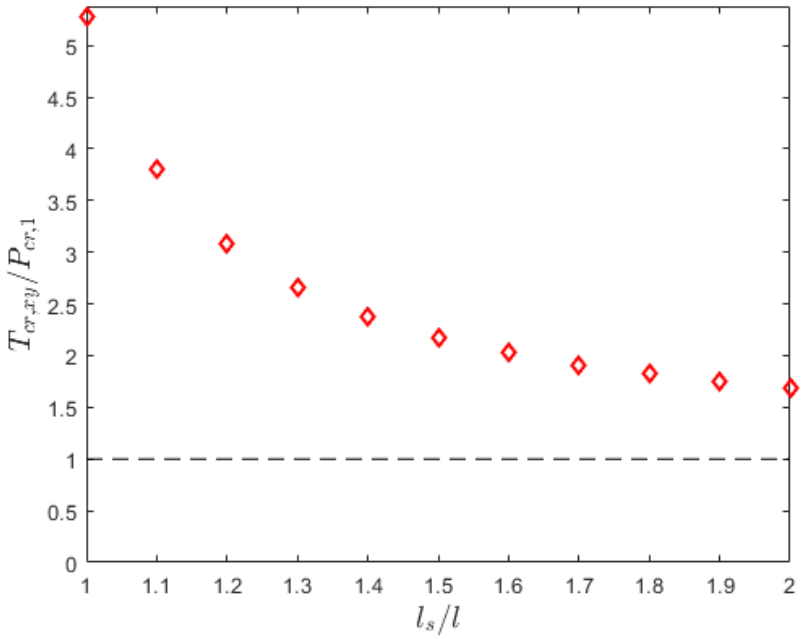

Figure 2.6. The change in the ratio $T_{cr,xy}/P_{cr,1}$ with respect to the ratio l_s/l.

Figure 2.6 shows that if the wire length l_s is much longer than l, this ratio converges to the unity. If analytical methods are used, $T_{cr,xy}$ can be found implicitly [55]. If the ratio of the numerical to analytical $T_{cr,xy}$ values is denoted as $\bar{T}_{cr,xy}$, Figure 2.7 shows the change in the ratio $\bar{T}_{cr,xy}$ with respect to l_s/l.

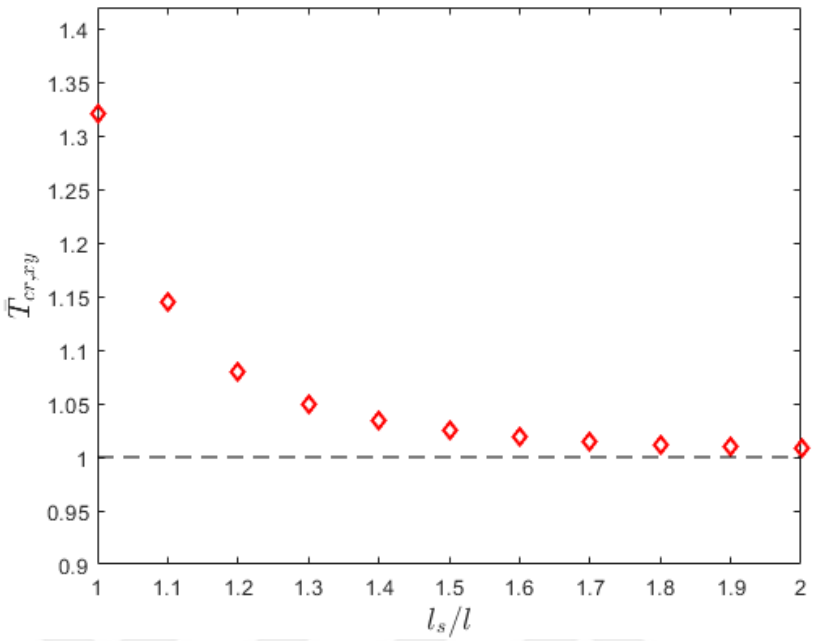

Figure 2.7. The change in ratio $\bar{T}_{cr,xy}$ with respect to l_s/l.

Figure 2.7 shows that the simple analytical formula for $T_{cr,xy}$ in Equation 2.9 can provide results within 2.47 % accuracy for $l_s \geq 1.5l$. However, if the ratio l_s/l becomes smaller, the accuracy of the formula decreases. For instance, if $l_s/l = 1$, then the results may be within 30-35 % accuracy. For this reason, if Equation 2.9 is used to obtain numerical results for $T_{cr,xy}$ within 5 % accuracy, the ratio l_s/l should be in the range $1.3 \leq l_s/l \leq 2$.

When the torsional vibration mode in Figure 2.4 is examined, the lateral-angular deflections of the beams can be decoupled into lateral and angular deflections for small vibrations. The general expression for the lateral deflections can be approximated as the same in Equation 2.1. On the other hand, the general expression for the angular deflections can be approximated as

$$\phi = \frac{q}{l\bar{r}}x \tag{2.10}$$

where $\bar{r}$ is the distance between beam attachment points and the center. Thus, the potential energy of the platform becomes

$$E_p = \frac{3EI}{2}\int_0^l \left(\frac{\partial^2 y}{\partial x^2}\right)^2 dx + \frac{3GI_p}{2}\int_0^l \left(\frac{\partial \phi}{\partial x}\right)^2 dx - \left(\frac{P_0+P+T}{2}\right)\int_0^L \left(\frac{\partial y}{\partial x}\right)^2 dx \qquad (2.11)$$

Therefore, E_p can be obtained as

$$E_p = \frac{3EI\pi^4}{16l^3}q^2 + \frac{3GI_p}{2l\bar{r}^2}q^2 - \frac{(P_0+P+T)\pi^2}{16l}q^2 \qquad (2.12)$$

The kinetic energy of the platform can be written as

$$E_k = \frac{3\rho A}{2}\int_0^l \left(\frac{\partial y}{\partial t}\right)^2 dx + \frac{3\rho I_p}{2}\int_0^l \left(\frac{\partial \phi}{\partial t}\right)^2 dx + \left(\frac{J_0+J_p}{2}\right)\dot{\phi}(l)^2 \qquad (2.13)$$

Therefore, E_k becomes

$$E_k = \frac{9\rho Al}{16}\dot{q}^2 + \frac{\rho I_p l}{2\bar{r}^2}\dot{q}^2 + \left(\frac{J_0+J_p}{2\bar{r}^2}\right)\dot{q}^2 \qquad (2.14)$$

If the Lagrange's method is applied similarly as in Equation 2.6, $Q = 0$, and ω_{zz} can be found as

$$\omega_{zz} = \frac{\pi^2}{l^2}\sqrt{\frac{3EI}{9\rho A + \frac{8\rho I_p}{\bar{r}^2} + \frac{8(J_0+Jp)}{\bar{r}^2 l}}}\sqrt{1 + \frac{8GI_p}{\pi^4 EI}\left(\frac{l}{\bar{r}}\right)^2 - \frac{(P_0+P+T)l^2}{3\pi^2 EI}} \qquad (2.15)$$

In order for ω_{zz} to be zero, the tension force T must be equal to $T_{cr,zz}$ which is found from this equation as

$$T_{cr,zz} = P_{cr,1}\left(1 + \frac{8GI_p}{\pi^4 EI}\left(\frac{l}{\bar{r}}\right)^2\right) - (P_0 + P) \tag{2.16}$$

In this equation, if gravity is neglected ($P_0 = P = 0$), $T_{cr,zz}$ becomes approximately greater than $P_{cr,1}$ by the ratio $\left(1 + \frac{8GI_p}{\pi^4 EI}\left(\frac{l}{\bar{r}}\right)^2\right)$. In this case, Figure 2.8 shows the change in the ratio $T_{cr,zz}/P_{cr,1}$ with respect to the ratio $\bar{r}/l$.

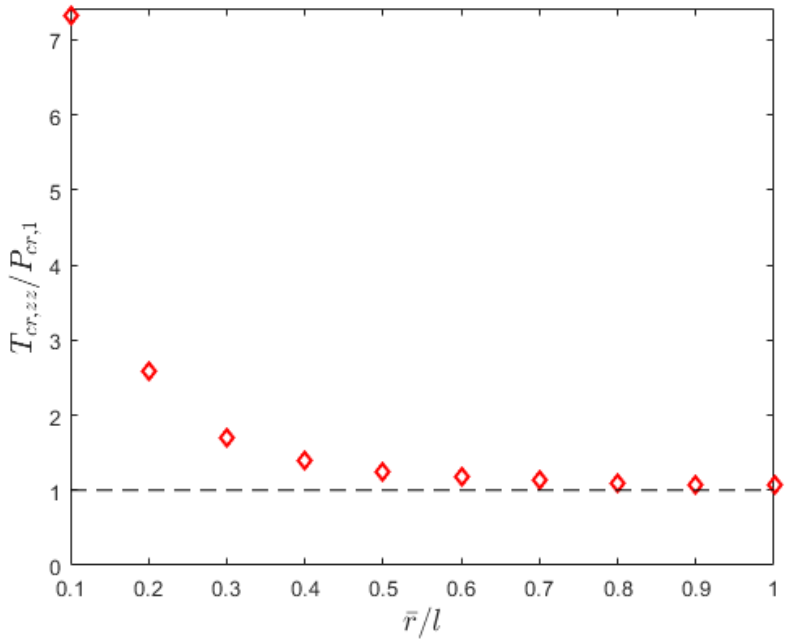

Figure 2.8. The change in the ratio $T_{cr,zz}/P_{cr,1}$ with respect to the ratio $\bar{r}/l$.

Figure 2.8 shows that if the beam distance to the central axis $\bar{r}$ is increased to l, this ratio converges to the unity. If analytical methods are used, $T_{cr,zz}$ can be found implicitly [55]. If

the ratio of the numerical to analytical $T_{cr,zz}$ values is denoted as $\bar{T}_{cr,zz}$, Figure 2.9 shows the change in the ratio $\bar{T}_{cr,zz}$ with respect to $\bar{r}/l$.

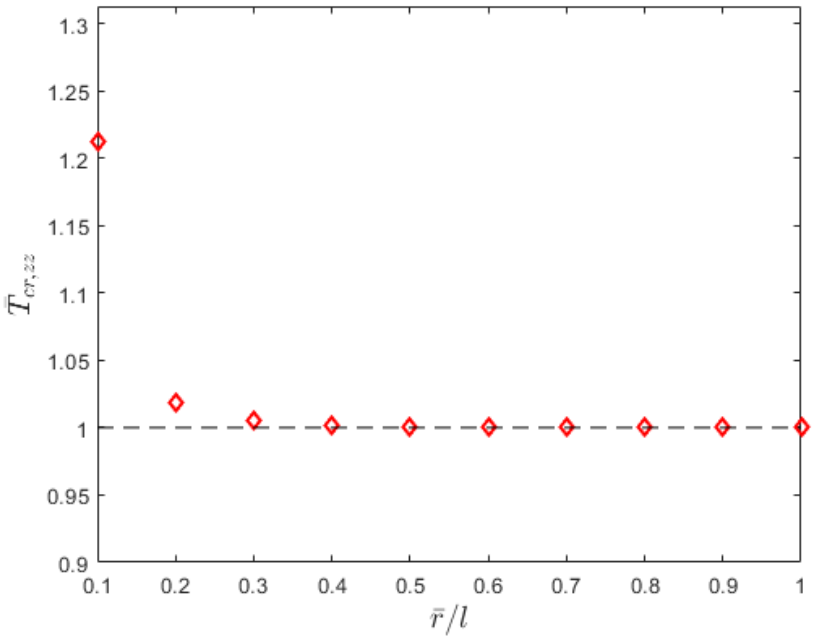

Figure 2.9. The change in ratio $\bar{T}_{cr,zz}$ with respect to $\bar{r}/l$.

Figure 2.9 shows that the numerical formula for $T_{cr,zz}$ in Equation 2.16 can provide results within 0.51 % accuracy for $\bar{r} \geq 0.3l$. However, if the ratio $\bar{r}/l$ becomes smaller, the accuracy of the formula decreases. For instance, if $\bar{r}/l = 0.1$, then the results may be within 20-25 % accuracy. For this reason, if Equation 2.16 is used to obtain numerical results for $T_{cr,zz}$ within 5 % accuracy, the ratio $\bar{r}/l$ should be in the range $0.2 \leq \bar{r}/l \leq 1$.

When the vibrational mode of the system in Figure 2.5 is examined, the general expression for the lateral deflections of the beams can be approximated as

$$y = q\left(1 - \cos\frac{2\pi x}{l}\right)/2 \tag{2.17}$$

If the Lagrange's equations are written similarly for this case, then ω_u can be found as

$$\omega_u = \frac{4\pi^2}{l^2}\sqrt{\frac{3EI}{9\rho A}}\sqrt{1-\frac{(P_0+P+T)l^2}{12\pi^2 EI}} \tag{2.18}$$

In order for ω_u to be zero, the tension force T must be equal to $T_{cr,u}$ which is found from this equation as

$$T_{cr,u} = 4P_{cr,1} - (P_0 + P) \tag{2.19}$$

In this equation, when gravity is neglected, P_0 and P would become zero, and $T_{cr,u}$ becomes greater than $P_{cr,1}$ by exactly four times. This value is also equal to the second critical buckling force of the system ($P_{cr,2} = 4P_{cr,1}$). Hence, Equation 2.19 gives the exact value of $T_{cr,u}$.

With the formulas for the natural frequencies given in Equations 2.8, 2.15 and 2.18, ω_{xy}, ω_{zz} and ω_u can be determined as a function of the tension force T when the system supports a payload with the mass m_p and mass polar moment of inertia J_p. To obtain numerical solutions for ω_{xy}, ω_{zz} and ω_u, it is necessary to design the top platform and the beams by selecting their material and dimensional properties. The payload properties must be also determined. For instance, the top platform can be assumed to be a square plate with the density ρ_0, side length a and height h. Thus, its mass m_0, mass polar moment of inertia J_0, radius of gyration κ_0 and weight P_0 can be found from the equations $m_0 = \rho_0 a^2 h$, $J_0 = m_0 a^2/6$, $\kappa_0 = \sqrt{J_0/m_0}$ and $P_0 = m_0 g$. If $\rho_0 = 7800\,\text{kg/m}^3$, $a = 400$ mm and $h = 10$ mm, it is obtained that $m_0 = 12.48$ kg, $J_0 = 0.3328$ kg.m^2, $\kappa_0 = 163.3$ mm and $P_0 = 122.4$ N. In addition to this, the beams can be assumed to have a circular solid cross-section with the density $\rho = 7800\,\text{kg/m}^3$, Young's modulus $E = 180$ GPa, length $l = 200$ mm and radius $r = 1.50$ mm. When the beams are designed with these properties,

from $P_{cr,1} = 3\pi^2 EI/l^2$, it is obtained that $P_{cr,1} = 529.8$ N. Thus, the maximum payload mass (m_{max}) that the system can support can be found as

$$m_{max} = \left(P_{cr,1} - P_0\right)/g \tag{2.20}$$

from which it is obtained that $m_{max} = (529.8 - 122.4)/9.810 = 41.52$ kg. Moreover, the wire can be assumed to have the length $l_s = 300$ mm. In order to set ω_{xy} and ω_{zz} close to each other when there is no tension force in the wire, the beams can be placed at a distance equal to the radius of gyration of the top platform, dividing the 360 degrees evenly ($\bar{r} = \kappa_0$). Table 2.1 shows the analytical and numerical values of $T_{cr,xy}$, $T_{cr,zz}$ and $T_{cr,u}$for different m_p/m_{max} ratios.

Table 2.1. The analytical (Analyt.) and numerical (Num.) values of $T_{cr,xy}$, $T_{cr,zz}$ and $T_{cr,u}$ for different m_p/m_{max} ratios.

	$\boldsymbol{m_p/m_{max} = 0.10}$		$\boldsymbol{m_p/m_{max} = 0.50}$		$\boldsymbol{m_p/m_{max} = 0.90}$	
	Analyt.	**Num.**	**Analyt.**	**Num.**	**Analyt.**	**Num.**
$\boldsymbol{T_{cr,xy}}$ **(N)**	784.6	797.6	439.2	443.1	88.47	88.62
$\boldsymbol{T_{cr,zz}}$ **(N)**	416.7	416.8	253.8	253.9	90.86	90.94
$\boldsymbol{T_{cr,u}}$ **(N)**	1956	1956	1793	1793	1630	1630

Table 2.1 shows that the numerical values of $T_{cr,xy}$ and $T_{cr,zz}$ obtained from Equation 2.9 and Equation 2.16 are at most 1.66 % and 0.0861 % higher than the analytical results, respectively. If $m_p/m_{max} = 0.10$ and $m_p/m_{max} = 0.50$, the platform buckles in coupled

bending-torsional mode whereas it buckles in lateral bending mode if $m_p/m_{max} = 0.90$. Since $T_{cr,xy}$ and $T_{cr,zz}$ are closest to each other and the overall inertia of the system is maximum when $m_p/m_{max} = 0.90$, the isolator has the best isolation performance among the three cases. At all m_p values, $T_{cr,u}$ is considerably higher than $T_{cr,xy}$ and $T_{cr,zz}$. This is a desired condition because the isolation bandwidth can be maximized if $T_{cr,u} \gg T_{cr,xy}$ and $T_{cr,u} \gg T_{cr,zz}$.

The natural frequencies ω_{xy}, ω_{zz} and ω_u can be determined as a function of the tension force T under a certain loading condition. If the average mass of a vibration-sensitive device is assumed to be around 20 kg, then the case where $m_p/m_{max} = 0.50$ can be examined. If the mass polar moment of inertia of the payload J is assumed to be $J_p = m_p{\kappa_0}^2$, Figure 2.10 shows the changes in ω_{xy} and ω_{zz} with respect to T.

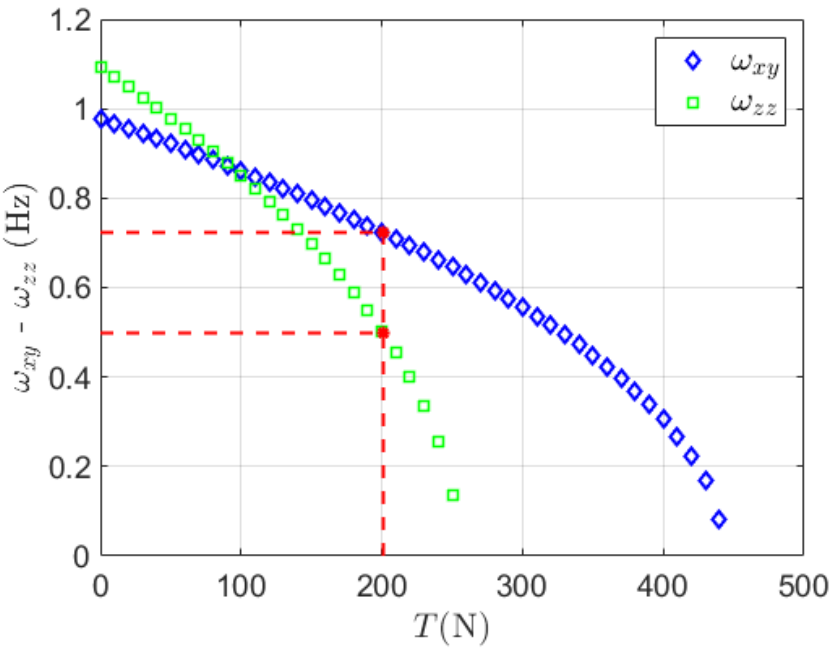

Figure 2.10. When $m_p/m_{max} = 0.50$, the changes in ω_{xy} and ω_{zz} with respect to T. At the intersection of the horizontal and vertical red dashed curves, $T_o = 201$ N, $\omega_{xy} = 0.723$ Hz and $\omega_{zz} = 0.498$ Hz.

Figure 2.10 shows that when T approaches $T_{cr,xy}$ and $T_{cr,zz}$, the horizontal natural frequencies ω_{xy} and ω_{zz} converge to zero, respectively. Since ω_{zz} decreases to zero at a faster rate than ω_{xy}, the system achieves a quasi-zero-stiffness condition along the torsional axis. The intersection points of the horizontal and vertical red-dashed curves correspond to the values of ω_{xy} and ω_{zz} when the lowest natural frequency of the system (ω_{zz}) is equal to 0.5 Hz. To keep the system stable, the lowest natural frequency is not decreased below 0.5 Hz. The tension force satisfying this condition can be defined as the optimum tension force and can be represented as T_o. Under this condition, it is obtained that, $T_o = 201$ N, $\omega_{xy} = 0.723$ Hz and $\omega_{zz} = 0.498$ Hz. Similarly, Figure 2.11 shows the change in ω_u with respect to T. At the intersection of the horizontal and vertical red dashed curves, $T_o = 201$ N and $\omega_u = 283$ Hz.

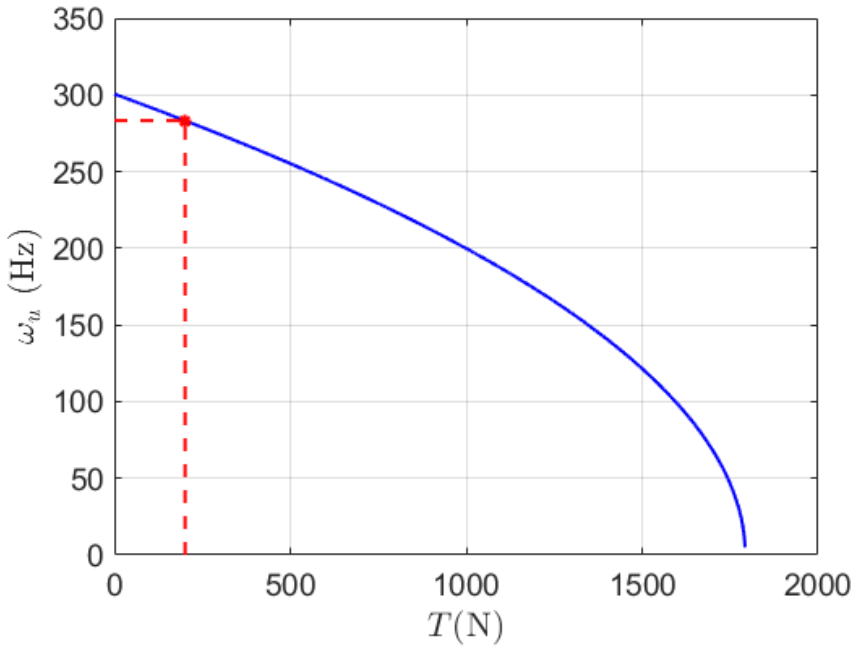

Figure 2.11. When $m_p/m_{max} = 0.50$, the change in ω_u with respect to T. At the intersection of the horizontal and vertical red dashed curves, $T_o = 201$ N and $\omega_u = 283$ Hz.

Figure 2.10 and Figure 2.11 show that when $T_o = 201$ N, $\omega_{xy}/\omega_u = 0.0026$ for translational vibrations and $\omega_{zz}/\omega_u = 0.0018$ for torsional vibrations. The isolation bandwidth starts at $\sqrt{2}\omega_{zz} = 0.71$ Hz and extends up to $\omega_u = 283$ Hz for torsional vibrations while the isolation bandwidth starts at $\sqrt{2}\omega_{xy} = 1.02$ Hz and extends up to $\omega_u = 283$ Hz for translational vibrations. Since $\omega_{zz}/\omega_u < \omega_{xy}/\omega_u$, the system has a better isolation performance for torsional vibrations.

For $m_p/m_{max} > 0.50$, isolation at low frequencies becomes better because the overall inertia of the isolator increases. For instance, when $m_p/m_{max} = 0.90$, ω_{xy} and ω_{zz} are less than 0.5 Hz at all values of T. For this reason, it is more important to determine the isolation performance when $m_p/m_{max} \leq 0.50$. Table 2.2 shows the values of ω_{xy}, ω_{zz} and ω_u at $T = T_o$ when the ratio m_p/m_{max} is at different values.

Table 2.2. The values of ω_{xy}, ω_{zz} and ω_u at $T = T_o$ for various m_p/m_{max} values.

	$\boldsymbol{m_p/m_{max} = 0.10}$	$\boldsymbol{m_p/m_{max} = 0.20}$	$\boldsymbol{m_p/m_{max} = 0.30}$	$\boldsymbol{m_p/m_{max} = 0.40}$	$\boldsymbol{m_p/m_{max} = 0.50}$
$\boldsymbol{T_o}$ **(N)**	390	343	296	248	200
$\boldsymbol{\omega_{xy}}$ **(Hz)**	1.32	1.12	0.967	0.836	0.723
$\boldsymbol{\omega_{zz}}$ **(Hz)**	0.497	0.498	0.500	0.498	0.498
$\boldsymbol{\omega_u}$ **(Hz)**	281	281	282	283	283

From the above results, it is seen that even if the value of m/m_{max} is changed, ω_{zz} can be adjusted to the order of 0.5 Hz in all cases, showing that the wire tension mechanism can maintain the torsional vibration isolation performance of the system even if the payload mass changes. Although the wire tension mechanism can be used to decrease ω_{xy} and ω_{zz} at the same time, since ω_{zz} decreases at a faster rate than ω_{xy} as T increases, the system usually loses its stability before ω_{xy} is lowered to 0.5 Hz. For heavier payload masses, the difference

between ω_{xy} and ω_{zz} decreases, and the system has a better multi-axis isolation performance.

2.1.2. Horizontal-Motion Isolator with Elastic Stepped Beams

Figure 2.12(a) shows the schematic structure of the elastic stepped beams that are used in the system shown in Figure 2.2. In order to increase the isolation bandwidth of the system, the stepped beams shown in Figure 2.12 are designed by using thin-walled cylinders with a larger outer radius in their middle sections. The thin beams as the lower and upper parts of the stepped beams are connected to the thin-walled cylinders with the fasteners. While the thin beams can be firmly inserted into the fasteners with a press or similar equipment, the fasteners can also be inserted into the thin-walled cylinders in the same way. Alternatively, these parts can be combined by heat treatment. Moreover, these parts (thin beam, fasteners and thin-walled cylinder) can also be joined by methods such as bonding, soldering, brazing or welding.

To simplify the analytical models in this section, the stepped beams can be modelled as if they are formed from five different beam parts as shown in Figure 2.12(b). The parts of the thin beams inside the fasteners and the parts of the thin-walled cylinders surrounding the fasteners can be assumed to be the parts of the fasteners. Hence, the fasteners can be modelled as the red parts with a solid circular cross-section with the flexural rigidity $E_2 I_2$. Besides, the stepped beams are symmetric; the thin beams have the same design parameters. Similarly, the fasteners are identical to each other.

Since the cross-section of the stepped beams changes abruptly, the approximation of beam deflections by trigonometric functions as in Section 2.1.1 may not provide satisfactory results for the determination of the critical buckling tensions and horizontal natural frequencies. In the following two sections, the buckling and vibration analyses of the system are performed.

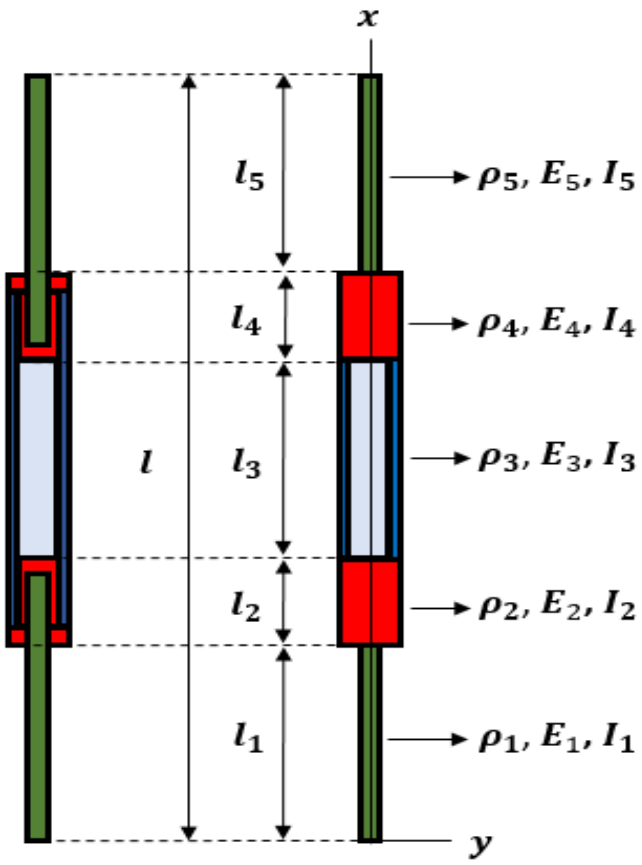

Figure 2.12. (a) The schematic structure of the elastic stepped beam. The green parts are the thin beams, the red parts are the fasteners, and the blue parts are the thin-walled cylinders, (b) The modelling of the elastic stepped beam with 5 parts.

2.1.2.1. Buckling of the Isolator. As in Section 2.1.1, the maximum payload mass (m_{max}) that the isolator shown in Figure 2.2 can support can be found from Equation 2.20. Since the stepped beams are used, the first critical buckling force $P_{cr,1}$ can be found by writing separately the differential equations for lateral deflections of the beam parts as shown in Figure 2.12(b) [54]. The general expression for these differential equations can be written as

$$E_i I_i \frac{d^4 y_i}{dx^4} + \left(\frac{P}{3}\right) \frac{d^2 y_i}{dx^2} = 0 \qquad (2.21)$$

where the subscript i takes the numbers 1, 2, 3, 4 and 5 for the lower thin beam, lower fastener, middle thin-walled cylinder, upper fastener and upper thin beam, respectively. In

this equation, P is a vertical compressive force that is aimed to be found as $P_{cr,1}$. Since it is assumed that the force P compresses each of the three beams equally, it is divided by three in Equation 2.1. In this analysis, the top platform and payload weights ($m_0 g$ and $m_p g$) do not contribute to P because gravity is not taken into account. Since the stepped beams are formed from identical thin beams and fasteners, the expressions $E_1 I_1 = E_5 I_5$ and $E_2 I_2 = E_4 I_4$ can be written. Using the notation ${k_i}^2 = P/3E_i I_i$, the general solution of Equation 2.21 is found as

$$y_i = a_i \sin k_i x + b_i \cos k_i x + c_i x + d_i \tag{2.22}$$

In this equation, since there are five parts of the beam, the total number of the unknown constants a_i, b_i, c_i and d_i are 20, and they can be found from the boundary and continuity conditions of the beams. The boundary conditions at the lower end are

$$y_1 = 0 \tag{2.23}$$

$$\frac{dy_1}{dx} = 0 \tag{2.24}$$

The continuity conditions are defined at points where the cross-section of the beam changes. These points are at the coordinates $x = l_1$, $x = l_1 + l_2$, $x = l_1 + l_2 + l_3$ and $x = l_1 + 2l_2 + l_3$ as shown in Figure 2.12(b). The general expressions of the continuity conditions at these four points are

$$y_i - y_{i+1} = 0 \tag{2.25}$$

$$\frac{dy_i}{dx} - \frac{dy_{i+1}}{dx} = 0 \tag{2.26}$$

$$E_i I_i \frac{d^2 y_i}{dx^2} - E_{i+1} I_{i+1} \frac{d^2 y_{i+1}}{dx^2} = 0 \tag{2.27}$$

$$E_i I_i \frac{d^3 y_i}{dx^3} - E_{i+1} I_{i+1} \frac{d^3 y_{i+1}}{dx^3} = 0 \tag{2.28}$$

where $i = 1, 2, 3, 4$. Finally, the boundary conditions at the upper end are

$$\frac{dy_5}{dx} = 0 \tag{2.29}$$

$$\frac{d^3 y_5}{dx^3} + k_1 \frac{dy_5}{dx_3} = 0 \tag{2.30}$$

When the general solutions in Equation 2.22 are substituted into Equation 2.23-2.30, the determinant of 20 linear homogeneous equations obtained from the boundary and continuity conditions becomes zero. Hence, the characteristic equation of this determinant gives the critical value of P. Using the numerical solution techniques, this critical value can be found as $P_{cr,1}$.

It has been explained in Section 2.1.1 that when the system carries a payload mass less than m_{max}, it is necessary to apply a certain tension force T to buckle the system. Thus, as explained previously, the system may buckle in two different modes (see Figure 2.13 and Figure 2.14). These buckling modes are defined as lateral and torsional buckling of the system, and the critical tension forces for these conditions are $T_{cr,xy}$ and $T_{cr,zz}$.

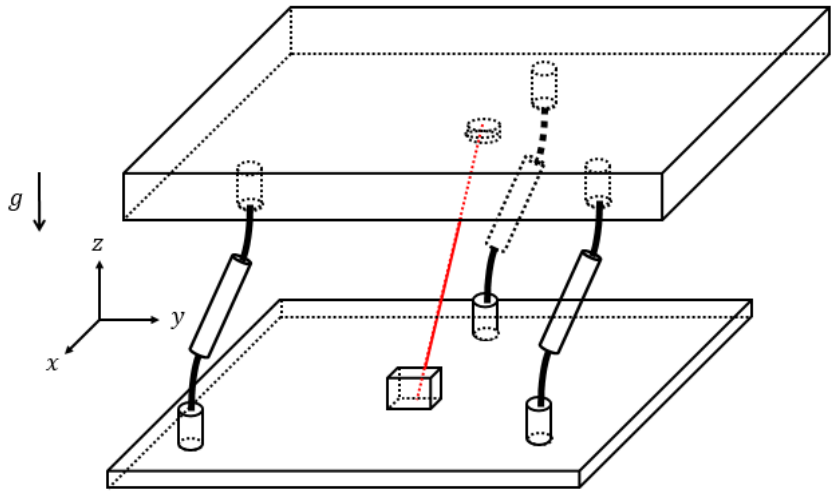

Figure 2.13. Lateral buckling of the system under the action of $T_{cr,xy}$.

When the system buckles as shown in Figure 2.13 ($T_{cr,xy} < T_{cr,zz}$), the stepped beams are only deflected laterally, and the tension wire creates a restoring force in the horizontal plane. On the other hand, when $T_{cr,zz} < T_{cr,xy}$, Figure 2.14 shows that the beams are laterally and angularly deflected, and the tension wire remains vertical.

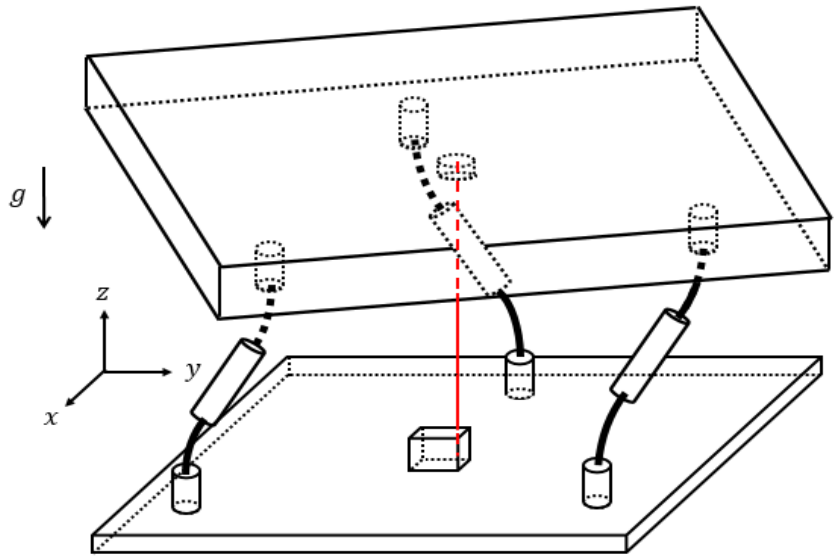

Figure 2.14. Lateral buckling of the system under the action of $T_{cr,zz}$.

Similarly, Figure 2.15 shows the buckling mode of the system that corresponds to a higher critical value of the tension force which is known as $T_{cr,u}$. Almost in all cases, it is obtained that $T_{cr,u} \gg T_{cr,xy}$ and $T_{cr,u} \gg T_{cr,zz}$.

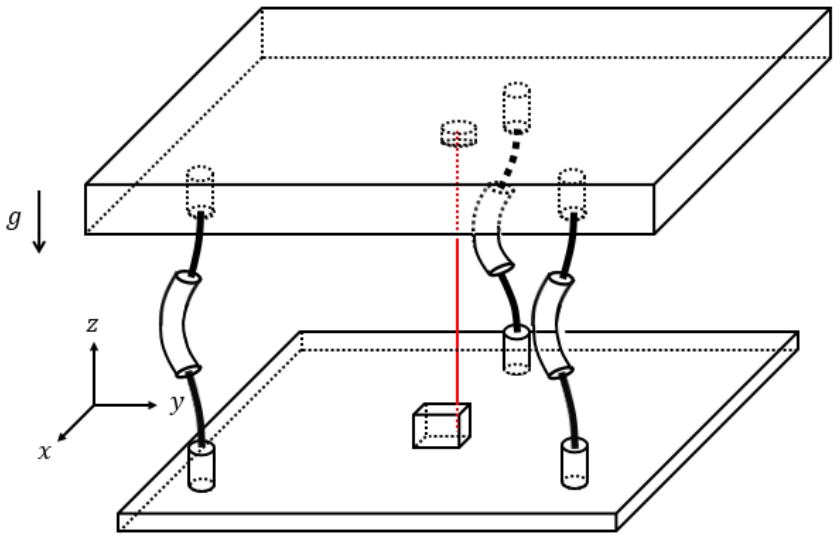

Figure 2.15. Buckling of the system under the action of T_u which is significantly higher than $T_{cr,xy}$ and $T_{cr,zz}$.

When the first buckling condition (see Figure 2.13) is considered, $T_{cr,xy}$ can be found by analyzing the case of the buckling of a column with load through a fixed point [55]. The general expression for the differential equations of lateral deflections of the beam parts can be written as

$$E_i I_i \frac{d^4 y_i}{dx^4} + \left(\frac{P_0+P+T}{3}\right)\frac{d^2 y_i}{dx^2} = 0 \qquad (2.31)$$

Using the notation $k_i = (P_0 + P + T)/3E_i I_i$, the general form of the solutions of this equation can be written similarly as in Equation 2.22. However, this problem differs from the usual case of Euler Buckling in that the shear forces at the upper ends of the beams are

created by the horizontal component of T. For small lateral deflections, if the upper ends of the beams are deflected by δ, the horizontal component of the tension force T can be taken equal to $T\delta/l_s$. Hence, the boundary condition expressed in Equation 2.30 becomes

$$\frac{d^3y_5}{dx^3} + k_1\frac{dy_5}{dx} - \frac{T\delta}{3E_1I_1l_s} = 0 \tag{2.32}$$

The other boundary and continuity conditions can be expressed from Equation 2.23 to Equation 2.29. The unknown constants a_i, b_i, c_i and d_i of the general solutions can be found in terms of δ. As a final condition, the lateral deflection of the upper ends can be written as

$$y_5 = a_5 \sin k_1 l + b_5 \cos k_1 l + c_5 l + d_5 = \delta \tag{2.33}$$

Consequently, $T_{cr,xy}$ can be found from this nonlinear equation by numerical methods.

When the second buckling condition (see Figure 2.14) is investigated, lateral-angular deflections of the beams can be decoupled into lateral and angular deflections. As in the first buckling case (see Figure 2.13), the differential equations for lateral deflections are the same (see Equation 2.31). In addition to this, the boundary and continuity conditions can be written as in Equations 2.23-2.29. The general expression for the differential equations of angular deflections can be written as

$$G_iI_{pi}\frac{d^2\phi_i}{dx^2} = 0 \tag{2.34}$$

Hence, the general solution of Equation 2.34 becomes

$$\phi_i = e_i x + f_i \tag{2.35}$$

In this equation, the total number of the unknown constants e_i and f_i are 10, and they can be found from the boundary and continuity conditions. The boundary condition at the lower end of the beam is

$$\phi_1 = 0 \tag{2.36}$$

The general expressions for the continuity conditions at the points where the cross-section of the beams changes can be written as

$$\phi_i - \phi_{i+1} = 0 \tag{2.37}$$

$$G_i I_{pi} \frac{d\phi_i}{dx} - G_{i+1} I_{p(i+1)} \frac{d\phi_{i+1}}{dx} = 0 \tag{2.38}$$

Finally, the boundary conditions at the upper end of the beam are

$$y_5 - \bar{r}\phi_5 = 0 \tag{2.39}$$

$$\left(\frac{d^3 y_5}{dx^3} + k_1 \frac{dy_5}{dx}\right)\bar{r} - \frac{G_1 I_{p1}}{E_1 I_1} \frac{d\phi_5}{dx} = 0 \tag{2.40}$$

Thus, the total number of the unknown constants a_i, b_i, c_i, d_i, e_i and f_i in Equation 2.22 and Equation 2.35 are 30, and they can be found in terms of δ if the general solutions

are substituted into the equations for the boundary and continuity conditions. As a final condition, the lateral deflection at the upper end of the beam is

$$y_5 = a_5 \sin k_1 l + b_5 \cos k_1 l + c_5 l + d_5 = \delta \tag{2.41}$$

Consequently, $T_{cr,zz}$ can be found from this nonlinear equation by numerical methods.

When the third buckling condition in Figure 2.15 is investigated, it is seen that the boundary conditions at the lower and upper ends of the beams are $y_1 = 0$ and $\partial y_1/\partial x = 0$ and $y_5 = 0$ and $\partial y_5/\partial x = 0$, respectively. Thus, the beams can be considered to have clamped-clamped boundary conditions, and the continuity conditions are the same as expressed from Equation 2.25 to Equation 2.28. Since the deflected shape of the beams corresponds to their second buckling mode, $T_{cr,u}$ can be found as

$$T_{cr,u} = P_{cr,2} - (P_0 + P) \tag{2.42}$$

In this equation, $P_{cr,2}$ can be found similarly as $P_{cr,1}$.

$T_{cr,xy}$, $T_{cr,zz}$ and $T_{cr,u}$ can be determined if the design parameters and loading conditions of the isolator are given. To compare the isolation bandwidths of the isolators shown in Figure 2.1 and Figure 2.2, the design parameters of the second system can be chosen the same as the first system except that the stepped beams have a thicker middle part (thin-walled cylinder) than the uniform beams. The thin parts of the stepped beams have the same cross-section as the uniform beams ($r = 1.50$ mm), and the thick part have the outer radius $r_{3,o} = 3.00$ mm and wall thickness $t = 0.20$ mm. The lengths l_1, l_2 and l_3 in Figure 2.8(b) can be chosen as $l_1 = 50$ mm, $l_2 = 10$ mm and $l_3 = 80$ mm such that $l = 2l_1 + 2l_2 + l_3 = 200$ mm.

With these values above, it is found that $P_{cr,1} = 617.1$ N. Thus, from Equation 2.20, the maximum payload mass that the isolator can support is found as $m_{max} = 50.42$ kg. Table 2.3 shows the values of $T_{cr,xy}$, $T_{cr,zz}$ and T_u for various values of m_p/m_{max}.

Table 2.3. The values of $T_{cr,xy}$, $T_{cr,zz}$ and $T_{cr,u}$ for various values m_p/m_{max} ratios.

	$\boldsymbol{m_p/m_{max} = 0.10}$	$\boldsymbol{m_p/m_{max} = 0.50}$	$\boldsymbol{m_p/m_{max} = 0.90}$
$\boldsymbol{T_{cr,xy}}$ **(N)**	1020	569.0	114.3
$\boldsymbol{T_{cr,zz}}$ **(N)**	531.6	333.7	135.8
$\boldsymbol{T_{cr,u}}$ **(N)**	4433	4235	4038

Table 2.3 shows that when m_p/m_{max} is 0.10 and 0.50, the platform buckles in coupled bending-torsional mode whereas it buckles in lateral bending mode when $m_p/m_{max} = 0.90$. Hence, for small m_p/m_{max} values, the isolator is more likely to buckle in bending-torsional coupled mode than in lateral bending mode. As the ratio m_p/m_{max} increases, it becomes more probable that the isolator buckles in lateral bending mode. Since $T_{cr,xy}$ and $T_{cr,zz}$ are closest to each other when $m_p/m_{max} = 0.90$, the isolator has the best isolation performance among the three cases. At all m_p/m_{max} values, $T_{cr,u}$ is considerably higher than $T_{cr,xy}$ and $T_{cr,zz}$. This is a desired condition because the isolation bandwidth can be maximized if $T_{cr,u} \gg T_{cr,xy}$ and $T_{cr,u} \gg T_{cr,zz}$.

2.1.2.2. Vibration of the Isolator. The natural frequencies ω_{xy}, ω_{zz} and ω_u can be determined as a function of the tension force T under a given loading condition. To obtain them, it is necessary to write the differential equations for lateral and angular vibrations of the isolator, and their general solutions must be substituted into the boundary and continuity conditions. Finally, ω_{xy}, ω_{zz} and ω_u can be found from the system of linear homogeneous equations by numerical methods. Vibration modes of the isolator can be represented similarly as in Figure 2.13. When the isolator has bending mode as in Figure 2.13, the general expression for the differential equations of lateral vibrations can be written as [55]

$$E_i I_i \frac{\partial^4 y_i}{\partial x^4} + \left(\frac{P_0+P+T}{3}\right)\frac{\partial^2 y_i}{\partial x^2} + \rho_i A_i \frac{\partial^2 y_i}{\partial t^2} = 0 \quad (2.43)$$

where the subscript i takes the numbers 1, 2, 3, 4 and 5 for the lower thin beam, lower fastener, middle thin-walled cylinder, upper fastener and upper thin beam, respectively. Using the notations ${k_i}^2 = \frac{P_0+P+T}{3E_i I_i}$ and $a_i = \frac{\rho_i A_i}{E_i I_i}$, Equation 2.43 can be rearranged as

$$\frac{\partial^4 y_i}{\partial x^4} + {k_i}^2 \frac{\partial^2 y_i}{\partial x^2} + a_i \frac{\partial^2 y_i}{\partial t^2} = 0 \quad (2.44)$$

The solutions of these partial differential equations can be assumed to be in the form

$$y_i = A f_i(x) e^{j\omega t} \quad (2.45)$$

where A is an arbitrary constant and $j = \sqrt{-1}$. If these solutions are plugged into Equation 2.44, the ordinary differential equations for $f_i(x)$ are obtained as

$$\frac{d^4 f_i(x)}{dx^4} + {k_i}^2 \frac{d^2 f_i(x)}{dx^2} - a_i \omega^2 f_i(x) = 0 \quad (2.46)$$

for which the general solutions are

$$f_i(x) = a_i \sinh \lambda_{i1} x + b_i \cosh \lambda_{i1} x + c_i \sin \lambda_{i2} x + d_i \cos \lambda_{i2} x \quad (2.47)$$

where

$$\lambda_{i1} = \left[\sqrt{a_i\omega^2 + \frac{{k_i}^4}{4}} - \frac{{k_i}^2}{2}\right]^{\frac{1}{2}} \tag{2.48}$$

$$\lambda_{i2} = \left[\sqrt{a_i\omega^2 + \frac{{k_i}^4}{4}} + \frac{{k_i}^2}{2}\right]^{\frac{1}{2}} \tag{2.49}$$

The unknown constants a_i, b_i, c_i and d_i in Equation 2.47 can be determined from the equations for the boundary and continuity conditions. Hence, the boundary conditions at the lower end of the beam are

$$y_1 = 0 \tag{2.50}$$

$$\frac{\partial y_1}{\partial x} = 0 \tag{2.51}$$

The general expression for the continuity conditions at the intersection points shown in Figure 2.12(b) can be written as

$$y_i - y_{i+1} = 0 \tag{2.52}$$

$$\frac{\partial y_i}{\partial x} - \frac{\partial y_{i+1}}{\partial x} = 0 \tag{2.53}$$

$$E_i I_i \frac{\partial^2 y_i}{\partial x^2} - E_{i+1} I_{i+1} \frac{\partial^2 y_{i+1}}{\partial x^2} = 0 \tag{2.54}$$

$$E_i I_i \frac{\partial^3 y_i}{\partial x^3} - E_{i+1} I_{i+1} \frac{\partial^3 y_{i+1}}{\partial x^3} = 0 \tag{2.55}$$

for $i = 1,2,3,4$. The boundary conditions at the upper end of the beam are

$$\frac{\partial y_5}{\partial x} = 0 \tag{2.56}$$

$$\left(m_0 + m_p\right) \frac{\partial^2 y_5}{\partial t^2} - 3\left(E_1 I_1 \frac{\partial^3 y_5}{\partial x^3} + \left(\frac{P_0+P+T}{3}\right) \frac{\partial y_5}{\partial x}\right) + \frac{T y_5}{l_s} = 0 \tag{2.57}$$

In this equation, the first term is the inertial force of the top platform and payload. If the general solutions in Equation 2.45 are substituted into the equations from Equation 2.50 to Equation 2.57, the determinant of a system of 20 linear homogeneous equations becomes zero. Thus, using numerical methods, the solution of the characteristic equation of the determinant is found as ω_{xy} for any value of T.

When the isolator has coupled bending-torsional mode as in Figure 2.14, lateral-angular vibrations of the beams can be decoupled into lateral and angular vibrations. As in the first vibration mode (see Figure 2.13), the differential equations for lateral vibrations are the same (see Equations 2.44). In addition to this, the boundary and continuity conditions can be expressed the same as in Equation 2.50- 2.57. The general expression for the differential equations of angular vibrations can be written as

$$\rho_i I_{pi} \frac{\partial^2 \phi_i}{\partial t^2} = \left(G_i I_{pi} - \left(\frac{P_0+P+T}{3A_i}\right) I_{pi}\right) \frac{\partial^2 \phi_i}{\partial x^2} \tag{2.58}$$

The solutions of these partial differential equations can be assumed to be in the form

$$\phi_i = B\theta_i(\mathrm{x})\mathrm{e}^{\mathrm{j}\omega\mathrm{t}} \tag{2.59}$$

where B is an arbitrary constant and $j = \sqrt{-1}$. If Equation 2.59 is plugged into Equation 2.58, the ordinary differential equations for $\theta_i(\mathrm{x})$ becomes

$$(G_i I_{pi} - \left(\frac{P_0+P+T}{3A_i}\right) I_{pi}) \frac{d^2\theta_i(x)}{dx^2} + \rho_i I_{pi}\omega^2\theta_i(x) = 0 \tag{2.60}$$

Thus, the general solutions of this equation can be written as

$$\theta_i(x) = e_i \sin\sigma_i x + f_i \cos\sigma_i x \tag{2.61}$$

where σ_i is a separation constant and is related to the angular frequency ω as $\sigma_i = \omega / \sqrt{\frac{1}{\rho_i}(G_i - \left(\frac{P_0+P+T}{3A_i}\right)}$.

In Equation 2.61, the total number of the unknown constants e_i and f_i are 10, and they can be found from the boundary and continuity conditions. The boundary condition at the lower end of the beam is

$$\phi_1 = 0 \tag{2.62}$$

The general expressions for the continuity conditions at the points where the cross-section of the beams changes can be written as

$$\phi_i - \phi_{i+1} = 0 \tag{2.63}$$

$$G_i I_{pi} \frac{\partial \phi_i}{\partial x} - G_{i+1} I_{p(i+1)} \frac{\partial \phi_{i+1}}{\partial x} = 0 \tag{2.64}$$

for $i = 1,2,3,4$. Finally, the boundary conditions at the upper end of the beam are

$$y_5 - \bar{r}\phi_5 = 0 \tag{2.65}$$

$$\left(J_0 + J_p\right) \frac{\partial^2 \phi_5}{\partial t^2} - 3\left(E_1 I_1 \frac{\partial^3 y_5}{\partial x^3} + \left(\frac{P_0 + P + T}{3A_i}\right) \frac{\partial y_5}{\partial x}\right) \bar{r} + 3G_1 I_{p1} \frac{\partial \phi_5}{\partial x} = 0 \tag{2.66}$$

In this equation, the first term is the inertial moment of the top platform and payload. If the general solutions in Equation 2.45 and Equation 2.59 are substituted into the equations from Equation 2.50 to Equation 2.56 and from Equation 2.62 to Equation 2.66, the determinant of a system of 30 linear homogeneous equations becomes zero. Thus, using numerical methods, the solution of the characteristic equation of the determinant is found as ω_{zz} for any value of T.

When the isolator has bending mode as in Figure 2.15, the general expression for the differential equations of lateral vibrations can be written the same as before. It is seen from this figure that the boundary conditions are $y_1 = 0$ and $\partial y_1/\partial x = 0$ at the lower ends and $y_5 = 0$ and $\partial y_5/\partial x = 0$ at the upper ends. Thus, the beams can be considered to have clamped-clamped boundary conditions. The continuity conditions, on the other hand, can be written the same as in Equation 2.52-2.55. When the general solutions are substituted into these boundary and continuity conditions, the determinant of a system of 20 linear homogeneous equations becomes zero. Thus, using numerical methods, the solution of the characteristic equation of the determinant is found as ω_u for any value of T.

With the same design parameters used in Section 2.1.2.1, the natural frequencies ω_{xy}, ω_{zz} and ω_u can be determined relative to the tension force T under a certain loading

condition. If $m_p/m_{max} = 0.50$ and $J_p = m_p{\kappa_0}^2$, Figure 2.16 shows the changes in ω_{xy} and ω_{zz} with respect to T. As in the case for the isolator with elastic uniform beams, T can be increased to the point at which the lowest natural frequency (ω_{zz}) is decreased to 0.5 Hz in order to keep the isolator in a stable condition.

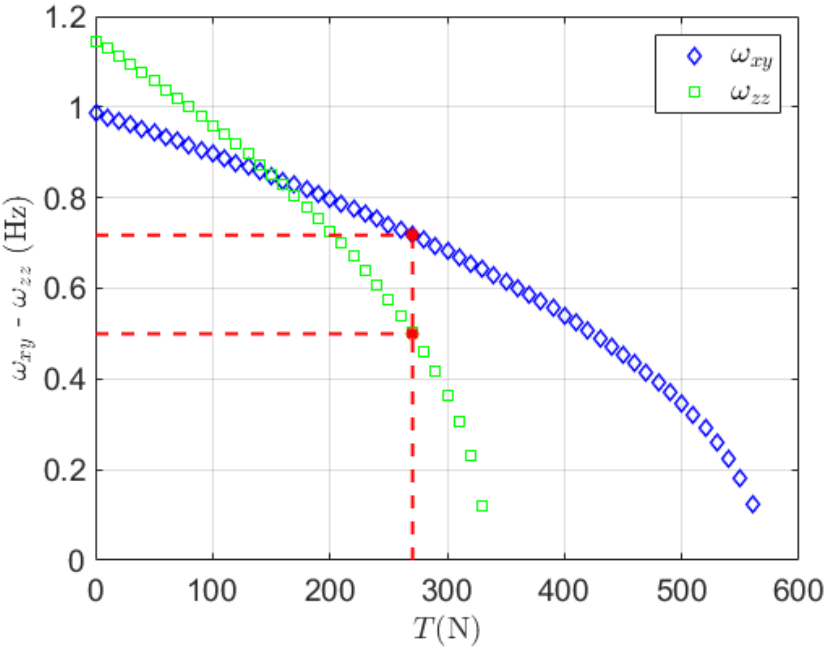

Figure 2.16. When $m_p/m_{max} = 0.50$, the changes in ω_{xy} and ω_{zz} with respect to T. At the intersection of the horizontal and vertical red dashed curves, $T_o = 270.5$ N, $\omega_{xy} = 0.7171$ Hz and $\omega_{zz} = 0.4997$ Hz.

Similarly, Figure 2.17 shows the change in ω_u with respect to T. Since $T_{cr,u}$ is significantly larger than $T_{cr,xy}$ and $T_{cr,zz}$, ω_u is slightly decreased when T is increased to T_o.

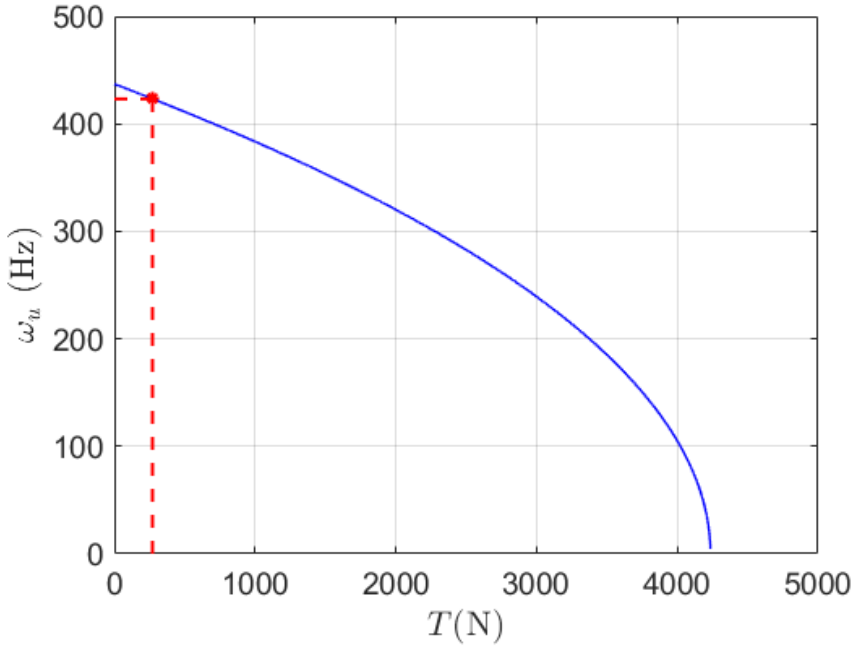

Figure 2.17. When $m_p/m_{max} = 0.50$, the change in ω_u with respect to T. At the intersection of the horizontal and vertical red dashed curves, $T_o = 270.5$ N and $\omega_u = 423.2$ Hz.

In Figure 2.16 and Figure 2.17, the intersection points of the horizontal and vertical red dashed curves show that when $T_o = 270.5$ N, $\omega_{xy} = 0.7171$ Hz, $\omega_{zz} = 0.4997$ Hz and $\omega_u = 423.2$ Hz. Hence, $\omega_{xy}/\omega_u = 0.0017$ for translational vibrations and $\omega_{zz}/\omega_u = 0.0012$ for torsional vibrations. The isolation bandwidth starts at $\sqrt{2}\omega_{zz} = 0.71$ Hz and extends up to $\omega_u = 4232$ Hz for torsional vibrations while the isolation bandwidth starts at $\sqrt{2}\omega_{xy} = 1.01$ Hz and extends up to $\omega_u = 423.2$ Hz for translational vibrations. Since $\omega_{zz}/\omega_u < \omega_{xy}/\omega_u$, the system has a better isolation performance for torsional vibrations.

To better illustrate the advantage of using thin-walled cylinders with a thicker outer radius in the middle part of the stepped beams, this case can be compared to the case where the middle part of the stepped beams has the same outer radius but a solid cross section. Thus, the isolator with elastic uniform beams (Isolator 1), the isolator with elastic stepped

beams having a middle part with a solid cross-section (Isolator 2) and the isolator with elastic stepped beams having a middle part with a hollow cross-section (Isolator 3) can be compared in terms of the maximum payload mass that they can support (m_{max}) and the isolation bandwidth for translational (ω_{xy}/ω_u) and torsional (ω_{zz}/ω_u) vibrations. Table 2.4 shows the values of ω_{xy}/ω_u and ω_{zz}/ω_u for all systems when $m_p/m_{max} = 0.50$ and $T = T_o$.

Table 2.4. The values of ω_{xy}/ω_u and ω_{zz}/ω_u for all systems when $m_p/m_{max} = 0.50$ and $T = T_o$.

	Isolator 1	**Isolator 2**	**Isolator 3**
$\boldsymbol{m_{max}}$ **(kg)**	41.52	51.59	50.42
$\boldsymbol{T_o}$ **(N)**	200.7	288.5	270.5
$\boldsymbol{\omega_{xy}}$ **(Hz)**	0.7231	0.7064	0.7171
$\boldsymbol{\omega_{zz}}$ **(Hz)**	0.4984	0.4985	0.4997
$\boldsymbol{\omega_u}$ **(Hz)**	283.2	299.6	423.2
$\boldsymbol{\omega_{xy}/\omega_u}$	0.0026	0.0024	0.0017
$\boldsymbol{\omega_{zz}/\omega_u}$	0.0018	0.0017	0.0012

Comparing Isolator 1 and Isolator 2 with each other, the above results show that when the middle part is made thicker, the system can achieve a larger isolation bandwidth for translational and torsional vibrations. Moreover, Isolator 2 has a greater payload carrying capacity due to the stepped beams. However, it is seen that thin-walled cylinders (Isolator 3) provide the largest isolation bandwidth as ω_u is significantly larger than the other two cases. Besides, the payload carrying capacity is very close to Isolator 2. For these reasons, the analytical, numerical and experimental studies in the following sections are focused on the systems consisting of elastic stepped beams with a thin-walled cylinder in their middle part.

2.2. Finite Element Models

In this section, the finite element models of the buckling and vibration of a small-scale horizontal-motion isolator constructed for experimental use are developed on ABAQUS, and the numerical results are used to verify the analytical results obtained from the previous section. Figure 2.18(a) shows the finite element model of the small-scale isolator consisting of three elastic stepped beams, a tension wire in the center, a top platform connected to the stepped beams and a point mass represented with a green square attached to the top platform. The long cylindrical part on the flat cylindrical plate is used to stretch the wire which is longer than the stepped beams. The inside of this part is designed as hollow to connect the wire to the inner surface of the part (see Figure 2.18(b)). The point mass/inertia on top of the cylindrical part can be used to define the total mass and mass moment of inertia of the top platform and the payload carried. The parts of the stepped beams (thin beams, thin-walled cylinder and fasteners) are modelled with the continuum element type C3D20R, and the tension wire is modelled with the beam element type B31. On the other hand, since the top platform is considerably stiffer than the stepped beams, it can be modelled with the rigid quadrilateral element type R3D4 instead of using the element type C3D20R in order to decrease the analysis times of the models.

If the design parameters of the system are known, the maximum payload mass that the system can support (m_{max}) can be determined by finding the first critical buckling load ($P_{cr,1}$) of the system. Then, the critical buckling tensions ($T_{cr,xy}$, $T_{cr,zz}$ and $T_{cr,u}$) and the horizontal natural frequencies (ω_{xy}, ω_{zz} and ω_u) can be found in a similar way. Finally, the isolation bandwidth of the system for translational and torsional vibrations can be found from the differences $\sqrt{2}\omega_{xy}$ - ω_u and $\sqrt{2}\omega_{zz}$ - ω_u, respectively. Moreover, isolation bandwidth for translational and torsional vibrations can be maximized by minimizing ω_{xy}/ω_u and ω_{zz}/ω_u, respectively.

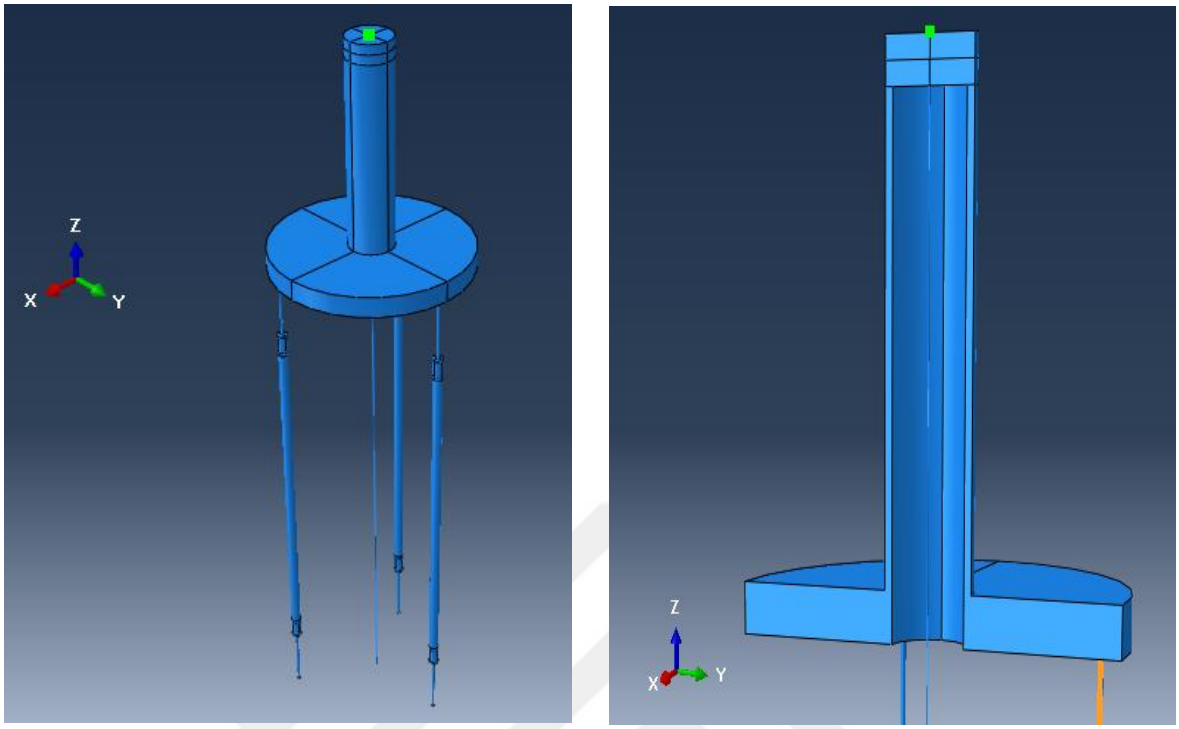

(a) (b)

Figure 2.18. (a) Finite element model of the small-scale isolator. The green square on top of the cylindrical part is a point mass/inertia property representing the total mass and mass moment of inertia of the top platform and the payload carried, (b) The section view of the isolator shows that the wire is connected to the top surface of the hollow cylindrical part so that the wire becomes longer than the stepped beams

The design parameters of the parts used in the stepped beams are shown in Table 2.5, and the total length of the stepped beams used in the system is determined as $l = 275$ mm. Since the thin beams and fasteners are made of steel, and the thin-walled cylinders are assumed to be made of brass, their material properties (E and ρ) are taken according to average values found in the literature. In addition, since the thin beams are passed into the fasteners by a certain amount, the length of the thin beams given in the below table is measured from the outside of the fasteners. On the other hand, the fasteners are passed into the thin-walled cylinders in the form of dowels in a way that their thick ends remain 1 mm outside the thin-walled cylinder. For this reason, the terms r_o and r_i in the table represent the outer and inner radius of the parts, respectively.

Table 2.5. Design parameters of the stepped beams used in the small-scale isolator.

	Thin Beam	**Fastener**	**Thin-Walled Cylinder**
$\boldsymbol{E}$ **(GPa)**	180	180	105
$\boldsymbol{\rho}$ **(kg/m^3)**	7800	7800	8500
$\boldsymbol{l}$ **(mm)**	35	12	203
$\boldsymbol{r_o}$ **(mm)**	0.75	2.585	2.585
$\boldsymbol{r_i}$ **(mm)**	-	0.75	2.415

In addition, the length of the wire is measured as $l_s = 385$ mm ($l_s/l = 1.4$), the diameter of the top platform as 105 mm, and the beam distances to the central axis as $\bar{r} = 47$ mm ($\bar{r}/l = 0.1709$). Table 2.6 shows the design parameters of the top platform.

Table 2.6. Design parameters of the top platform.

$\boldsymbol{m_0}$ **(kg)**	1.024
$\boldsymbol{J_0}$ **(kg.m^2)**	0.0116
$\boldsymbol{P_0}$ **(N)**	10.04
$\boldsymbol{\kappa_0}$ **(mm)**	106.4

2.2.1. Buckling of the Small-Scale Isolator

When gravity is not taken into account and the wire is not stretched, Figure 2.19 shows the buckling of the small-scale isolator under the action of a vertical force P. The critical value of this force is $P_{cr,1}$.

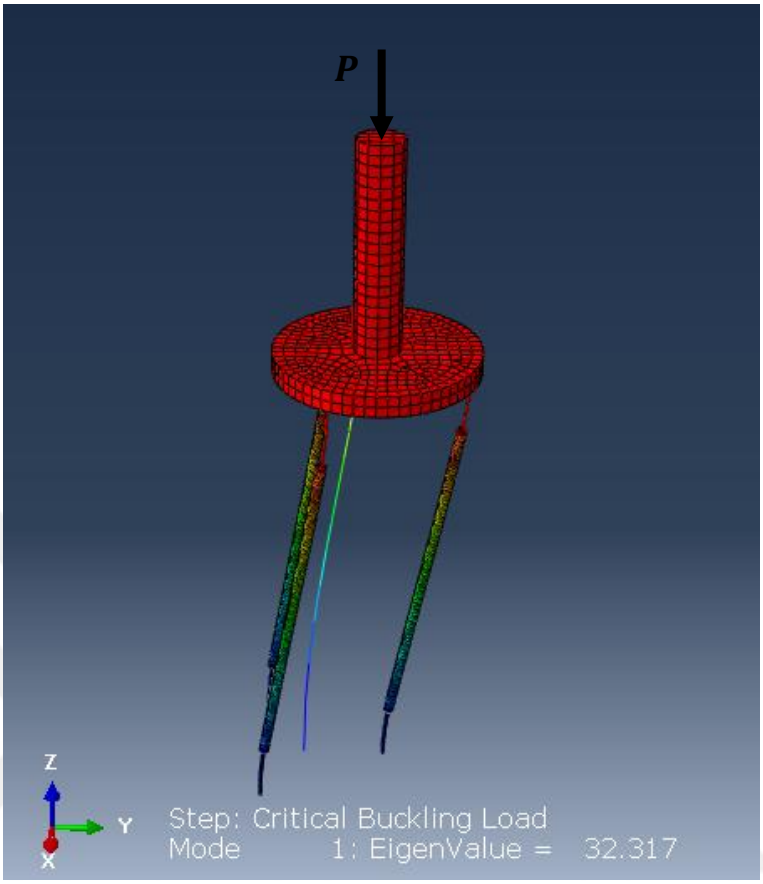

Figure 2.19. Buckling of the small-scale isolator under the action of a vertical force P.

When $P_{cr,1}$ is known, m_{max} can be found from Equation 2.20. Table 2.7 shows the comparison of the analytical and numerical results for $P_{cr,1}$ and m_{max}. It is seen from the below table that the finite element results verify the analytical results.

Table 2.7. The comparison of the analytical and finite element results for $P_{cr,1}$ and m_{max}.

	Analytical	**Finite Element**
$\boldsymbol{P_{cr,1}}$ **(N)**	32.54	32.32
$\boldsymbol{m_{max}}$ **(kg)**	2.293	2.270

When gravity is taken into account and the wire is stretched with a tension force T, Figure 2.20(a) shows the lateral buckling of the system. The critical value of this tension force T is represented with $T_{cr,xy}$. The difference between the buckling case shown in Figure 2.19 and the case in Figure 2.20(a) is that while the force P is applied to the top platform in the former case, the force T is applied to the wire in the latter case. On the other hand, Figure 2.20(b) shows the torsional buckling of the system when the tension force T is equal to $T_{cr,zz}$. Since $T_{cr,xy} < T_{cr,zz}$, the system buckles in the lateral mode.

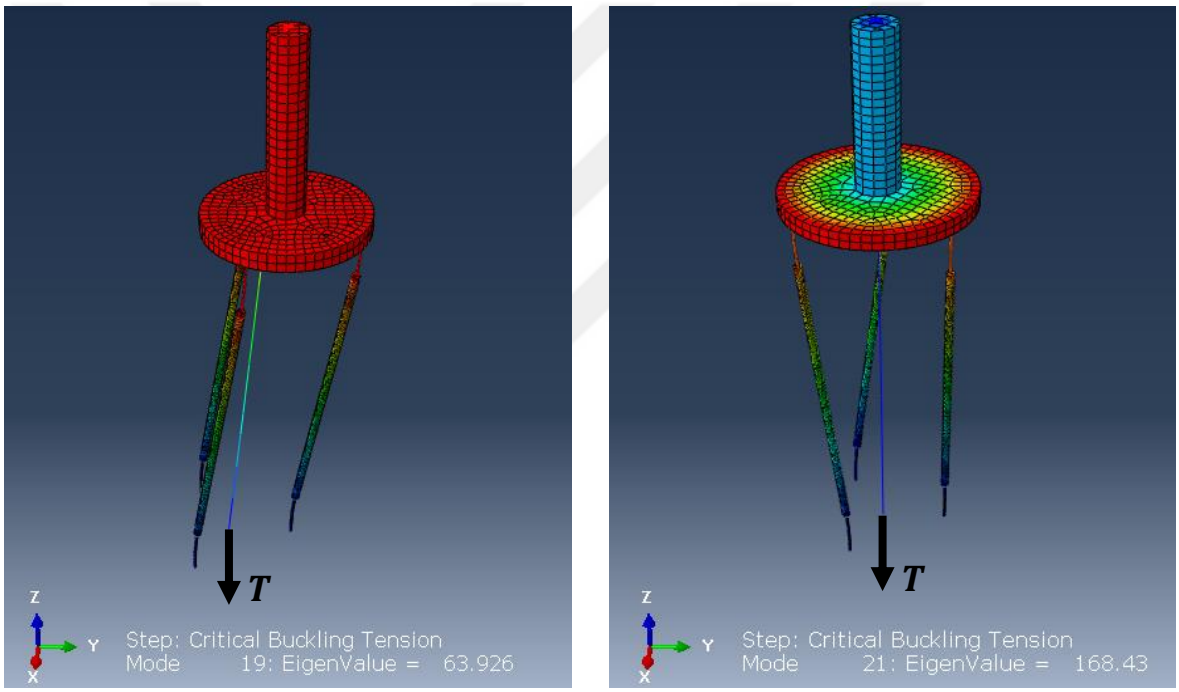

(a) (b)

Figure 2.20. (a) Lateral buckling of the small-scale isolator under the action of a tension force T, (b) Torsional buckling of the small-scale isolator under the action of a tension force T.

Moreover, Figure 2.21 shows the buckling of the system which corresponds to a higher critical value of the tension force T represented with $T_{cr,u}$.

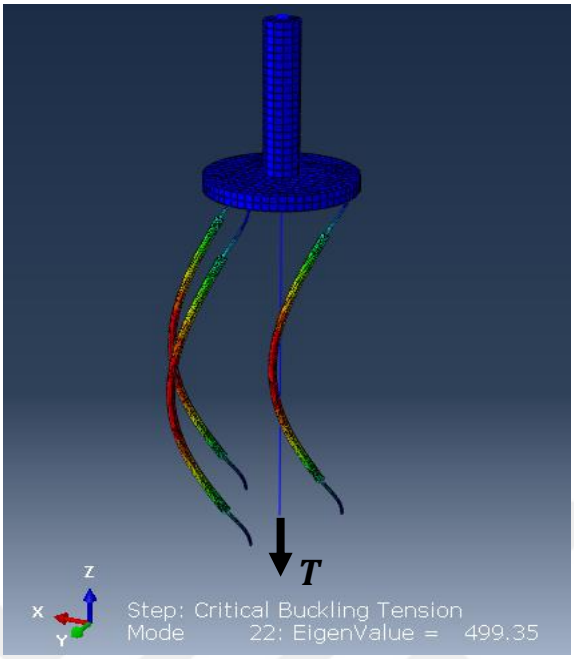

Figure 2.21. Buckling of the small-scale isolator under the action of a tension force T which corresponds to a higher mode.

Figure 2.20 and Figure 2.21 show that the values of $T_{cr,xy}$, $T_{cr,zz}$ and $T_{cr,u}$ (eigenvalues) correspond to the 19th, 21st and 22nd buckling modes of the system, respectively. This condition results from the fact that the other eigenvalues correspond to the critical buckling loads of the wire. However, ABAQUS prompts these eigenvalues as negative numbers because the wire is under tension. This also implies that a wire or a beam cannot be physically buckled when tensioned. Table 2.8 shows the comparison of the analytical and finite element results for $T_{cr,xy}$, $T_{cr,zz}$ and $T_{cr,u}$.

Table 2.8. The comparison of the analytical and finite element results for $T_{cr,xy}$, $T_{cr,zz}$ and $T_{cr,u}$.

	Analytical	**Finite Element**
$\boldsymbol{T_{cr,xy}}$ **(N)**	64.95	63.93
$\boldsymbol{T_{cr,zz}}$ **(N)**	169.5	168.4
$\boldsymbol{T_{cr,u}}$ **(N)**	501.2	499.4

When a payload mass m_p is supported by the system, $T_{cr,xy}$, $T_{cr,zz}$ and $T_{cr,u}$ values can be found similarly. If $m_p/m_{max} = 0.25$, Figure 2.22(a) and Figure 2.22(b) show the lateral and torsional buckling of the system, respectively. Due to the payload weight, $T_{cr,xy}$ and $T_{cr,zz}$ values decrease by certain amounts. While the decrease in $T_{cr,zz}$ is equal to $m_p g$, it is more than $m_p g$ for $T_{cr,xy}$.

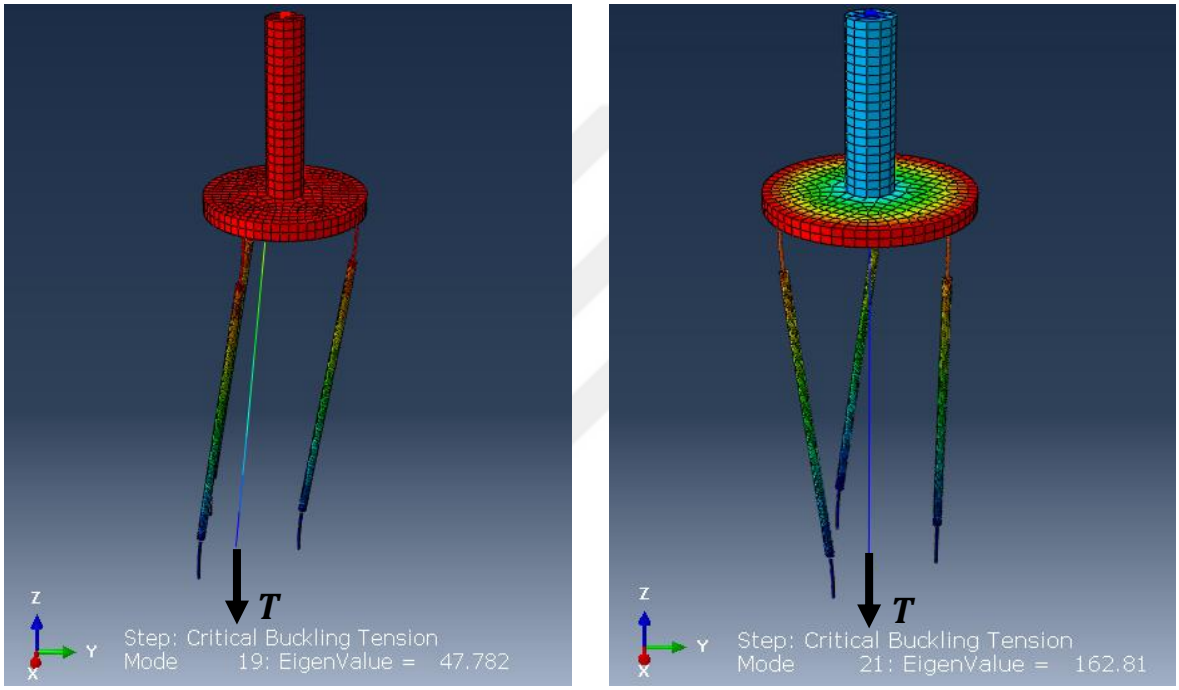

(a) (b)

Figure 2.22. When $m_p/m_{max} = 0.25$, (a) Lateral buckling of the small-scale isolator under the action of a tension force T, (b) Torsional buckling of the small-scale isolator under the action of a tension force T.

Similarly, Figure 2.23 show the buckling of the system corresponding to a higher mode, and the decrease in $T_{cr,u}$ is equal to $m_p g$.

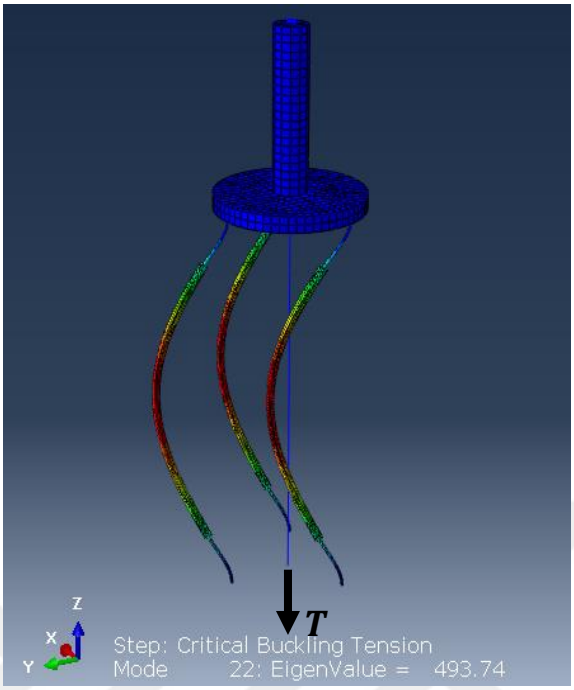

Figure 2.23. When $m_p/m_{max} = 0.25$, buckling of the small-scale isolator under the action of a tension force T which corresponds to a higher mode.

When $m_p/m_{max} = 0.25$, Table 2.9 shows the comparison of the analytical and finite element results for $T_{cr,xy}$, $T_{cr,zz}$ and $T_{cr,u}$.

Table 2.9. When $m_p/m_{max} = 0.25$, the comparison of the analytical and finite results for $T_{cr,xy}$, $T_{cr,zz}$ and $T_{cr,u}$.

	Analytical	**Finite Element**
$\boldsymbol{T_{cr,xy}}$ **(N)**	48.77	47.78
$\boldsymbol{T_{cr,zz}}$ **(N)**	163.9	162.8
$\boldsymbol{T_{cr,u}}$ **(N)**	495.5	493.7

2.2.2. Vibration of the Small-Scale Isolator

In this section, the horizontal natural frequencies ω_{xy}, ω_{zz} and ω_u are determined at several values of the tension force T when $m_p = 0.25m_{max}$. Table 2.10 shows the analytical and finite element results for ω_{xy}, ω_{zz} and ω_u.

Table 2.10. When $m_p/m_{max} = 0.25$, the analytical and finite element (FE) results of ω_{xy}, ω_{zz} and ω_u with respect to T.

T (N)	ω_{xy} (Hz)		ω_{zz} (Hz)		ω_u (Hz)	
	Analytical	**FE**	**Analytical**	**FE**	**Analytical**	**FE**
0	1.026	1.019	1.423	1.419	147.8	145.5
10	0.9157	0.9076	1.379	1.375	146.3	144.1
20	0.7895	0.7789	1.334	1.330	144.8	142.6
30	0.6382	0.6232	1.287	1.283	143.3	141.2
35	0.5469	0.5243	1.263	1.258	142.5	140.4
40	0.4366	0.4064	1.238	1.234	141.8	139.7
45	0.2864	0.2304	1.213	1.209	141.0	138.9

According to the above results, when $T = 35$ N, the lowest natural frequency ω_{xy} approaches 0.5 Hz. Under this condition, Figure 2.24, Figure 2.25 and Figure 2.26 show the vibrational modes of the system at $\omega_{xy} = 0.5243$ Hz, $\omega_{zz} = 1.263$ Hz and $\omega_u = 140.4$ Hz, respectively. Similarly, the natural frequencies of the system can be investigated graphically. Figure 2.24 shows that when $m_p/m_{max} = 0.25$ and $T = 35$ N, it is found that $\omega_{xy} = 0.5243$ Hz, and the isolation bandwidth for translational vibrations starts at $\sqrt{2}\omega_{xy} = 0.74$ Hz.

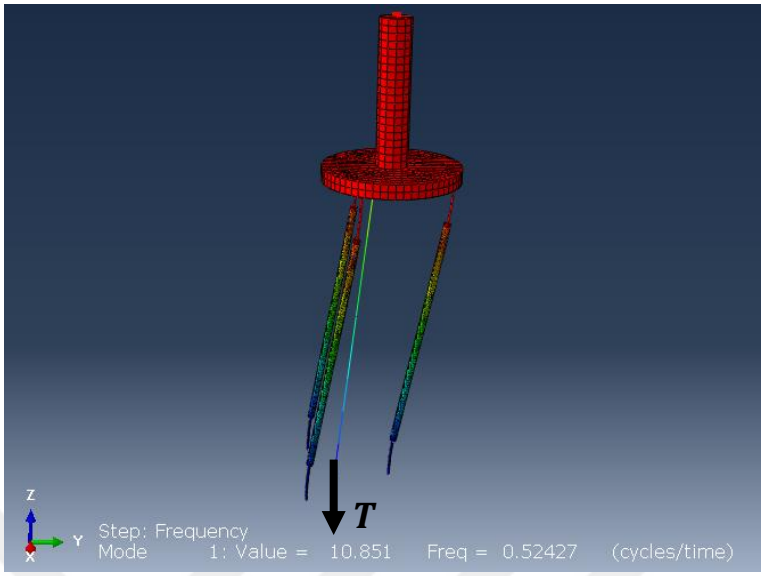

Figure 2.24. When $m_p/m_{max} = 0.25$ and $T = 35$ N, lateral vibrational mode of the system at $\omega_{xy} = 0.5243$ Hz.

On the other hand, Figure 2.25 shows that at the same tension force T, $\omega_{zz} = 1.258$ Hz, and the isolation bandwidth for torsional vibrations starts at $\sqrt{2}\omega_{zz} = 1.78$ Hz.

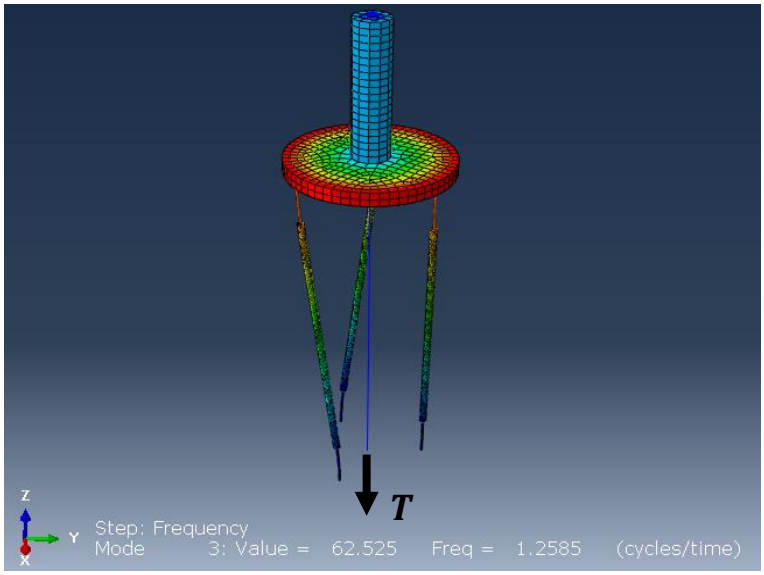

Figure 2.25. When $m_p/m_{max} = 0.25$ and $T = 35$ N, torsional vibrational mode of the system at $\omega_{zz} = 1.258$ Hz.

Figure 2.26 shows that the upper limit of the isolation bandwidth is determined as $\omega_u = 140.4$ Hz. Hence, it is obtained that $\omega_{xy}/\omega_u = 0.5243/140.4 = 0.0037$ and $\omega_{zz}/\omega_u = 1.258/140.4 = 0.0090$. Since $\omega_{xy}/\omega_u < \omega_{zz}/\omega_u$, the system has a better isolation performance for translational vibrations.

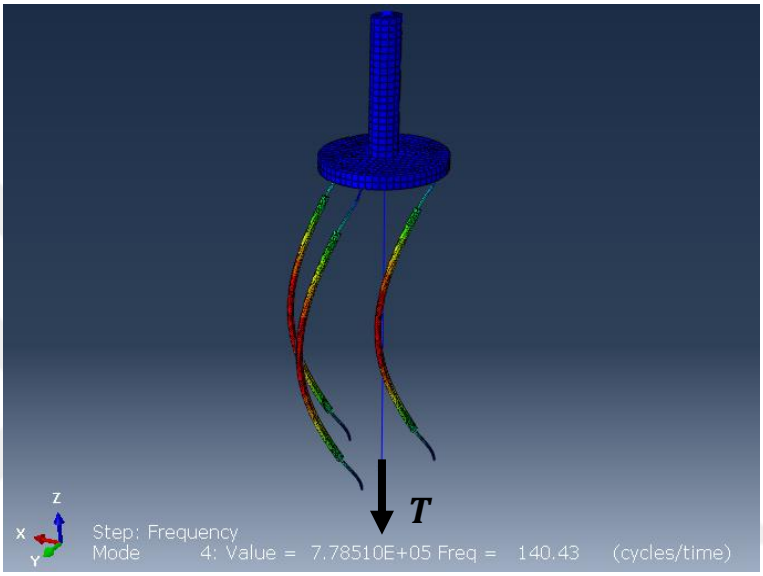

Figure 2.26. When $m_p/m_{max} = 0.25$ and $T = 35$ N, vibrational mode of the system at $\omega_u = 140.4$ Hz.

Alternatively, the isolation bandwidth of the system can be determined by analyzing the frequency spectrum of the system. Under the same conditions ($m_p/m_{max} = 0.25$ and $T = 35$ N), Figure 2.27(a) and Figure 2.27(b) show that a harmonic driving force $F(t)$ and moment $M(t)$ in the form of complex exponential functions $F(t) = F_0 e^{j\omega t}$ and $M(t) = M_0 e^{j\omega t}$ are applied to the top platform, respectively. The terms F_0 and M_0 represent the maximum amplitude of the applied force and moment, and ω stands for the driving frequency. It can be seen from these figures that $F(t)$ and $M(t)$ can be applied parallel to the horizontal y-axis (or x-axis) and parallel to the vertical z-axis, respectively. The driving force $F(t)$ is applied towards the central axis of the system in order to create only translational movements. Thus, when the system responses are analyzed in the steady-state conditions, the lateral and angular displacements of the payloads represented by the green

squares in these figures can also be assumed as complex exponential functions $y(l,t) = Ye^{j\omega t}$ and $\theta(l,t) = \Theta e^{j\omega t}$, respectively where the terms Y and Θ are the maximum amplitudes of the forced responses. In the FE models in ABAQUS, the mode-based steady-state dynamics procedure, which is a linear perturbation method, is used.

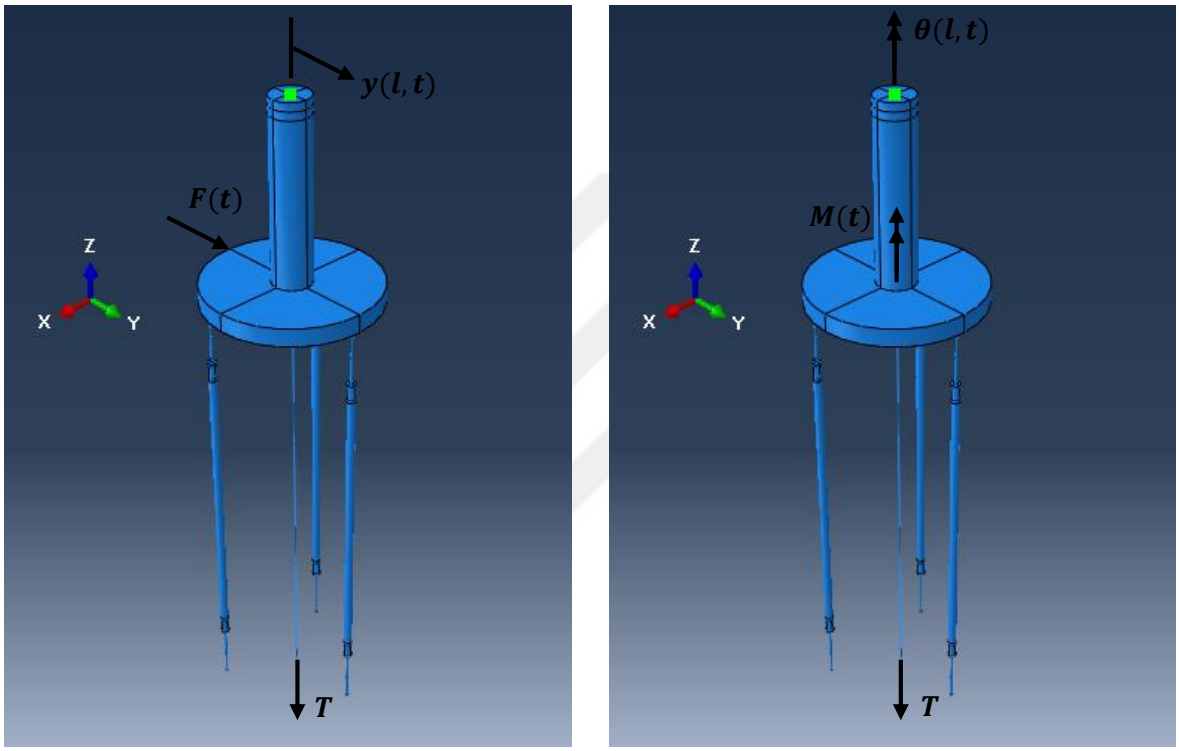

(a) (b)

Figure 2.27. (a) A harmonic driving force $F(t)$ can be applied to the top platform parallel to the horizontal y-axis (or x-axis), (b) A harmonic driving moment $M(t)$ can be applied to the top platform about the central axis of the system parallel to the vertical z-axis.

When the system is forced to statically deform along the y-axis with the force $F_0 = 0.1$ N, the lateral displacement of the top platform is approximately 5 mm. This static displacement value can be considered as reasonable in order for the system to have certain elasticity under various loading conditions. When the harmonic driving force $F(t) = F_0 e^{j\omega t}$

is applied to the system within the frequency range $0.1 \leq \omega \leq 250$ Hz, Figure 2.28 shows the changes in Y with respect to ω obtained from the analytical and FE models.

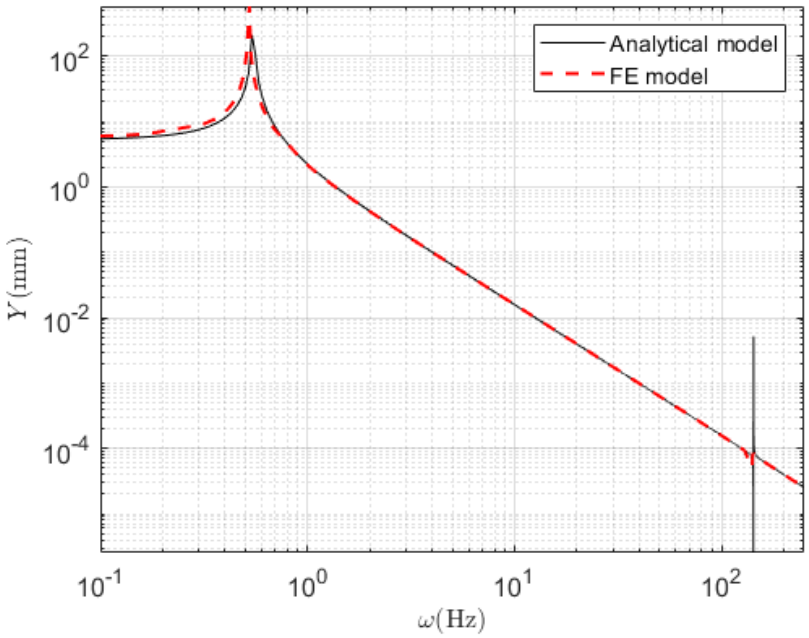

Figure 2.28. The changes in Y (mm) with respect to ω (Hz) obtained from the analytical and FE models.

Similarly, when the system is forced to statically deform about the z-axis with the moment $M_0 = 0.1$ N. m, the angular displacement of the top platform is approximately 5 °. This static displacement value can be considered as reasonable in order for the system to have certain elasticity under various loading conditions. When the harmonic driving moment $M(t) = M_0 e^{j\omega t}$ is applied to the system within the frequency range $0.1 \leq \omega \leq 250$ Hz, Figure 2.29 shows the changes in Θ with respect to ω obtained from the analytical and FE models.

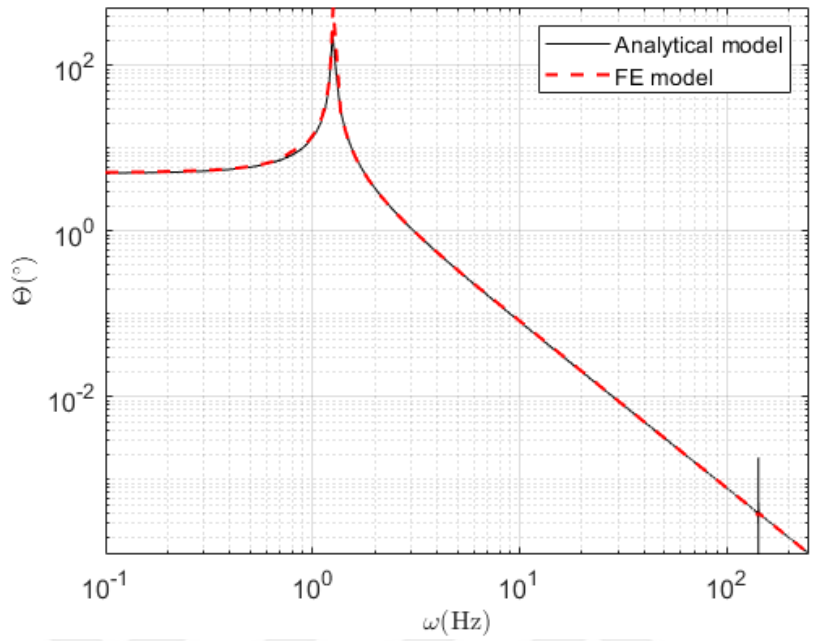

Figure 2.29. The changes in Θ (°) with respect to ω (Hz) obtained from the analytical and FE models.

Figure 2.28 and Figure 2.29 are plotted in a logarithmic scale to better visualize where the system has resonance frequencies. Both figures show that the peak values of Y and Θ occur at regions where $\omega = \omega_{xy}$ and $\omega = \omega_{zz}$ as shown in Table 2.10. On the other hand, the figures also show that the analytical values of Y and Θ change abruptly as the excitation frequency ω passes through the upper natural frequency ω_u, experiencing initially a sharp decrease and then a sharp increase. To bound the peak values around the resonance frequencies, a structural damping constant of 0.01 is assumed in the FE models. Thus, these sharp changes are not observed for the FE models in these figures. When the results obtained from the buckling, frequency and modal analyses are considered together, it is concluded that the analytical models are verified by the FE models.

2.3. Experimental Validations

In this section, the analytical results are compared with the results obtained from the experimental studies performed on the small-scale horizontal-motion isolator shown in Figure 2.30. In this figure, the system is in an unloaded state. The lower and upper thin parts and the middle thick part of the stepped beams are connected to each other by means of the fasteners as described in Section 2.1. The tension wire at the center of the system is stretched with a piece of a sigma profile that is placed vertically on the top platform, and the tension mechanism at the center of the base platform is used to pull the wire at different forces. The beams are fixed to the base and top platform with the mandrels at both ends.

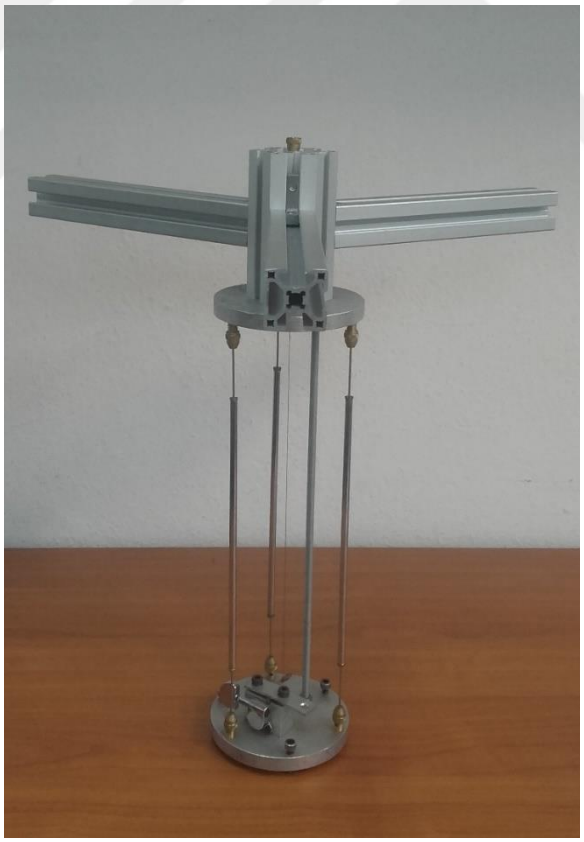

Figure 2.30. Horizontal-motion small-scale isolator.

Since the elastic stepped beams used in the system have circular cross-sections, the system has the same translational natural frequencies ($\omega_{xy} = \omega_x = \omega_y$). On the other hand, the torsional natural frequency ω_{zz} can be adjusted to very low values by changing the overall mass polar moment of inertia of the system. The payloads on the horizontal sigma profiles connected to the vertical sigma profile can be positioned at different distances from the center of the system, and the inertia adjustment of the system can be made. (see Figure 2.30).

The experimental maximum payload mass that the system can support can be found by measuring ω_{xy} values under different payloads. When there is no tension force in the wire, ω_{xy} can be approximated as

$$\omega_{xy} \approx \sqrt{\frac{k_0}{m_0+m_p}}\sqrt{1-\frac{P_0+P}{P_{cr,1}}} \tag{2.67}$$

where the term k_0 represents the translational stiffness of the system when there is no axial compressive loads on the beams ($P_0 = P = T = 0$). For the unloaded ($m_p = 0$) and loaded ($m_p > 0$) conditions, the values of ω_{xy} can be represented as $\omega_{xy,0}$ and $\omega_{xy,1}$, respectively. Since $P_0 = m_0 g$ and $P = m_p g$, the first critical buckling force of the system can be experimentally obtained from Equation 2.67 as

$$P_{cr,1} = \left(m_0 + \frac{m_p}{1-\left(1+\frac{m_p}{m_0}\right)\left(\frac{\omega_{xy,1}}{\omega_{xy,0}}\right)^2} \right) g \tag{2.68}$$

The $\omega_{xy,0}$ and $\omega_{xy,1}$ values can be found by measuring the duration at which the system completes 30 oscillations which can be initialized by pulling the top platform horizontally by 5 mm and releasing it to freely vibrate. For instance, if the duration of 30

oscillations made by the top platform is measured as 15 seconds with a stopwatch, the period of the system vibrations is found as 0.5 seconds. In this case, $\omega_{xy,0}$ (or $\omega_{xy,1}$) is equal to 2 Hz. Experimental measurements show that when $m_p = 0$, $\omega_{xy,0} = 1.39$ Hz and when $m_p = 0.453$ kg, $\omega_{xy,1} = 1.03$ Hz. If these values are substituted into Equation 2.68, then $P_{cr,1} = 31.6$ N. Since $P_0 = 10.0$ N, it is found from Equation 2.20 that $m_{max} = 2.20$ kg. These results are 2.8 % and 4.0 % lower than the analytical results ($P_{cr,1} = 32.5$ N and $m_{max} = 2.29$ kg), respectively. These differences may result from timing errors in the measurements made with the stopwatch, the uncertainties in the design parameters, the negligence of frictional effects and some elasticity of the mandrels used to tighten the beams under axial compressive loads. However, it is considered that the results obtained from Equation 2.69 can give accurate estimates about the maximum payload mass that the isolator can carry. The magnitude of the tension force applied to the top platform can be changed by pulling the wire in different amounts with the tension mechanism shown in Figure 2.31.

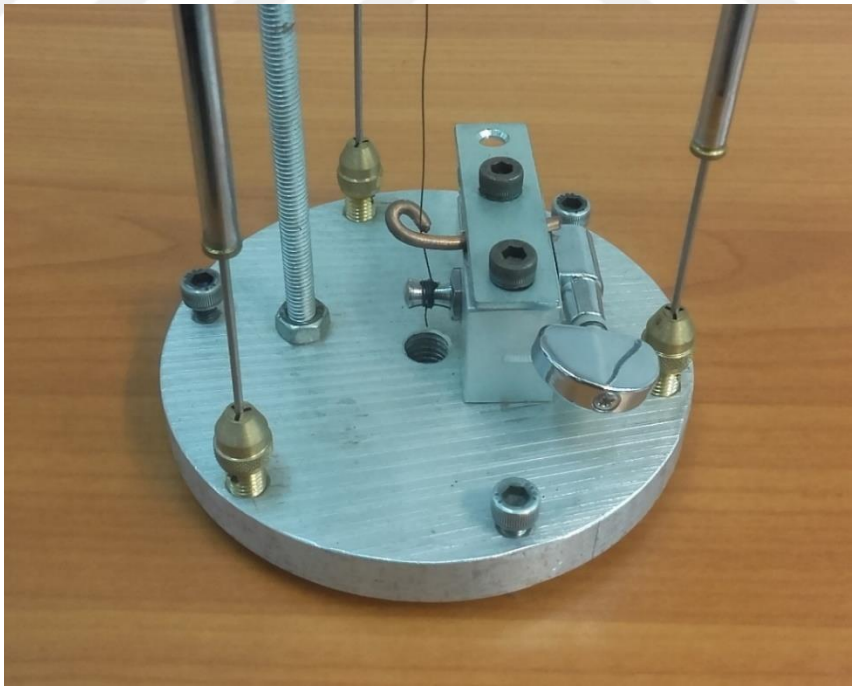

Figure 2.31. View of the tension mechanism. Since the wire in the center is not stretched, it looks wavy. when the wire is stretched, it straightens and the initial translational and torsional natural frequencies of the isolator decrease.

In order to reduce the lowest natural frequency of the isolator (ω_{xy} or ω_{zz}) to 0.5 Hz under different loading conditions, the magnitude of the tension force must be known. Since the tension wire is fixed at both ends as shown in Figure 2.30, its natural frequencies can be found as

$$\omega_{s,n} = \frac{n\pi c}{l_s} \tag{2.69}$$

In this equation c is the wave speed in the wire and is expressed by the formula $c = \sqrt{T/\rho_s A_s}$ where the terms p_s and A_s are the density and cross-sectional area of the wire, respectively. If $\omega_{s,1}$, which is the fundamental natural frequency of the wire, is expressed in Hz, then it can be written as

$$f_{s,1} = \omega_{s,1}/2\pi \tag{2.70}$$

In this case, the force T is found as

$$T = 4\rho_s A_s {l_s}^2 {f_{s,1}}^2 \tag{2.71}$$

Since the tension wire used is steel, $\rho_s = 7800\ \text{kg}/m^3$ is taken. In addition to this, since the wire diameter is 0.32 mm, the cross-sectional area is found as $A_s = 0.08042\ \text{mm}^2$. When these values are substituted into Equation 2.71, T can be written in Newton units as

$$T = 3.719\ 10^{-4} {f_{s,1}}^2 \tag{2.72}$$

The tension wire frequency $f_{s,1}$ can be found by a software program (PitchPerfect Musical Instrument Tuner) which is used for tuning musical instruments. For this purpose, the microphone of the laptop computer is used. While the wire is under different tension forces, the values of $f_{s,1}$ can be measured by pulling it from its midpoint and then releasing it to vibrate. Hence, T can be obtained from Equation 2.72.

When the system is in no-load state ($m_P = 0$), Figure 2.32 shows the analytical and experimental relationships between ω_{xy} and T. From this figure, it can be seen that the analytical results are verified by the experimental results. As T approaches 60 N, ω_{xy} can be lowered below 0.5 Hz both analytically and experimentally. The intersection point of the horizontal and vertical red-dashed curves corresponds to the analytical case where $\omega_{xy} \cong 0.5$ Hz and $T \cong 58.0$ N. As explained previously, this T value is denoted as T_o.

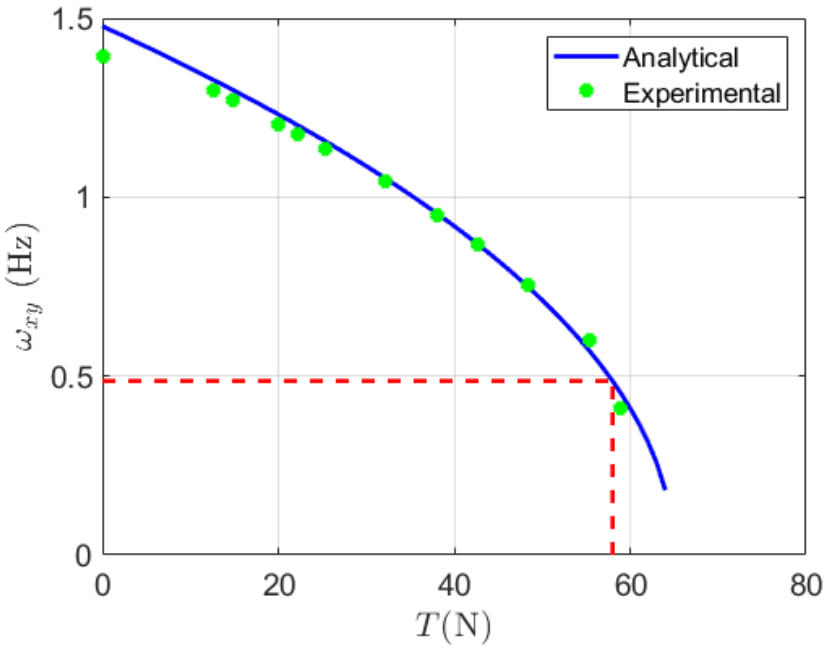

Figure 2.32. When $m_P = 0$, the analytical and experimental relationships between ω_{xy} and T.

Figure 2.32 shows that the horizontal red-dashed line is slightly below 0.5 Hz because the numerical methods find T_o at which $\omega_{xy} \leq 0.5$ Hz or $\omega_{zz} \leq 0.5$ Hz by incrementing the tension force T with a small step size such as $dT = 0.5$ N. Thus, ω_{xy} or ω_{zz} values may be found slightly lower than 0.5 Hz at the numerically found T_o value. In the experiments, when $f_{s,1} = 398$ Hz, Figure 2.32 shows that $T = 58.9$ N and $\omega_{xy} = 0.410$ Hz.

Similarly, the torsional natural frequency ω_{zz} can be estimated by measuring the time the system has completed 30 oscillations around its central axis. To initialize oscillations, the top platform can be rotated about 5 degrees from its equilibrium position and then released to vibrate. When the system is in no-load state ($m_P = 0$), Figure 2.33 shows the analytical and experimental relationships between ω_{zz} and T. Similar to the case shown in Figure 2.32, Figure 2.33 shows that the analytical results are verified by the experimental results.

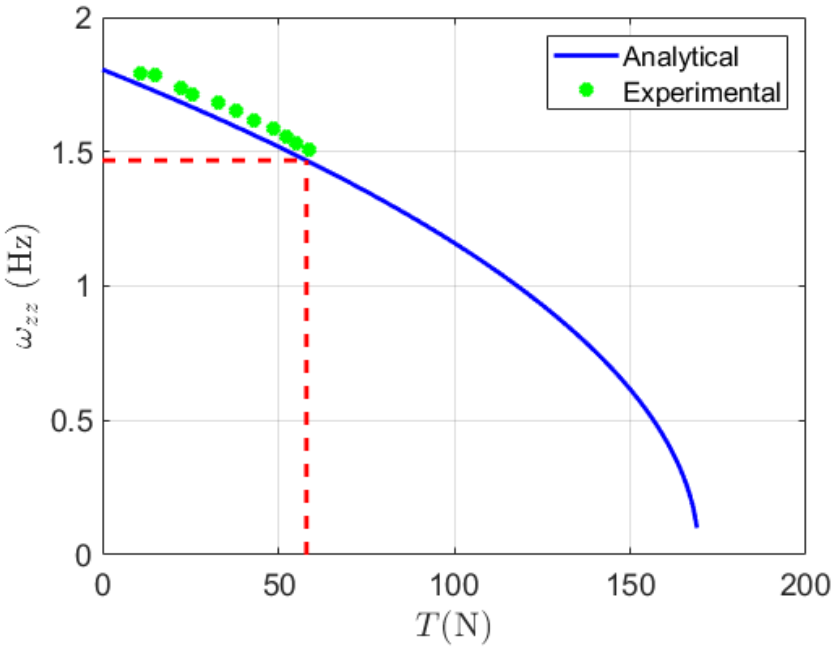

Figure 2.33. When $m_P = 0$, the analytical and experimental relationships between ω_{zz} and T.

When there is a certain payload mass on the top platform, the analytical and experimental relationships between ω_{xy} (ω_{zz}) and T can be investigated. Figure 2.34(a) and Figure 2.34(b) show that the payloads with a total mass $m_p = 0.898$ kg are placed at close and distant positions from the central axis. When the payloads are positioned at a further distance from the central axis, the mass polar moment of inertia of the system increases, and ω_{zz} decreases. In this case, since the payload mass does not change, ω_{xy} does not also change.

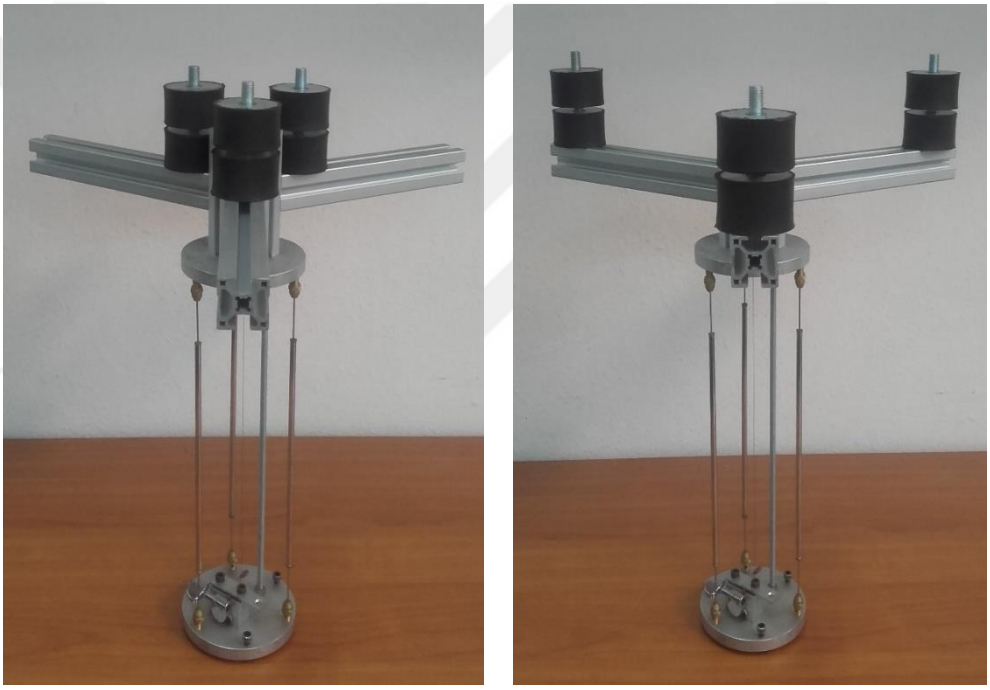

Figure 2.34. (a) View of the isolator with payloads close to the central axis. (b) View of the isolator with payloads distant from the central axis.

When the payloads are positioned on the system as shown in Figure 2.34(a), Figure 2.35 shows the analytical and experimental relationships between ω_{xy} and T. From this figure, it can be seen that the analytical results are validated by the experimental results. When T approaches 26 N, ω_{xy} can be lowered below 0.5 Hz both analytically and experimentally. In the experiments, when $f_{s,1} = 263$ Hz, Figure 2.36 shows that $T = 25.7$ N and $\omega_{xy} = 0.486$ Hz. It is observed that as the tension force in the wire is

increased further, ω_{xy} can be further reduced. For instance, when $f_{s,1} = 289$ Hz and $f_{s,1} = 315$ Hz, it is found that $T = 31.1$ N and $T = 36.9$ N. Under these conditions, it is measured that $\omega_{xy} = 0.382$ Hz and $\omega_{xy} = 0.214$ Hz, respectively.

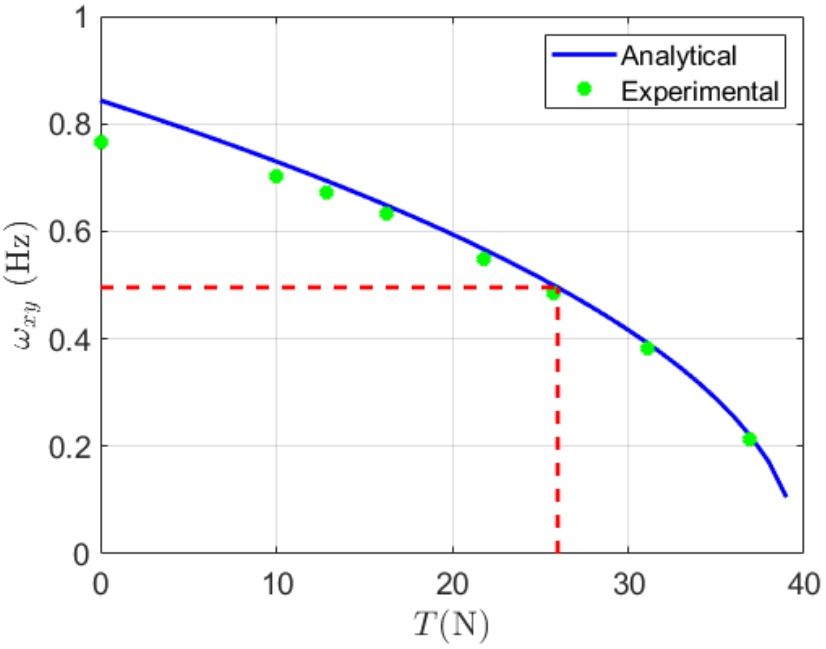

Figure 2.35. When $m_P = 0.898$ kg, the analytical and experimental relationships between ω_{xy} and T.

Under the same payload mass, Figure 2.36 shows the analytical and experimental relationships between ω_{zz} and T. Similar to the case shown in Figure 2.35, Figure 2.36 shows that the analytical results are verified by the experimental results.

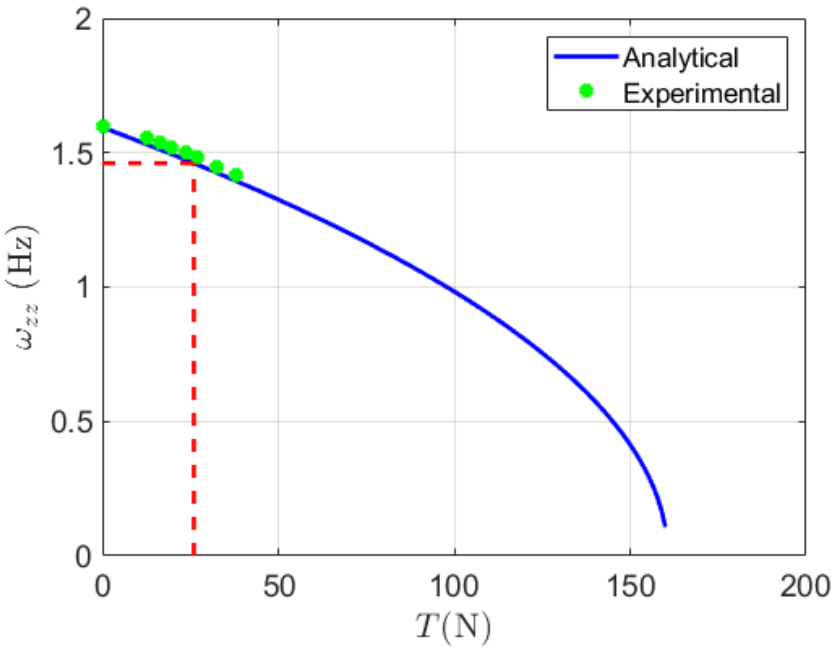

Figure 2.36. When $m_P = 0.898$ kg and the payloads are close to the central axis, the analytical and experimental relationships between ω_{zz} an T.

When the payloads are placed far from the central axis of the system as shown in Figure 2.34(b), Figure 2.37 shows the analytical and experimental relationships between ω_{zz} and T. From this figure, it can be seen that the analytical results are verified by the experimental results. Compared to the case shown in Figure 2.36, Figure 2.37 shows that the ω_{zz} values are reduced as a result of increasing the mass polar moment of inertia of the system.

In all the experiments, it is observed that as T becomes greater than T_o, it becomes more difficult to measure ω_{xy} and ω_{zz} because the system approaches the point of elastic instability. Since the vibration amplitudes increase when this limit is exceeded, the possibility of the system becoming unstable and leaning to one side increases. For this reason, the experimental ω_{zz} values shown in Figure 2.33, Figure 2.36 and Figure 2.37 cannot be measured at T values considerably larger than T_o.

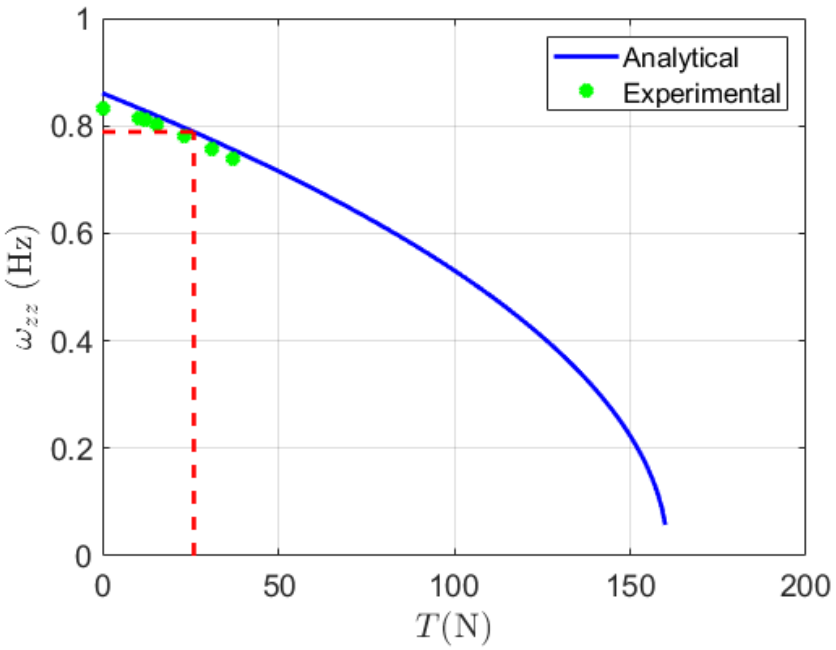

Figure 2.37. When $m_P = 0.898$ kg and the payloads are away from the central axis, the analytical and experimental relationships between ω_{zz} and T.

As in the analytical models, the experimental studies on the small-scale isolator shows that even if the isolator is under different loading conditions, the isolator can reach quasi-zero stiffness by using the tension mechanism. Based on all these findings, it is determined that the established analytical models can be used to calculate the maximum payload mass (m_{max}), critical buckling tension forces ($T_{cr,xy}$, $T_{cr,zz}$ and $T_{cr,u}$) and natural frequencies (ω_{xy}, ω_{zz} and ω_u) of multi-axial horizontal motion isolators.

3. MULTI-AXIS HORIZONTAL-MOTION ISOLATOR

3.1. Analytical Studies

The analytical, numerical and experimental studies in Chapter 2 have shown that the wire tension mechanism can be used to adjust the translational and torsional natural frequencies of horizontal-motion isolators to very low values even if the payload mass changes. In addition to this, the analytical and numerical studies have shown that the isolation bandwidth of these systems can be maximized by using elastic stepped beams having a thin-walled cylinder with a larger outer radius in their middle sections. However, despite all these advantages, it is shown that the lowest natural frequency reaches 0.5 Hz only on the translational or torsional axis, as the translational and torsional natural frequencies do not decrease at the same rate as the tension force in the wire increases.

While the examples in the analytical studies have shown that the torsional natural frequency usually decreases to zero faster than the translational natural frequencies when the payload mass is low, the experimental studies on the small-scale isolator have shown that the translational natural frequencies reach zero faster than the torsional natural frequency in all conditions. For these reasons, while the translational and torsional natural frequencies of the system are reduced simultaneously with the tension mechanism, a unique stiffness adjustment mechanism is developed that allows the torsional natural frequency to be adjusted independently of the translational natural frequencies. In order to achieve this feature, the torsional stiffness of the system must be adjusted by changing the distance of the elastic beams from the central axis of the system. Figure 3.1 shows the schematic structure of the new system when the slider mechanism is included in the system in Figure 2.2.

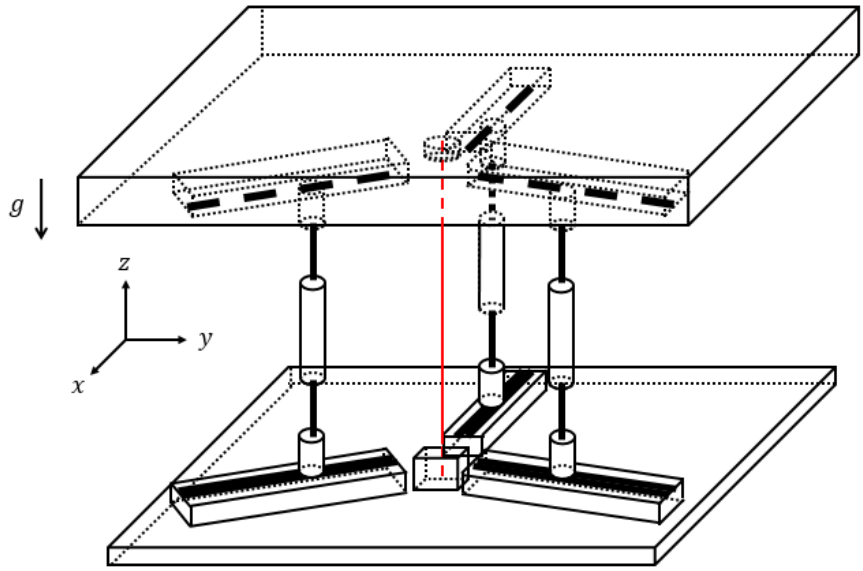

Figure 3.1. The schematic structure of the new system when the slider mechanism is included in the system shown in Figure 2.2.

Figure 3.1 shows that the lower and upper ends of the beams are fixed in the channels of the sliding mechanisms placed equally on the base and top platforms at an angle of 120 degrees. If the number of the beams is increased, the same number of the sliding mechanisms on the base and top platforms must be placed to evenly divide 360 degrees. Depending on the payload being carried, the distance of the beams to the central axis (red wire) can be changed by sliding the beams inside the channels. Figure 3.2 shows the beams in a position farther from the center. In this case, when the axial compressive force on the beams is neglected, the torsional natural frequency of the system increases compared to the situation in Figure 3.1. However, as the axial compressive force on the beams increases, the torsional natural frequency decreases more rapidly than the previous case. On the other hand, the translational natural frequencies are not affected by the changes in the beam positions. Therefore, when the beam distances are increased while the payload and tension force are the same, the torsional natural frequency increases, and the translational natural frequencies do not change. If the beams are brought closer to the center, the torsional natural frequency decreases while the translational natural frequencies remain the same. Thus, when the tension force in the wire is constant, the change in the distance of the beams ($\bar{r}$) only affects

the torsional natural frequency. To reduce (or increase) both natural frequencies at once, the tension of the central wire is increased (or decreased).

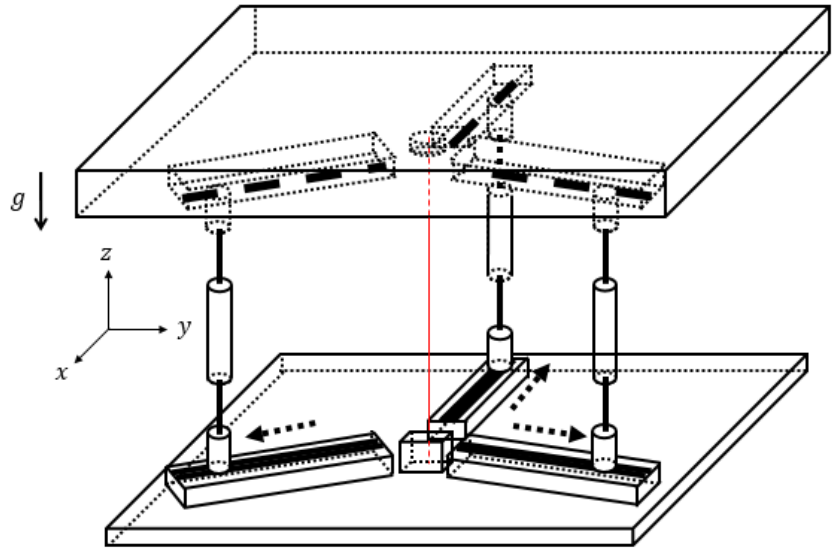

Figure 3.2. The schematic structure of the system when the elastic beams are positioned further from the center by the sliding mechanisms.

The effects of using the sliding mechanisms on the low-frequency isolation performance of horizontal-motion isolators can be examined by considering two different loading cases, and the design parameters can be chosen the same as in the system shown in Figure 2.2. Given that the maximum payload carrying capacity of the system is $m_{max} = 50.4$ kg, the system can support a light ($m_p = 5$ kg) and a heavy ($m_p = 35$ kg) payload mass in the first and second cases, respectively. It can be assumed that the mass polar moment of inertias of these payloads are equal to $J_p = m_p {k_0}^2$ where k_0 is the radius of gyration of the top platform ($k_0 = 160.3$ mm).

In the first case, Figure 3.3 shows the changes in ω_{xy} and ω_{zz} with respect to T at several values of $\bar{r}/\kappa_0$ when $m_p/m_{max} \cong 0.1$. When the ratio $\bar{r}/\kappa_0$ increases, ω_{zz} has larger

values at $T = 0$. On the other hand, ω_{zz} decreases to zero at a faster rate as T increases. If ω_{xy} and ω_{zz} are aimed to be adjusted close to each other around 0.5 Hz, then, the ratio $\bar{r}/\kappa_0$ should be selected between 0.3 and 0.5.

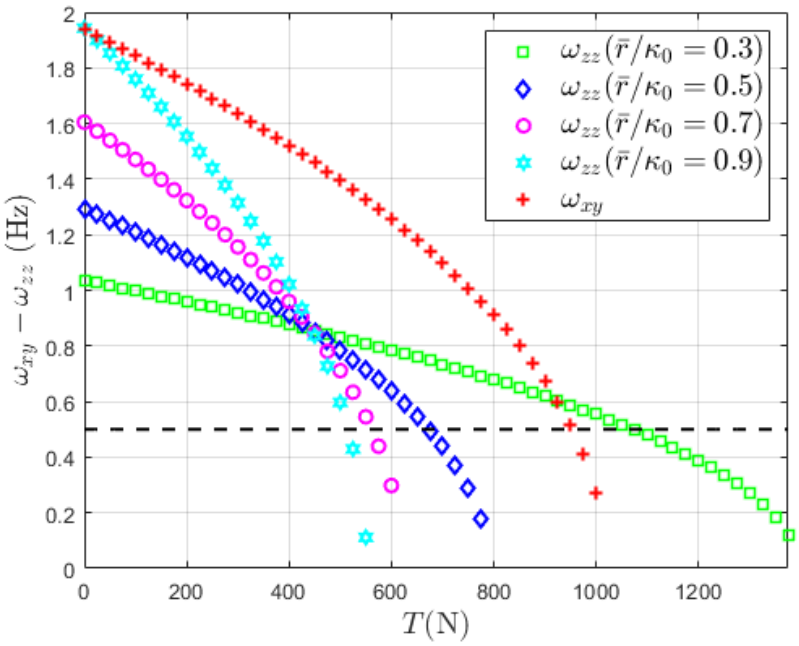

Figure 3.3. The changes in ω_{xy} and ω_{zz} relative to T for various values of $\bar{r}/\kappa_0$ when $m_p/m_{max} \cong 0.1$. The horizontal black dashed line passes through 0.5 Hz.

In the second case where $m_p/m_{max} \cong 0.7$, Figure 3.4 shows the changes in ω_{xy} and ω_{zz} with respect to T at two different values of $\bar{r}/\kappa_0$. According to Figure 3.4, the condition in which ω_{xy} and ω_{zz} are closest to 0.5 Hz is satisfied when the ratio $\bar{r}/\kappa_0$ is chosen to be between 0.7 and 0.9. The detailed analyses on both cases show that when $\bar{r}/\kappa_0 \cong 0.34$ and $\bar{r}/\kappa_0 \cong 0.80$, ω_{xy} and ω_{zz} can be adjusted to 0.5 Hz at the same time when the light and heavy payload masses are carried. Thus, these two results show that adjusting the distance $\bar{r}$ according to the supported payload allows for ω_{xy} and ω_{zz} to be adjusted to 0.5 Hz.

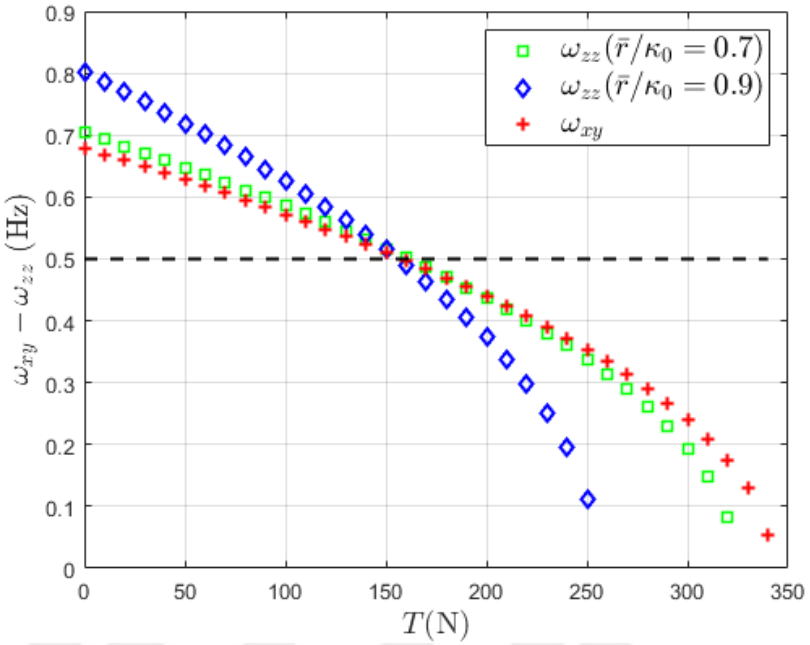

Figure 3.4. The changes in ω_{xy} and ω_{zz} relative to T at several values of $\bar{r}/\kappa_0$ when $m_p/m_{max} \cong 0.7$. The horizontal black dashed line passes through 0.5 Hz.

Figure 3.5 shows that when the system carries a small payload, the stepped beams are positioned close to the central axis.

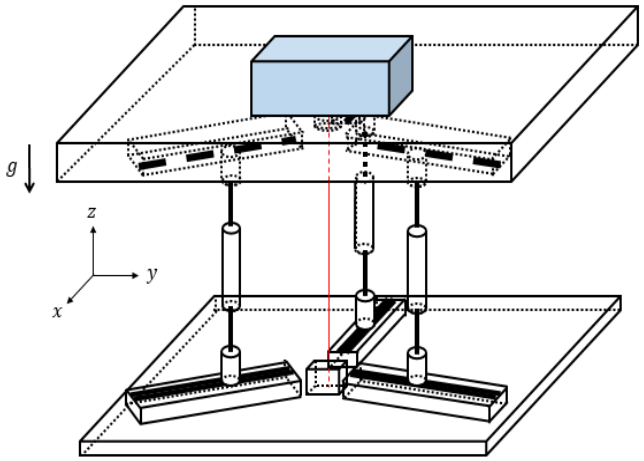

Figure 3.5. The beams are positioned close to the center axis when the supported payload mass is light ($m_p = 5$ kg).

Contrary to this, Figure 3.6 shows that when the system supports a heavy payload mass, the stepped beams are positioned away from the central axis.

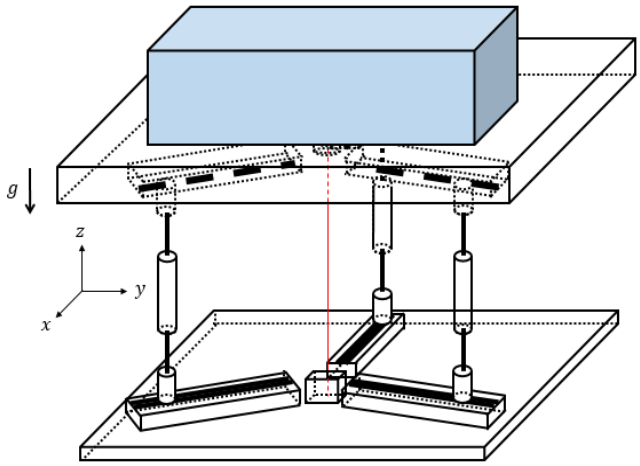

Figure 3.6. The beams are positioned away from the center axis when the supported payload mass is heavy ($m_p = 35$ kg).

Apart from all these situations mentioned above, considering the situation where the center of gravity of the payload carried by the system does not intersect with the central axis of the system, it is possible for the system to collapse sideways due to the moment imbalance that occurs as a result of the eccentric positioning of the payload on the top platform. For this reason, it is thought that keeping the distance of the beams from the central axis above a certain level will reduce the possibility of collapse that may arise from this condition. Thus, the lowest value for the $\bar{r}/\kappa_0$ ratio is chosen as 0.3 throughout the following analyses.

3.2. Design and Optimization for Isolation Bandwidth Maximization

In this section, optimization studies are performed in order to maximize the isolation bandwidth for the translational and torsional vibrations of the large-scale horizontal motion isolator to be produced. For this reason, it aimed to minimize the ω_{xy}/ω_u and ω_{zz}/ω_u ratios

under several design constraints. When the stepped beams of the system are modelled as shown in Figure 2.8(b), the design parameters to be optimized are as follows:

1- The length of the lower and upper parts of the beams: l_1
2- The radius of the lower and upper parts of the beams: r_1
3- The length of the middle part of the beams: l_3
4- The outer radius of the middle tier of the beams: $r_{3,o}$
5- The wall thickness of the middle part of the beams: t

On the other hand, there are several design constraints that need to be considered when the system is optimized. These constraints are summarized as follows:

1- The horizontal-motion isolator will be designed to carry a total mass of 60 kg. Approximately 30 kg of this total mass is determined as the mass of the top platform carrying the payload desired to be isolated. Therefore, considering the effect of gravity, the maximum load weight to which the isolator is subjected without the use of tension wire will be approximately 600 N. In this case, it is decided that the critical buckling force of the system is

$$P_{cr,1} \approx 600 \text{ N} \tag{3.1}$$

2- When the system undergoes a certain amount of lateral displacement while under the maximum tension force, the axial stress values in the beam cross-sections due to compression and bending of the beams must be lower than the yield stress of the beams. Since the fasteners are considerably stiffer than the thin beams and thin-walled cylinders, maximum axial stress calculations can be made only for the thin beams and thin-walled cylinders. Due to the symmetry of the stepped beams, the lower and upper thin beams can be considered to have the same deflection curves and thus the same maximum axial stress values. According to the beam sections

shown in Figure 2.8(b), the maximum axial stress values for the thin beams and thin-walled cylinder can be written as

$$\sigma_{1,max} \cong \frac{P_0+P+T_{max}}{3A_1} + \frac{M_{1,max}r_1}{I_1} < \frac{S_{y,1}}{SF} \tag{3.2}$$

$$\sigma_{3,max} \cong \frac{P_0+P+T_{max}}{3A_2} + \frac{M_{3,max}r_2}{I_2} < \frac{S_{y,3}}{SF} \tag{3.3}$$

respectively. In these equations, the first terms represent the axial compressive stresses, and the second terms represent the axial bending stresses. T_{max} is the maximum tension force required to buckle the system and is equal to the lower one between $T_{cr,xy}$ or $T_{cr,zz}$. $M_{i,max}$ is the maximum bending moment throughout the part i of the beams. SF is the safety factor and is taken as 1.5. $S_{y,i}$ is the yield strength of the same beam parts. $M_{i,max}$ values can be found analytically from the general solutions for lateral deflections of the beams when the system buckles. The unknown coefficients (A_i and B_i) in these general solutions for y_i (see Equation 2.22) can be determined by solving the system of the equations for the boundary and continuity conditions. In this way, if the maximum allowable lateral displacement of the top platform is denoted as δ_{max} when the system buckles, $M_{i,max}$ can be found as

$$M_{i,max} = E_i I_i \left|\frac{d^2y_i}{dx^2}\right| \tag{3.4}$$

where $\frac{d^2y_i}{dx^2} = -A_i(\delta_{max}){k_i}^2 \sin k_i x - B_i(\delta_{max}){k_i}^2 \cos k_i x$.

In the analyses, δ_{max} is taken as $0.05l$. For instance, if the length l of the beams is 200 mm, δ_{max} is 10 mm. In this way, it is aimed that the beams can withstand 10 mm of elastic lateral deformation at the maximum tension force. Similarly, the beam parts are also required to withstand the stress magnitudes at the maximum force. In order to have high strength in the thin sections, 302 stainless spring wire is used. Moreover, beryllium copper is used in the thin-walled cylindrical sections. Both materials have approximately 1 GPa of yield strength.

3- When the system is buckled by the maximum tension force, the maximum axial load (T_{max}) in the tension wire rope should be significantly lower than its breaking load. In all the experiments, the maximum load is excepted to be lower than 1000 N. Hence, a 1.8 mm diameter 7 x 7 304 stainless steel wire rope is chosen, which can support up to 1900 N tension force. Hence, the safety factor is at least

$$SF = \frac{1900}{1000} = 1.9 \qquad (3.5)$$

The cross-sectional area of a 7 x 7 wire rope is approximately 60.5 % of that of a wire with the same diameter. Since a 1.8 mm diameter wire has an area of 2.54 mm^2, the chosen wire rope has an area of 1.54 mm^2. Given that the wire rope can support up to 1900 N tension force, its yield strength is found as 1.23 GPa. Hence, when Equation 3.5 is used, the maximum allowable axial stress in the wire rope is found as 647 MPa.

4- The Euler-Bernoulli Beam Theory is used in the design of the beam parts. According to this theory, in order to obtain the critical buckling forces and natural frequencies accurately, the beams must be long enough (slender). As a result of the literature review, it is found that the ratio of the beam length to the shortest beam dimension should be at least 10 or more. From this point of view, the inequalities

$$20 \leq l_1/r_1 \tag{3.6}$$

$$20 \leq l_3/r_{3,o} \tag{3.7}$$

are used for the lower-upper and middle parts of the beam, respectively.

5- In section 2.1, it was stated that the length of the tension wire rope should be longer than the total length of the beams to decrease T_{max}. Since the beams are fixed by the sigma profiles as shown in Figure 3.1, the tension wire rope is longer than the beams. In addition to this, the length of the mandrels on the sigma profiles also increases this difference. Thus, the relationship between l_s and l can be written as

$$l_s = l + l_0 \tag{3.8}$$

where l_0 is taken as the difference between the length of the tension wire rope and the length of the beam. In this study, l_0 is obtained as 90 mm.

6- When industrial-type isolators are examined, it is found that the total heights of most of these systems are less than 800 mm [8,52,55,56,57]. For this reason, the total height of the designed isolator is determined to be around 400 mm, taking into account the length of the stepped beams and the heights of the base and top platforms. Hence, the length of the stepped beams is selected as $l = 200$ mm, and it is found from Remark 5 that l_s = 290 mm. In addition, the maximum allowable lateral deflection of the top platform is determined as $\delta_{max} = 0.05l = 10$ mm.

7- In order to firmly connect the thin beams to the thin-walled cylinders, the fasteners must be of a certain length. However, when the total length of the fasteners increases, the effective radius of gyration of the beams decreases, and the isolation bandwidth of the system decreases. For this reason, the length of the fasteners is taken as

$l_2 = 10$ mm in order to provide sufficient stiffness and to keep the radius of gyration of the beams as high as possible. As a result, since $2l_1 + 2l_2 + l_3 = l$ (see Figure 2.8(b)), it is obtained that $2l_1 + l_3 = 180$ mm.

8- The beams and thin-walled cylinders used in the industry are produced at certain radius and thickness values. For this reason, the variables r_1, $r_{3,o}$ and t are optimized, taking into account the available values for the beams and thin-walled cylinders as shown in Table 3.1.

Table 3.1. The limits on the thin beams and thin-walled cylinders

Thin Beam		**Thin-Walled Cylinders**		
Case	r_1 **(mm)**	**Case**	$r_{3,o}$ **(mm)**	t **(mm)**
1	0.65	**1**	2.60	0.20
2	0.75			
3	0.90	**2**	3.50	0.18
4	1.00			
5	1.30	**3**	4.50	1.00
6	1.50			

From the above values, it is seen that there are six different options for the thin beams and three different options for the thin-walled cylinders. Thus, there are 18 different options to select any combination of r_1 and $r_{3,o}$ values.

9- The top platform of the isolator is designed and manufactured to be used as a light-mass or heavy-mass structure depending on the payload carried. The light-mass system has the mass $m_0 = 17.75$ kg and the mass polar moment of inertia $J_0 = 1.088$ kg. m^2. On the other hand, the heavy-mass system has the properties $m_0 = 32.70$ kg and $J_0 = 2.791$ kg. m^2. When the system is required to carry the payloads over 30 kg, the light-mass top platform is preferred, while the heavy-mass

top platform is preferred to reduce the natural frequencies of the system when payloads below 30 kg are supported.

10- Due to the aluminum plates and surface coatings in industry, the length of each side of the top platform is determined as 600 mm. To increase the mass of the top platform, the brass strips are fixed on the lower sides of the aluminum plates. For this reason, the maximum distance to which the beams can be positioned from the central axis is determined as 260 mm.

Considering the limitations in Remarks 7 and 8, the initially given number of five independent variables (l_1, r_1, l_3, $r_{3,o}$ and t) decreases to three (l_1, r_1 and $r_{3,o}$). Since the parameters r_1 and $r_{3,o}$ must be selected from a set of discrete values according to Table 3.1, the genetic algorithm method is applied to find the optimum values for r_1, $r_{3,o}$ and l_1. The optimization studies must be performed for the worst-case scenario where the maximum tension force T_{max} takes the highest value to buckle the system. When this occurs, the axial-bending stress values in all stages of the beam cross-sections are maximized, and the isolation bandwidth of the system is minimized. When the top platform has a light mass, it is necessary to apply a higher T_{max} force to bring the system into quasi-zero-stiffness condition. In addition, while $T_{cr,xy}$ is not affected by the ratio $\bar{r}/\kappa_0$, $T_{cr,zz}$ increases when this ratio decreases as shown in Section 3.1. For this reason, the minimum $\bar{r}/\kappa_0$ value is chosen as 0.3. Hence, the optimization studies are performed when $\delta_{max} = 10$ mm, $m_0 = 17.75$ kg, $J_0 = 1.088$ kg. m^2, $\kappa_0 = 247.2$ mm, $m_p = J_p = 0$ and $\bar{r}/\kappa_0 = 0.3$. The genetic algorithm method is applied to minimize the ratio ω_{xy}/ω_u instead of the ratio ω_{zz}/ω_u because it is aimed to maximize the isolation bandwidth of the system along the two translational x and y axes instead of the single torsional z-axis. Moreover, ω_{zz} is constrained to be at 0.5 Hz. As a result, Table 3.2 shows the optimum design parameters (l_1, r_1 and $r_{3,o}$) and the results found by the genetic algorithm method.

Table 3.2. The optimum design parameters (l_1, r_1 and $r_{3,o}$) and the results found by the genetic algorithm method.

$\boldsymbol{l_1}$ **(mm)**	53
$\boldsymbol{r_1}$ **(mm)**	1.50
$\boldsymbol{r_{3,o}}$ **(mm)**	3.50
$\boldsymbol{m_{max}}$ **(kg)**	43.63
$\boldsymbol{T_{max}}$ **(N)**	818.9
$\boldsymbol{\sigma_{1,max}}$ **(MPa)**	405.8
$\boldsymbol{\sigma_{3,max}}$ **(MPa)**	172.4
$\boldsymbol{\sigma_{s,max}}$ **(MPa)**	544.3
$\boldsymbol{T_o}$ **(N)**	492
$\boldsymbol{\omega_{xy}}$ **(Hz)**	1.371
$\boldsymbol{\omega_{zz}}$ **(Hz)**	0.4996
$\boldsymbol{\omega_u}$ **(Hz)**	353.4
$\boldsymbol{\omega_{xy}/\omega_u}$	0.0039
$\boldsymbol{\omega_{zz}/\omega_u}$	0.0014

Table 3.2 shows that the $\sigma_{1,max}$, $\sigma_{3,max}$ and $\sigma_{s,max}$ values are below the specified axial stress limits for the stepped beam sections and tension wire rope. While the $\sigma_{1,max}$ value is obtained at the lower and upper ends of the thin beams, the $\sigma_{3,max}$ value is obtained at the regions exactly above the ends of the fasteners inside the thin-walled cylinders. Since the fasteners are passed into the cylinders by a certain amount, the cylinder areas surrounding the fasteners are subjected to very low stress values. Furthermore, the $\sigma_{s,max}$ value corresponds to the stress in the wire rope. More importantly, Table 3.2 shows that when ω_{zz} is constrained to be around 0.5 Hz, the system has the largest isolation bandwidth for translational vibrations because the ratio ω_{xy}/ω_u is minimized. Besides, the system has a larger isolation bandwidth for torsional vibrations because the ratio ω_{zz}/ω_u is smaller.

3.3. Finite Element Models

In this section, the final element models (FEM) are constructed on ABAQUS in order to perform buckling, stress and vibration analyses of the large-scale horizontal-motion isolator designed with the optimized parameters found in the previous section. In this way, the finite element (FE) results are used to verify the analytical results. Figure 3.7 shows the finite element model of the system consisting of three elastic stepped beams, a tension wire in the center and a rigid top platform with a point mass/inertia property shown with a green square in the figure. The inertial constants of the top platform are defined in this point mass/inertia property as $m_p = 17.75$ kg and $J_p = 1.088\ \text{kg.m}^2$. The parts of the stepped beams (thin beams, thin-walled cylinder and fasteners) are modelled with the continuum element type C3D20R, and the tension wire is modelled with the beam element type B31. On the other hand, the top platform is modelled with the rigid quadrilateral element type R3D4. In order to keep ω_{xy} and ω_{zz} close to each other at low tension forces, the stepped beams are placed at the distance $\bar{r} = 240$ mm from the central axis which is close to the radius of gyration of the top platform ($\kappa_0 = \sqrt{J_0/m_0} = 244.9$ mm).

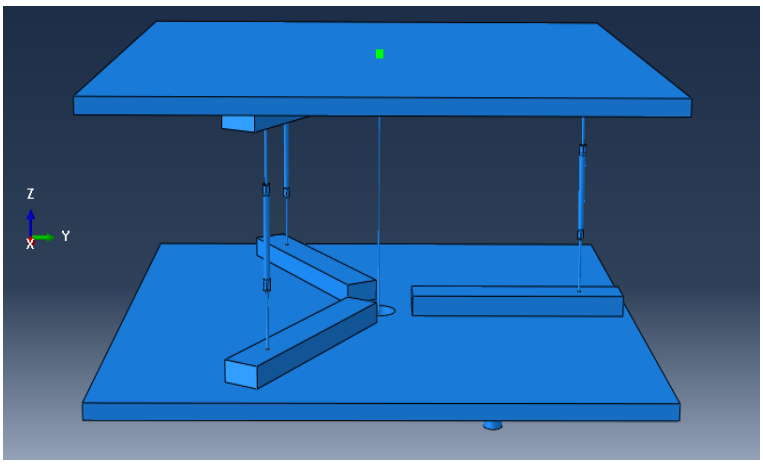

Figure 3.7. Finite element model of the large-scale isolator

3.3.1. Buckling of the Large-Scale Isolator

Figure 3.8 shows the buckling of the large-scale isolator when the system is under the action of a vertical force P. In this case, gravity is not taken into account, and the wire is not tensioned. As shown previously, the critical value of the force P is equal to $P_{cr,1}$.

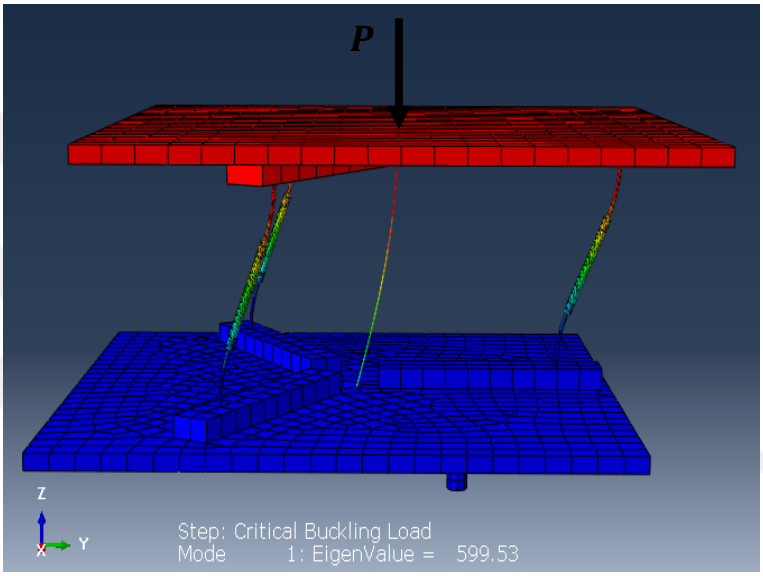

Figure 3.8. Buckling of the system when $P_{cr,1} = 599.5$ N.

When $P_{cr,1}$ is known, m_{max} can be found from Equation 2.20. Table 3.3 shows the comparison of the analytical and numerical results for $P_{cr,1}$ and m_{max}. It is seen from the below table that the finite element results verify the analytical results.

Table 3.3. The comparison of the analytical and finite element results for $P_{cr,1}$ and m_{max}.

	Analytical	**Finite Element**
$\boldsymbol{P_{cr,1}}$ **(N)**	601.3	599.5
$\boldsymbol{m_{max}}$ **(kg)**	43.54	43.36

When gravity is taken into account and the wire is stretched with a tension force T, Figure 3.9 shows the lateral buckling of the system at $T = T_{cr,xy}$.

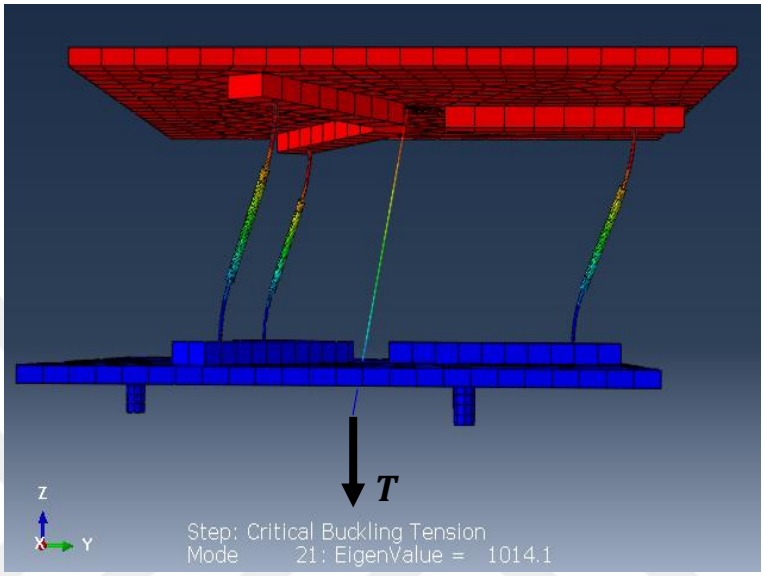

Figure 3.9. Lateral buckling of the system at $T = T_{cr,xy}$.

Similarly, Figure 3.10 shows the torsional buckling of the system at $T = T_{cr,zz}$.

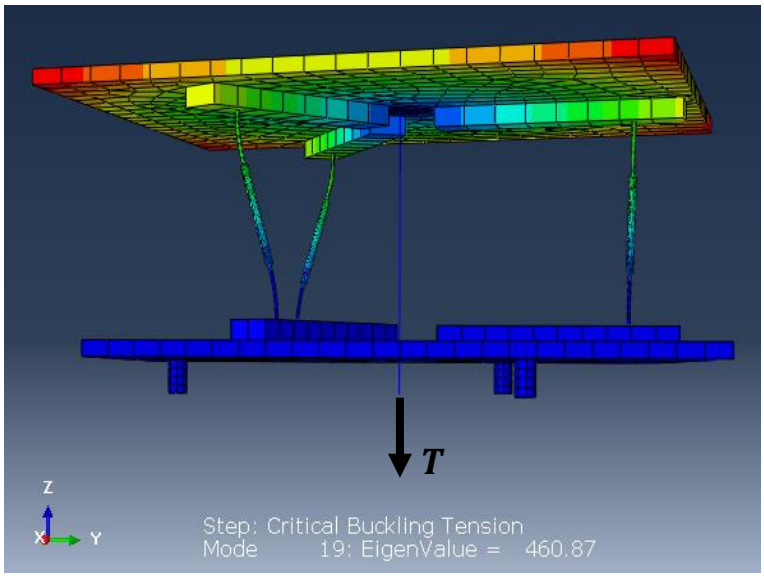

Figure 3.10. Torsional buckling of the system at $T = T_{cr,zz}$.

From Figure 3.9 and Figure 3.10, it is seen that $T_{cr,zz} < T_{cr,xy}$. For this reason, the system undergoes torsional buckling. At a higher critical value of the tension force T, Figure 3.11 shows the buckling of the system at $T = T_{cr,u}$.

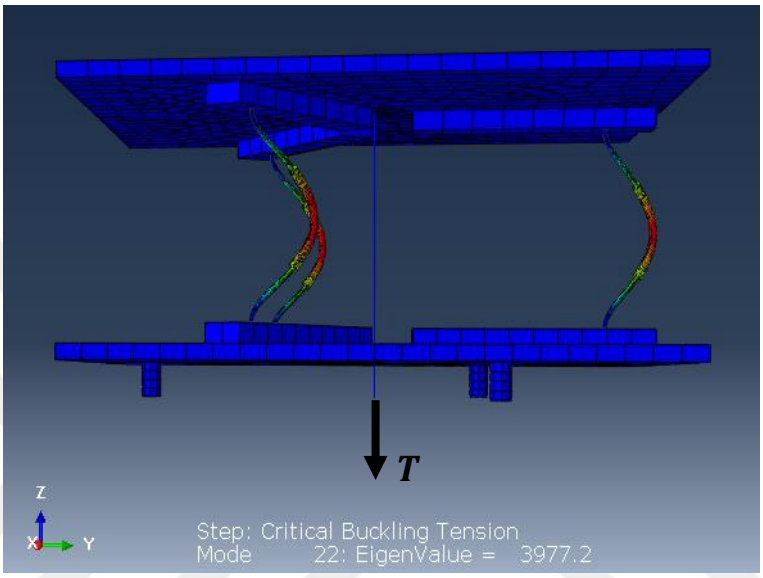

Figure 3.11. Buckling of the system at a higher critical value of the tension force T where $T = T_{cr,u}$.

Finally, the comparison of the analytical and finite element results for $T_{cr,xy}$, $T_{cr,zz}$ and $T_{cr,u}$ is shown in Table 3.4.

Table 3.4. The comparison of the analytical and finite element results for $T_{cr,xy}$, $T_{cr,zz}$ and $T_{cr,u}$.

	Analytical	**Finite Element**
$\boldsymbol{T_{cr,xy}}$ **(N)**	1013	1014
$\boldsymbol{T_{cr,zz}}$ **(N)**	464.7	460.9
$\boldsymbol{T_{cr,u}}$ **(N)**	4017	3977

3.3.2. Elastic Deflection of the Large-Scale Isolator

When the system is buckled and tilts laterally, the axial stress magnitudes in the beams may be considerably high due to large deflections. Besides, the tension wire may be under the action of excessive axial stress. Under this condition, it is important to ensure that the beams and wire can deform elastically given the maximum tension force T_{max} and maximum allowable lateral deflection δ_{max} of the top platform. In these analyses, T_{max} can be taken as approximately equal to the lowest critical buckling tension force of the system which is $T_{cr,zz}$ in this case. The stress analysis can be divided into three sub-steps. In the first step, gravity is applied to pre-stress the beams. In the second step, T_{max} is applied to the wire to bring the system into a quasi-zero-stiffness condition. Finally, in the third step, the top platform is forced to displace laterally by δ_{max}. Since FE simulations give that $T_{cr,zz} = 460.9$ N, T_{max} can be taken as $T_{max} = 460$ N in both the analytical and FE models. When $\delta_{max} = 10$ mm, Figure 3.12 shows that the maximum axial stress values occur at the lower boundary region of the thin beam. It can be seen from Figure 3.12 that maximum stress values occur at the compression side of the lower end of the thin beam, taking values between 388.9 MPa and 458.0 MPa.

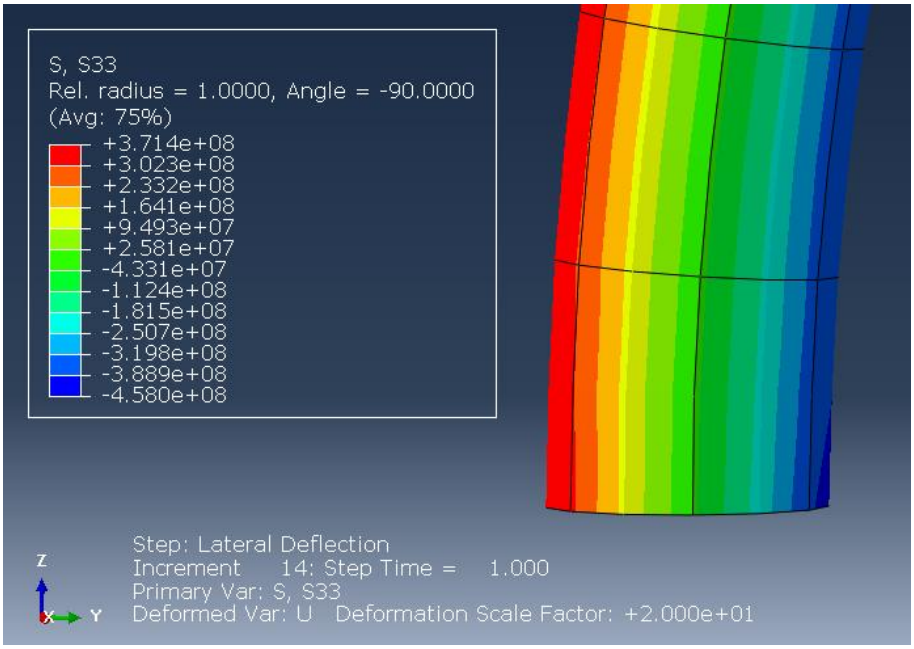

Figure 3.12. Maximum axial stress distribution in the thin beam.

On the other hand, Figure 3.13 shows that maximum axial stress values occur at regions close to the ends of the thin-walled cylinder. Since the fasteners are passed into the thin-walled cylinders by a certain amount, the regions of the cylinders surrounding the fasteners are subjected to very low stress values. Hence, maximum axial stress values occur at regions exactly where the fasteners end inside the cylinder. in the compressed regions of the thin-walled cylinder slightly above (below) the fasteners in it, taking values between 120 MPa and 140 MPa.

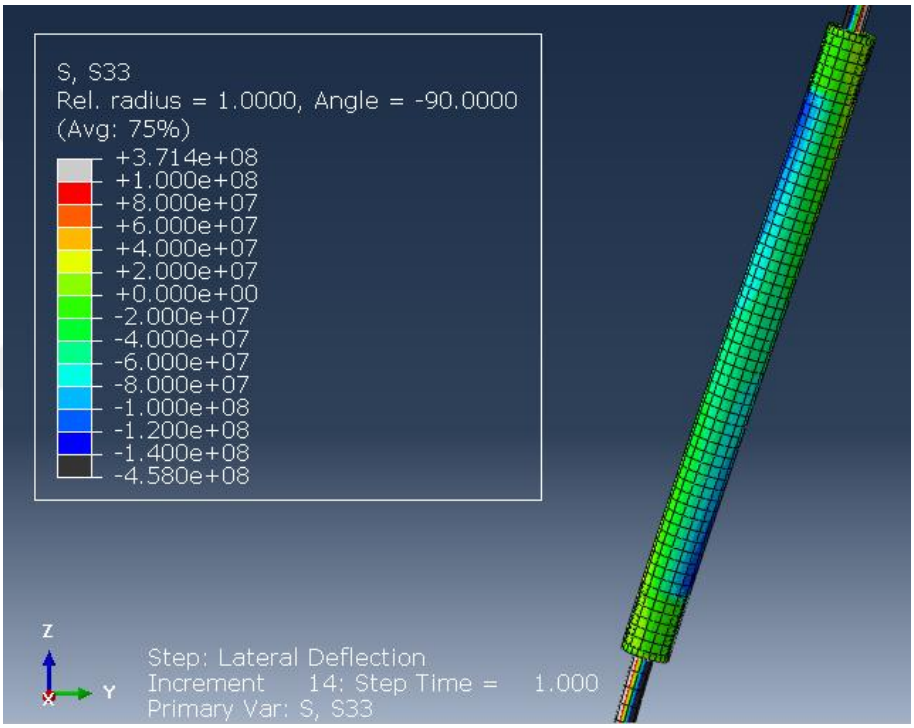

Figure 3.13. Maximum axial stress distribution in the thin-walled cylinder.

Table 3.5 shows the comparison of the analytical and finite element results for the maximum axial stress values in the thin beams, thin-walled cylinders and the wire.

Table 3.5. The comparison of the analytical and finite element results for the maximum axial stress values in the thin beams ($\sigma_{1,max}$), thin-walled cylinders ($\sigma_{3,max}$) and wire ($\sigma_{s,max}$).

	Analytical	**Finite Element**
$\boldsymbol{\sigma_{1,max}}$ **(MPa)**	404	458
$\boldsymbol{\sigma_{3,max}}$ **(MPa)**	134	135
$\boldsymbol{\sigma_{s,max}}$ **(MPa)**	299	298

Table 3.5 shows that analytical and finite element results are compatible with each other. As a result, when the system is built with these optimized design parameters found in the previous section, it is seen that the maximum axial stress values to which the system will be subjected are lower than the experimental yield strengths of these elements (approximately 1 GPa).

3.3.3. Vibration of the Large-Scale Isolator

When the same design parameters are used, Table 3.6 shows the analytical and finite element results for ω_{xy}, ω_{zz} and ω_u at various T values. From this table, it can be seen that the analytical results are validated by the finite element results. As the tension force T increases, ω_{zz} decreases at a faster rate than ω_{xy}. When $T = 430$ N, the analytical and finite element results show that ω_{zz} becomes nearly equal to 0.5 Hz.

Table 3.6. The analytical (Analyt.) and finite element (FE) results for ω_{xy}, ω_{zz} and ω_u at certain T values.

T (N)	ω_{xy} (Hz)		ω_{zz} (Hz)		ω_u (Hz)	
	Analyt.	**FE**	**Analyt.**	**FE**	**Analyt.**	**FE**
0	1.892	1.889	1.913	1.907	375.7	373.2
100	1.799	1.803	1.696	1.689	371.1	368.7
200	1.700	1.706	1.446	1.437	366.5	364.0
300	1.595	1.601	1.141	1.130	361.8	359.4
400	1.482	1.488	0.7159	0.6966	357.0	354.6
430	1.446	1.452	0.5244	0.4973	355.6	353.2
450	1.421	1.427	0.3414	0.2975	354.6	352.2

When $T = 430$ N, Figure 3.14 and Figure 3.15 show the lateral and torsional vibrational modes of the system at $\omega_{xy} = 1.452$ Hz and $\omega_{zz} = 0.4973$ Hz, respectively.

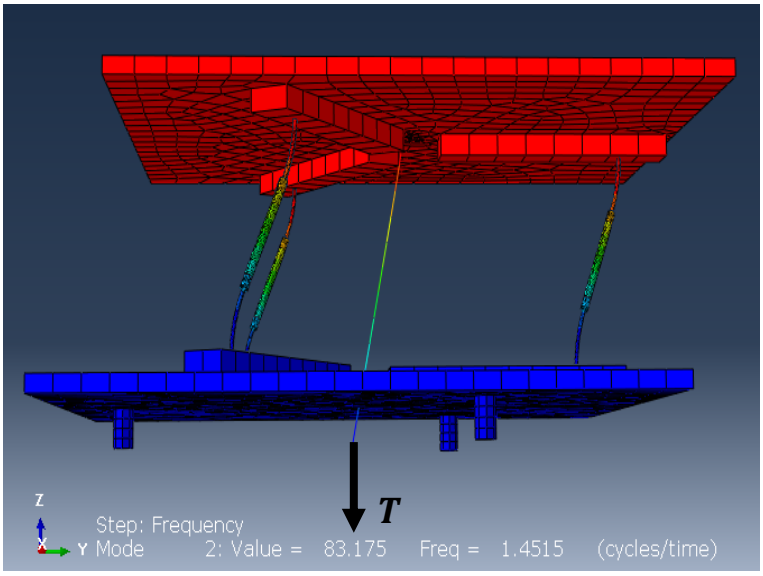

Figure 3.14. When $T = 430$ N, lateral vibrational mode of the system at $\omega_{xy} = 1.452$ Hz.

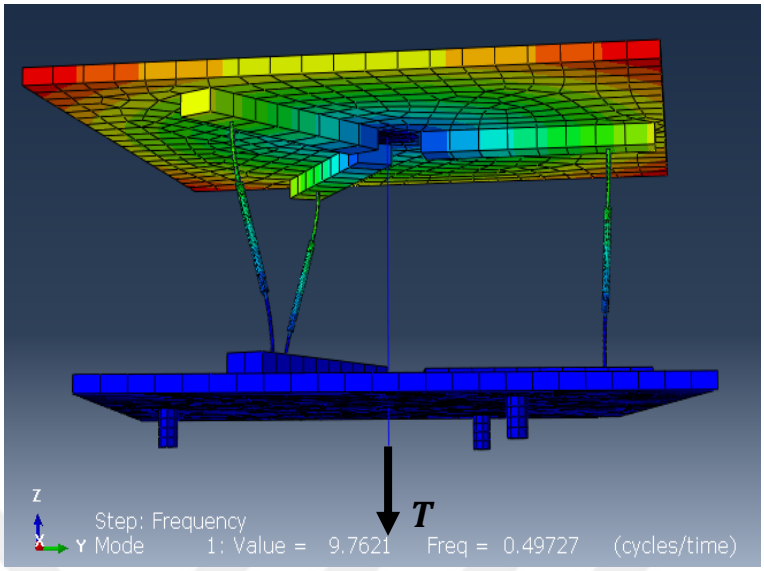

Figure 3.15. When $T = 430$ N, torsional vibrational mode of the system at $\omega_{zz} = 0.4973$ Hz.

Under the same condition, Figure 3.16 shows the higher vibrational mode of the system at $\omega_u = 353.2$ Hz.

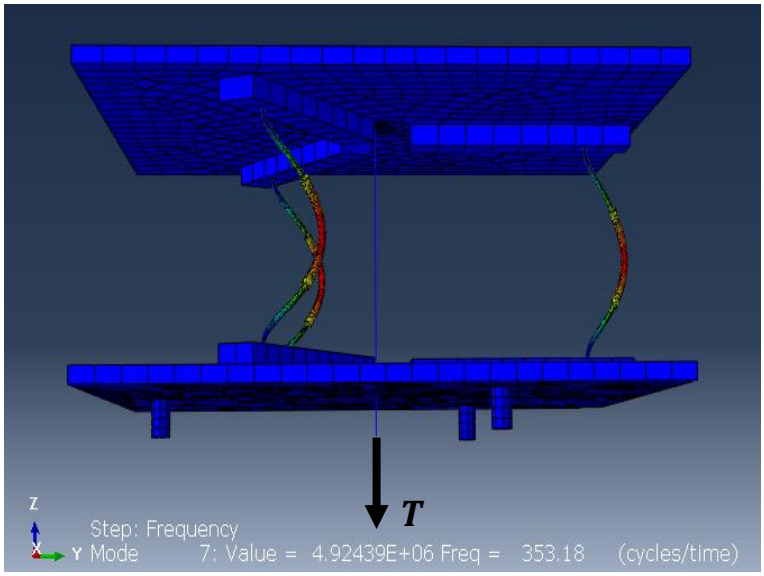

Figure 3.16. When $T = 430$ N, higher vibrational mode of the system at $\omega_u = 353.2$ Hz.

The frequency spectrum of the system can be analyzed for translational and torsional vibrations separately. Figure 3.17 shows that a harmonic driving force $F(t)$, which is in the form of a complex exponential $F(t) = F_0 e^{j\omega t}$, is applied to the middle of the left side of the top platform in the y direction to create translational vibrations. Thus, the response of the top platform can be assumed to be in the form $y(l,t) = Ye^{j\omega t}$ where Y is the maximum amplitude of the lateral displacement of the response and l is the length of the stepped beams.

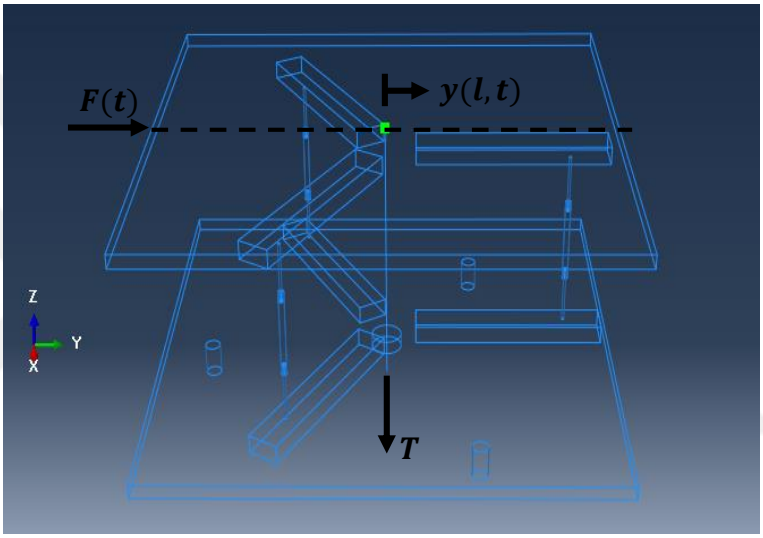

Figure 3.17. A harmonic driving force $F(t)$ can be applied to the top platform parallel to the horizontal y-axis (or x-axis).

When $T = 430$ N, $F_0 = 10$ N and $0.1 \leq \omega \leq 400$ Hz, Figure 3.18 shows the changes in Y relative to ω obtained from the analytical and FE models. The results are plotted in the logarithmic scale. From this figure, it can be seen that the analytical frequency spectrum precisely agrees with the finite element spectrum, and the first resonance peaks occur around 1.45 Hz in both models as expected from Table 3.6. Moreover, both models show that the second resonance peaks occur slightly above 350 Hz. To bound the resonance peaks in the finite element models, the structural damping of the system is assumed as 0.001 in ABAQUS.

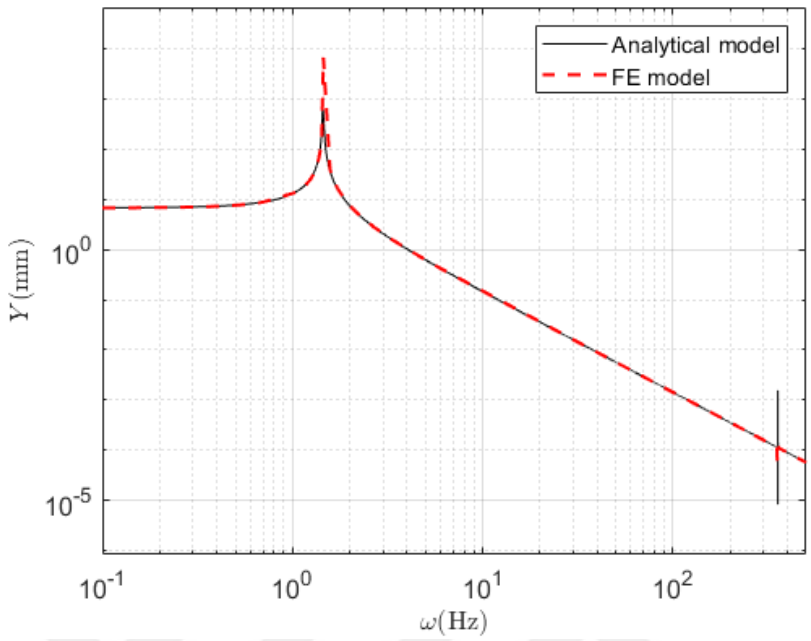

Figure 3.18. The changes in Y (mm) with respect to ω (Hz) obtained from the analytical and FE models.

On the other hand, Figure 3.19 shows that harmonic driving forces $F(t)$ ($F(t) = F_0 e^{j\omega t}$) are applied to the opposite corners of the top platform with the side length $a = 600$ mm to create a harmonic driving moment $M(t) = F(t)a$. Thus, the response of the top platform can be assumed to be in the form $\theta(l,t) = \Theta e^{j\omega t}$ where Θ is the maximum amplitude of the angular displacement of the response and l is the length of the stepped beams. When $T = 430$ N, $F_0 = 0.5$ N and $0.1 \leq \omega \leq 400$ Hz, Figure 3.20 shows the changes in Θ relative to ω obtained from the analytical and FE models. The results are plotted in the logarithmic scale. From Figure 3.20, it can be seen that the analytical frequency spectrum precisely agrees with the finite element spectrum, and the first resonance peaks occur around 0.5 Hz in both models as expected from Table 3.6. Moreover, both models show that the second resonance peaks occur slightly above 350 Hz.

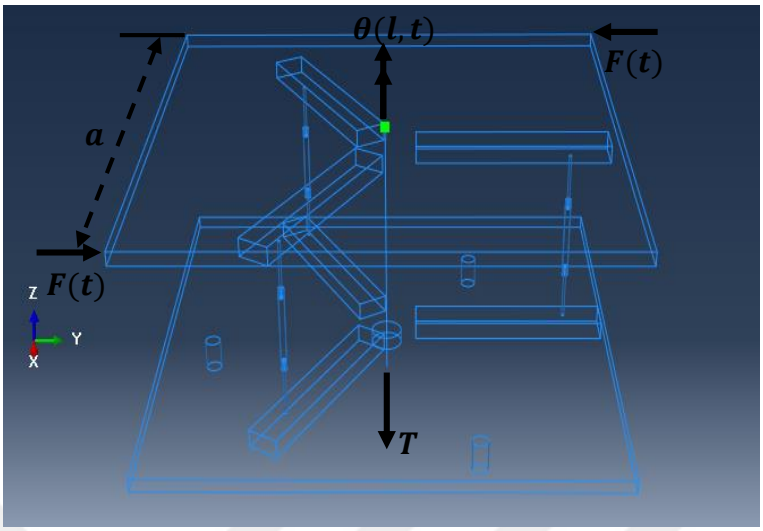

Figure 3.19. A harmonic driving moment $M(t) = F(t)a$ can be applied to the top platform about the central axis of the system parallel to the vertical z-axis.

As in the case of translational vibrations, the structural damping is assumed to be 0.001.

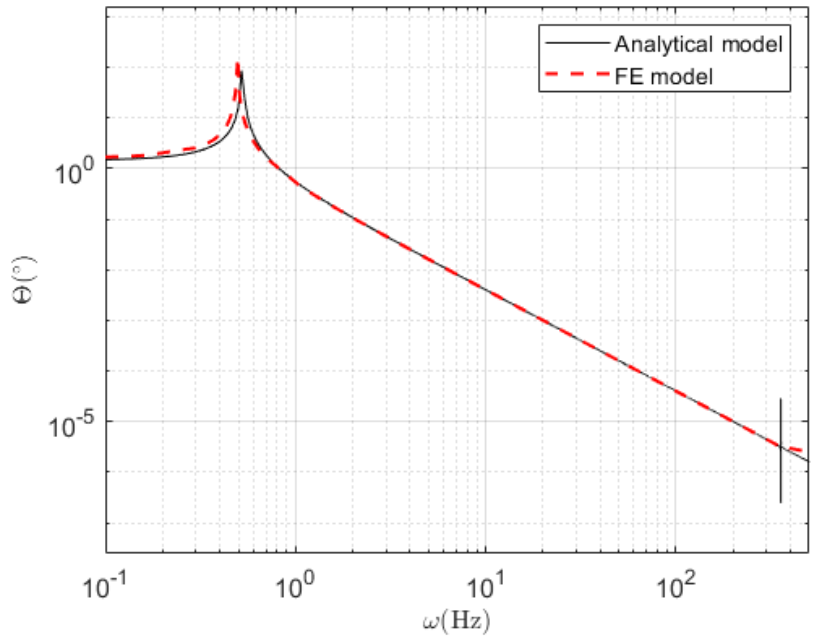

Figure 3.20. The changes in Θ (°) with respect to ω (Hz) obtained from the analytical and FE models.

3.4. Experimental Validation

Figure 3.21 shows views of the industrial-type vibration isolator (Minus K 100BM-1) and the height-adjustable support structure placed under it. Purchased to be used as a benchmark system, this isolator has horizontal and vertical sub-systems that can operate at low frequencies.

Figure 3.21. Views of an industrial-type vibration isolator (Minus K 100BM-1) and the height-adjustable support structure placed underneath.

In order for the isolator shown in Figure 3.21 to operate at low frequencies, the mass and mass polar moment of inertia of the system are increased by placing aluminum plates and surface coatings on the top platform. In addition, 1 mm thick rubber sheets with high damping coefficient are placed between the aluminum plates and surface coatings in order to prevent undesired vibration modes arising from these parts. These added weights reduces

the natural frequencies of the system in the horizontal and vertical directions. Moreover, in order to assess the vibration isolation performance of the system in a wide frequency range, the support structure must have high structural stiffness. This structure is built with three legs to prevent the system from shaking on the ground, and the sigma profile parts used in the system are connected to each other with steel wire ropes to increase structural stiffness, especially in torsional and lateral directions. In addition, this support structure is produced to have an adjustable height in order to bring the isolator to the desired heights.

Since horizontal stiffness adjustment mechanisms are designed in this thesis, impact tests are applied on the industrial-type isolator to evaluate the isolation performance of its horizontal sub-system. Figure 3.22 shows the experimental setup of this isolator. In this setup, Polytec data acquisition device, 393B04 Model PCB accelerometer and laptop computer are used. The measurement time was 8 seconds, and the acceleration data was collected with a resolution of 0.125 Hz up to 100 Hz without using a filter. In addition, the sampling frequency was 240 Hz.

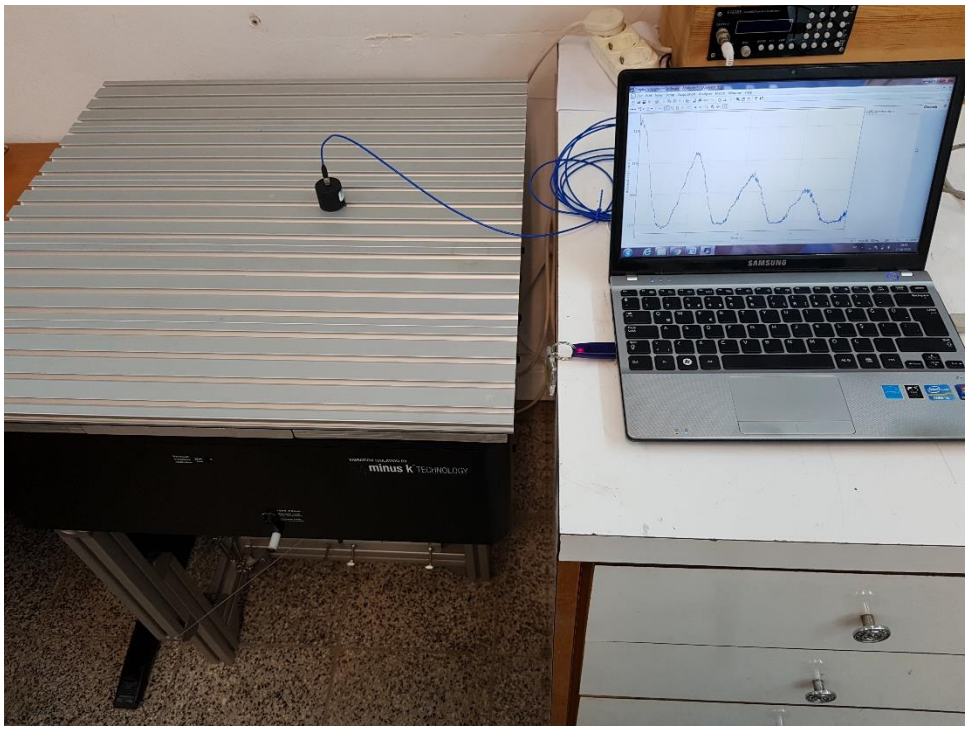

Figure 3.22. Test setup of the Industrial-Type Isolator (Minus K 100BM-1).

Since the horizontal sub-system of this isolator does not have adjustable stiffness, the vibration isolation performance of the system deteriorates as the payload mass decreases. The isolator's own plate (top platform) has the dimensions 610 mm x 572 mm x 10 mm and is made of aluminum (density 2700 kg/m^3). Therefore, its mass is estimated as 9.42 kg. To improve the horizontal vibration isolation performance, the aluminum plates (extra mass 28.70 kg) are used on the top platform.

When the mass of the system is increased, the free translational and torsional vibration response of it can be examined in time and frequency domains. Figure 3.23 shows the acceleration values of the translational and torsional vibrations of the top platform over time. When the periods of these two movements are examined, it is seen that the period of the torsional vibrations is longer than that of the translational vibrations. In other words, it is understood that the torsional natural frequency is lower than the translational natural frequency.

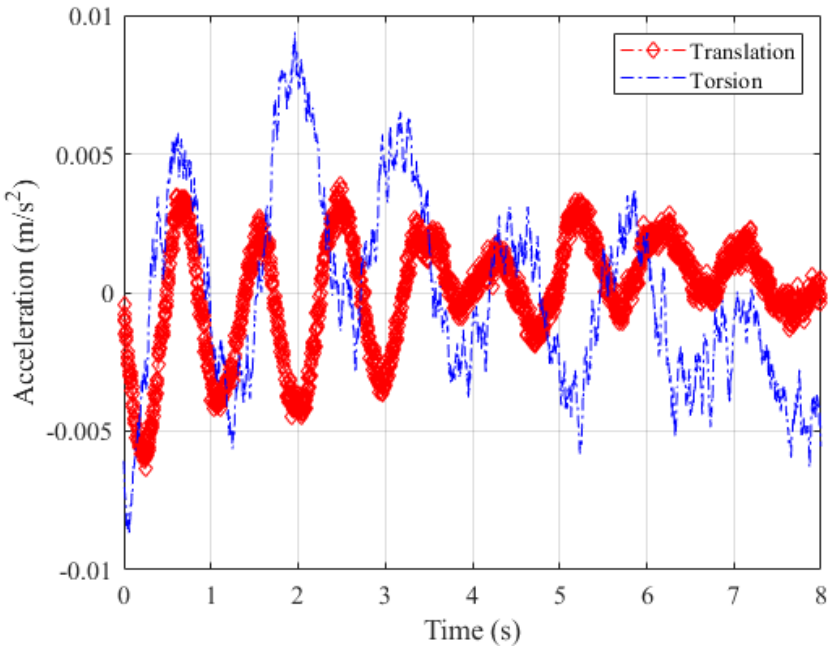

Figure 3.23. The acceleration values for the translational and torsional motions of the top platform over time for the Minus K 100BM-1 isolator with 28.7 kg extra mass.

Figure 3.24 shows the system response in the frequency domain. Since the resonance frequency of torsional vibrations is lower than that of translational vibrations, it is understood that the torsional natural frequency is lower than the translational natural frequency. The resonance frequencies are determined as 1.125 Hz and 0.750 Hz for translational and torsional vibrations, respectively. On the other hand, a distinct resonance up to 100 Hz is not observed for both vibration types.

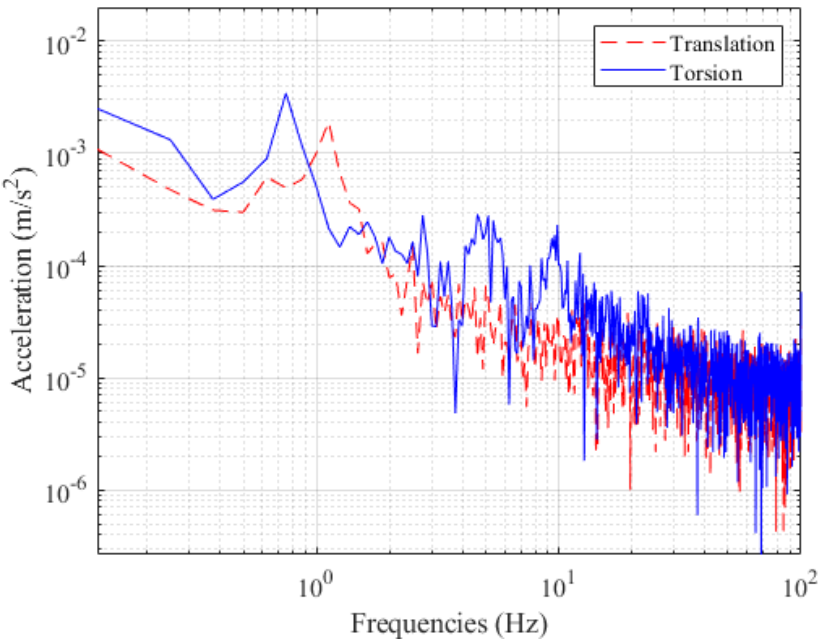

Figure 3.24. The acceleration values according to the frequency during the translational and torsional vibrations of the top platform for the Minus K 100BM-1 isolator with 28.7 kg extra mass.

In order to compare the experimental results performed on the industrial-type isolator, the large-scale isolator is constructed (see Figure 3.25). The sigma profiles fixed to the base and top platforms allow the stepped beams to move to or away from the central axis of the isolator to adjust the torsional stiffness and torsional natural frequency. The mandrels fixing the beams from their ends are fixed inside the rails of the sigma profiles by means of the t-slot nuts. Thus, the beams can be adjusted to any position depending on the payload carried.

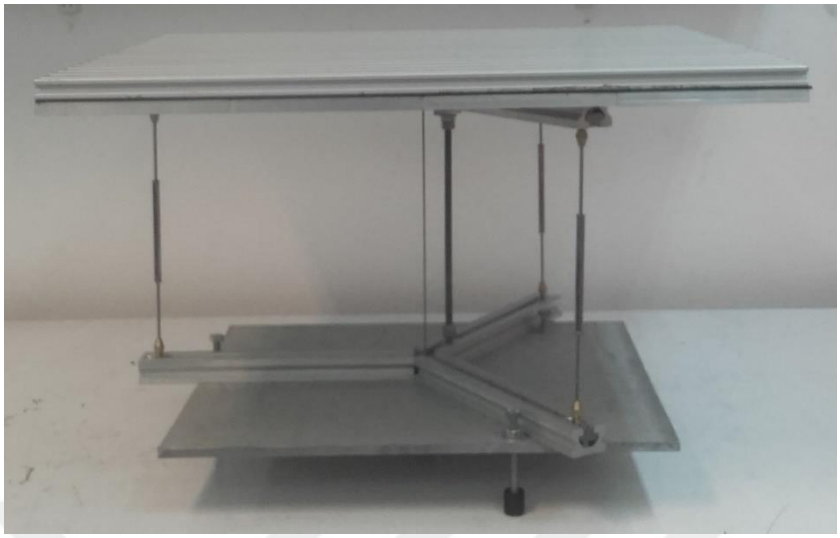

Figure 3.25. View of the Large-Scale Isolator.

The top platform of this isolator has the mass $m_0 = 17.75$ kg and the mass polar moment of inertia $J_0 = 1.088$ kg.m^2. The total length of the beams, measured from the outside of the mandrels, is $l = 200$ mm. In addition, the 7 x 7 steel tension wire rope has the length $l_s = 290$ mm, diameter $d_s = 1.8$ mm and mass per unit length $\rho_s A_s = 0.0127\ \text{kg.m}^2$. Moreover, the points where the beams are connected are 260 mm from the central axis of the isolator ($\bar{r} = 260$ mm). After the large-scale isolator was constructed according to the optimization studies, it was realized that the elastic stepped beams had different values for material properties (E and ρ) than the numerical values shown in Table 2.5.Hence, Table 3.7 shows the experimental values of the design parameters of the stepped beams.

Table 3.7. The experimental values of the design parameters of the stepped beams.

	Thin Part	**Fastener Part**	**Thick Part**
$\boldsymbol{E}$ **(GPa)**	193	200	125
$\boldsymbol{\rho}$ **(kg/m^3)**	7920	7800	8350
$\boldsymbol{l}$ **(mm)**	53	10	92
$\boldsymbol{r_o}$ **(mm)**	1.50	3.32	3.50
$\boldsymbol{r_i}$ **(mm)**	-	1.50	3.32

The thin and thick parts of the beams are connected to each other by using the fasteners as described in Section 2.1. In this case, the analytical critical buckling force of the system is found to be $P_{cr,1} = 647.3$ N. The experimental studies are conducted on the isolator under two different conditions. In the first condition, the system has a light mass as shown in Figure 3.25. In the second condition, the mass and mass polar moment of inertia of the system are increased by attaching brass strips on the four edges of the top platform ($m_0 = 32.30$ kg and $J_0 = 2.791$ kg.m^2). Figure 3.26 shows the view of the system when the top platform has the extra brass mass.

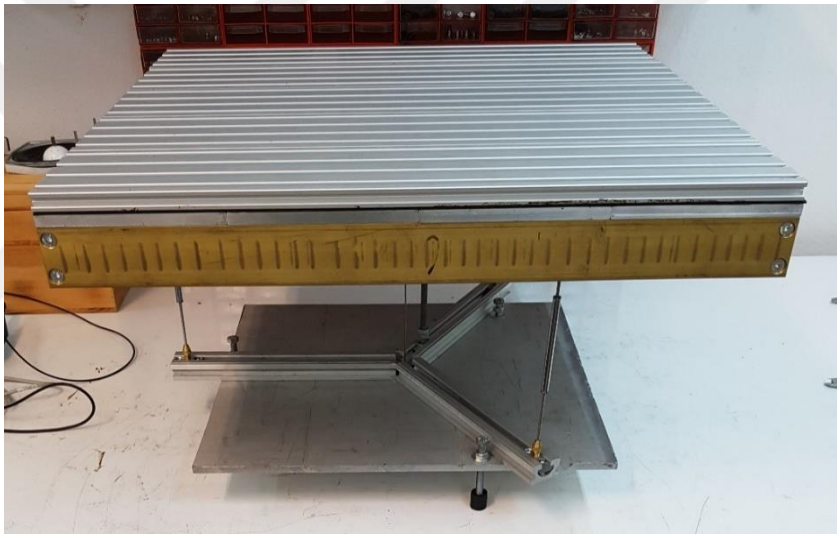

Figure 3.26. View of the large-scale isolator when brass strips are attached to the top platform to increase its mass and polar moment of inertia.

Table 3.8 shows the analytical results for the maximum payload mass that the isolator can support (m_{max}), the critical buckling tensions ($T_{cr,xy}$, $T_{cr,zz}$ and $T_{cr,u}$), the optimum tension force required to bring the lowest natural frequency to the order of 0.5 Hz (T_o) and the horizontal natural frequencies (ω_{xy}, ω_{zz} and ω_u) at $T = T_o$ for the light and heavy mass cases.

Table 3.8. The Analytical Results for m_{max}, $T_{cr,xy}$, $T_{cr,zz}$, $T_{cr,u}$, T_o, ω_{xy}, ω_{zz} and ω_u for the Light and Heavy Mass Cases.

	Light-Mass System	**Heavy-Mass System**
$\boldsymbol{m_0}$ **(kg)**	17.75	32.30
$\boldsymbol{m_{max}}$ **(kg)**	48.23	33.68
$\boldsymbol{T_{cr,xy}}$ **(N)**	1123	787.4
$\boldsymbol{T_{cr,zz}}$ **(N)**	508.2	365.4
$\boldsymbol{T_{cr,u}}$ **(N)**	4585	4427
$\boldsymbol{T_o}$ **(N)**	482	297
$\boldsymbol{\omega_{xy}}$ **(Hz)**	1.515	0.9784
$\boldsymbol{\omega_{zz}}$ **(Hz)**	0.4930	0.4978
$\boldsymbol{\omega_u}$ **(Hz)**	378.4	380.2

Based on the above results, it is seen that the isolator will undergo torsional buckling in both cases when the experimental studies are carried out. To prevent the collapse of the system due to buckling, a motion-limiting structure is used as shown in Figure 3.27. This structure allows at most 1 mm vertical deflection and 5 mm horizontal deflection. Hence, the vibration isolator's top platform can only displace with small amplitudes with respect to the equilibrium position. This restraint system also prevents the beams from being subjected to high stress values by restricting large lateral deflections.

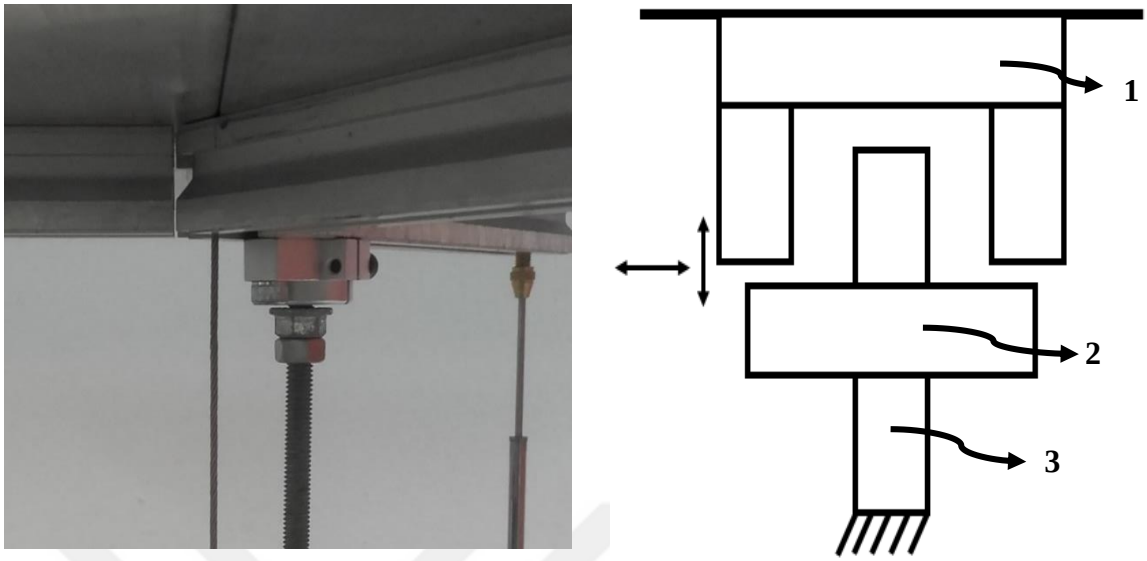

(a) (b)

Figure 3.27. (a) View of the motion restraint system. if the restraint hole moves more than 5 mm laterally, the stud touches the edges of the hole. Besides, when the tension wire is tightened more than necessary, the nut fixed with the counter on the stud touches edge of the hole and limits the axial movement. Apart from these situations, the system can vibrate without any contact with the restraint system, (b) The schematic structure of the motion restraint system: 1 – Hollow Cylindrical Part, 2 – Nut, 3 – Stud. While the stud prevents the top platform from moving horizontally more than the maximum allowable deflection during the lateral buckling of the system, the nut prevents the system from collapsing downwards during the torsional buckling of the system.

Impact tests are applied to the isolator to find its translational and torsional natural frequencies when it has the light-mass and heavy-mass top platforms. The experimental setup for the light-mass system is shown in Figure 3.28, and the experimental setup for the heavy-mass system is also the same. By attaching the accelerometer to the top platform, the frequency spectrums of both systems can be obtained.

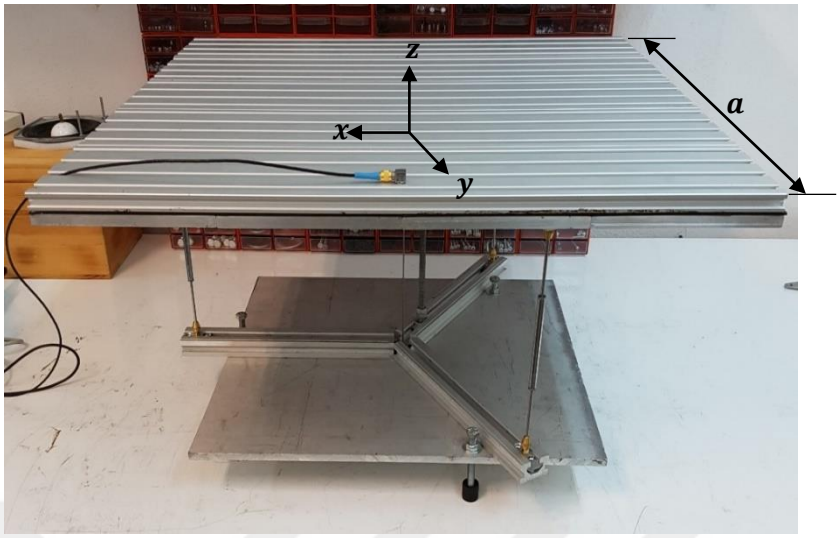

Figure 3.28. View of the experimental setup for the light mass case.

The acceleration data for translational vibrations of the light-mass and heavy-mass systems can be obtained by applying an impulse force to the middle point of the side a (see Figure 3.28). As a result, Figure 3.29 shows the frequency spectrum of both systems while there is no tension force in the wire rope.

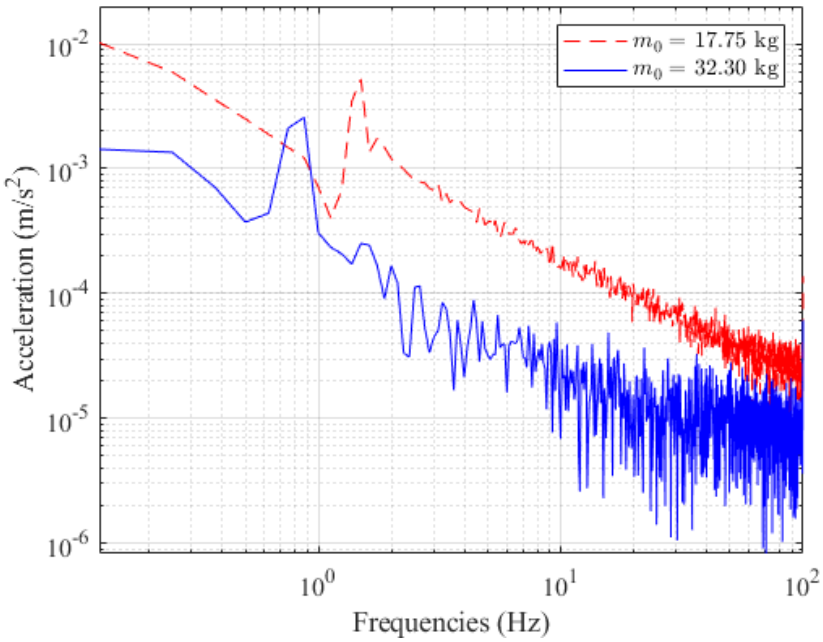

Figure 3.29. Acceleration data for the translational vibrations of the large-scale isolator with the light and heavy mass systems when there is no tension force in the wire rope.

From Figure 3.29, it is seen that the translational natural frequencies of the light and heavy mass systems (ω_{xy}) are 1.50 Hz and 0.875 Hz, respectively. Considering that the lowest natural frequency of the isolator is desired to be reduced to the order of 0.5 Hz, it is seen that the heavy mass system is expected to achieve this goal with lower tension forces. Besides, it is seen from the figure above that the upper natural frequencies (ω_u) of both systems are higher than the targeted 100 Hz value. Based on all these findings, it can be stated that the systems perform vibration isolation at low frequencies and have wide frequency ranges in the axes where they make translational vibrations.

When there is no tension force in the wire rope and an impulse force is applied to any corner point of the side a as shown in Figure 3.28, the acceleration data for torsional vibrations of both systems are shown in Figure 3.30.

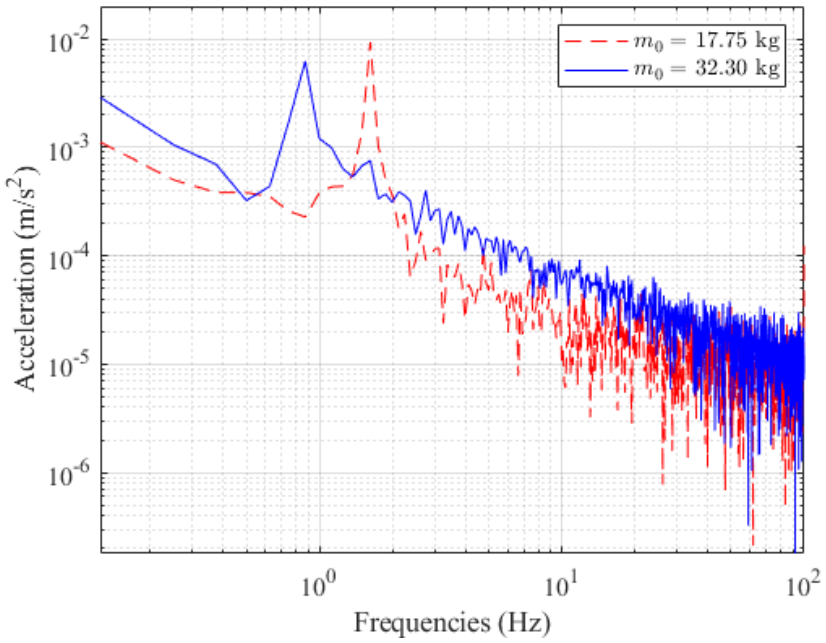

Figure 3.30. Acceleration data for the torsional vibrations of the large-scale isolator with the light and heavy mass systems when there is no tension force in the wire rope.

According to Figure 3.30, the torsional natural frequencies (ω_{zz}) for both cases correspond to 1.625 Hz and 0.875 Hz, respectively. Besides, it is seen that the upper natural frequencies of both systems are higher than the targeted 100 Hz value. Based on all these findings, it can be stated that the systems perform vibration isolation at low frequencies and have wide isolation frequency ranges for torsional vibrations.

When the industrial-type isolator is compared with the large-scale isolator with the light-mass and heavy-mass top platforms in terms of their translational and torsional frequency spectrum, four different cases can be examined. In each of these cases, the frequency spectrums of the light-mass and heavy-mass systems are obtained from the impact tests when there is a tension force in the wire which is found from the wire natural frequency $f_{s,1}$ as shown in Equation 2.72. The wire natural frequencies are measured as explained in Section 2.3. Figure 3.31 shows the experimental results of the translational frequency spectrums of the industrial-type isolator and the light mass system when the tension force is applied to the light-mass system ($f_{s,1} = 261$ Hz, $T = 291$ N).

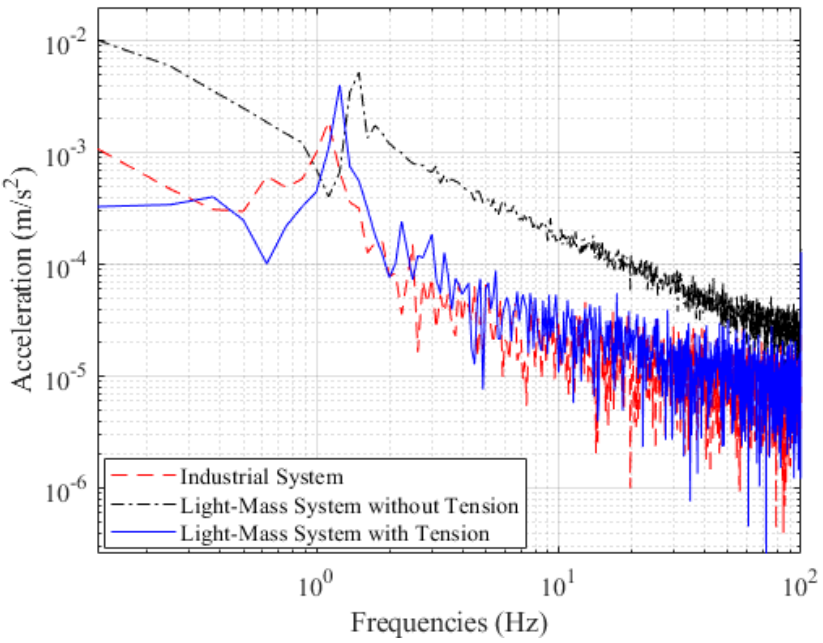

Figure 3.31. Experimental results of the translational frequency spectrums of the industrial-type isolator and the light-mass system when the tension force is applied to the light-mass system ($f_{s,1} = 261$ Hz, $T = 291$ N).

Similarly, Figure 3.32 shows the experimental results of the torsional frequency spectrums of the industrial-type isolator and the light-mass system when the same tension force is applied to the light-mass system.

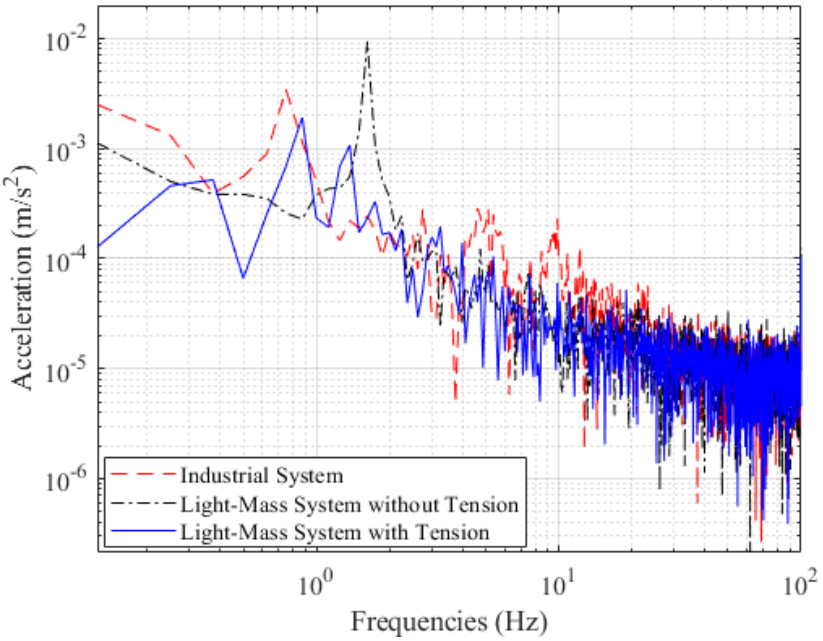

Figure 3.32. Experimental results of the torsional frequency spectrums of the industrial-type isolator and the light-mass system when the same tension force is applied to the light-mass system ($T = 291$ N).

Figure 3.31 and Figure 3.32 show that when the tension force is applied to the light-mass system, its translational and torsional natural frequencies decrease from 1.500 Hz to 0.875 Hz and from 1.625 Hz to 0.875 Hz, respectively. It is observed that when the tension force is found as 291 N, the torsional natural frequency of the system decreased more than the translational natural frequency and came to the same value with the translational natural frequency.

Compared to the experimental results, the analytical model shows that when the same tension force is applied ($T = 291$ N), $\omega_{xy} = 1.61$ Hz and $\omega_{zz} = 1.25$ Hz. Hence, the

experimental translational and torsional natural frequencies are found to be approximately 46 % and 30 % lower than their analytical counterparts, respectively. The main reason for these differences is considered to stem from the assumption that the base and top platforms are not deformed under tension forces. However, since they are relatively large and flat plates, the structural stiffness of the system is lower than expected in the analytical models. As a result, the experimental natural frequencies are found to be lower than the analytical values. If the tension force is increased slightly, the system is observed to buckle in the torsional mode as expected from the analytical results ($T_{cr,xy} = 1123$ N, $T_{cr,zz} = 508.2$ N).

Under this condition, since the system slightly collapses downwards, the tension force in the wire rope decreases, reducing the experimental natural frequency of the wire rope. Besides, Figure 3.31 shows that the translational natural frequency of the light-mass system becomes lower than that of the industrial system when the tension force is applied. This implies that the light-mass system achieves better isolation performance at low frequencies than the industrial system. On the other hand, although the torsional natural frequency of the light-mass system is higher than that of the industrial system when the tension force is applied, Figure 3.32 shows that the tension mechanism also reduces the torsional natural frequency of the light-mass.

If more tension force were applied, the light-mass system would obtain a lower torsional natural frequency than the industrial system. To further lower the natural frequencies, the inertia of the top platform is increased by the extra brass masses as shown in Figure 3.26. When there is a certain tension force in the wire ($f_{s,1} = 123$ Hz, $T = 64.6$ N), Figure 3.33 shows the frequency spectrums of the heavy-mass system and industrial isolator for translational vibrations.

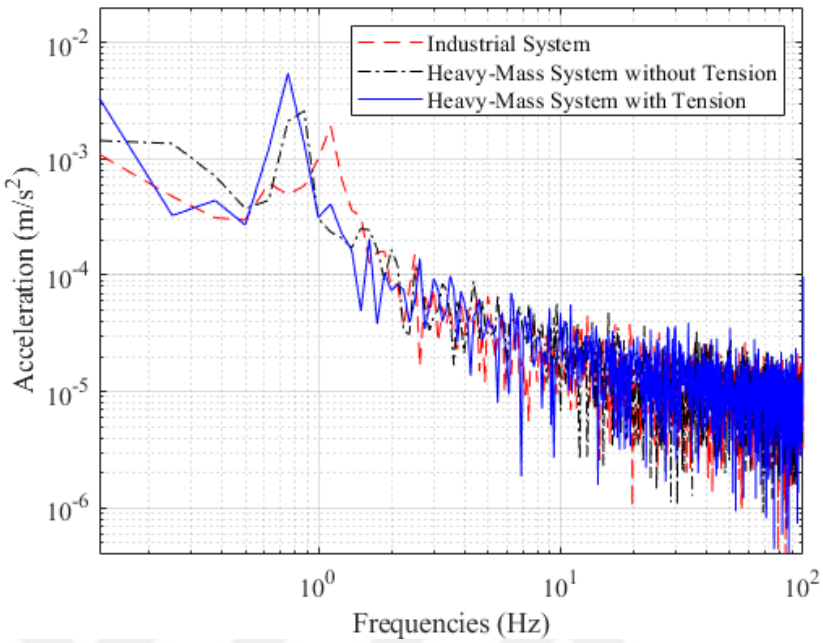

Figure 3.33. Experimental results of the translational frequency spectrums of the industrial-type isolator and the heavy-mass system when the tension force is applied to the heavy-mass system ($f_{s,1} = 123$ Hz, $T = 64.6$ N).

Similarly, Figure 3.34 shows the frequency spectrums of these systems for torsional vibrations. From Figures 3.33-3.34, it can be seen that a small increase in the tension force can reduce the translational and torsional natural frequencies of the heavy-mass system from 0.875 Hz to 0.750 Hz. While the translational natural frequencies of the heavy-mass system are lower than that of the industrial system in both cases, the torsional natural frequency of it has the same value with that of the industrial system. A further increase in the tension force would result in lower values for both natural frequencies.

Compared to the experimental results, the analytical model shows that when the same tension force is applied ($T = 64.6$ N), $\omega_{xy} = 1.09$ Hz and $\omega_{zz} = 0.950$ Hz. Hence, the experimental translational and torsional natural frequencies are found to be approximately 31 % and 21 % lower than their analytical counterparts, respectively. As explained in the previous case, the base and top platforms are assumed to be rigid in the analytical model,

which increases the natural frequencies. Despite this assumption, Figure 3.31-3.34 show that the tension mechanism can adjust the translational and torsional natural frequencies of the light and heavy-mass systems to very low values even if the payload mass (or the top platform mass in this case) changes.

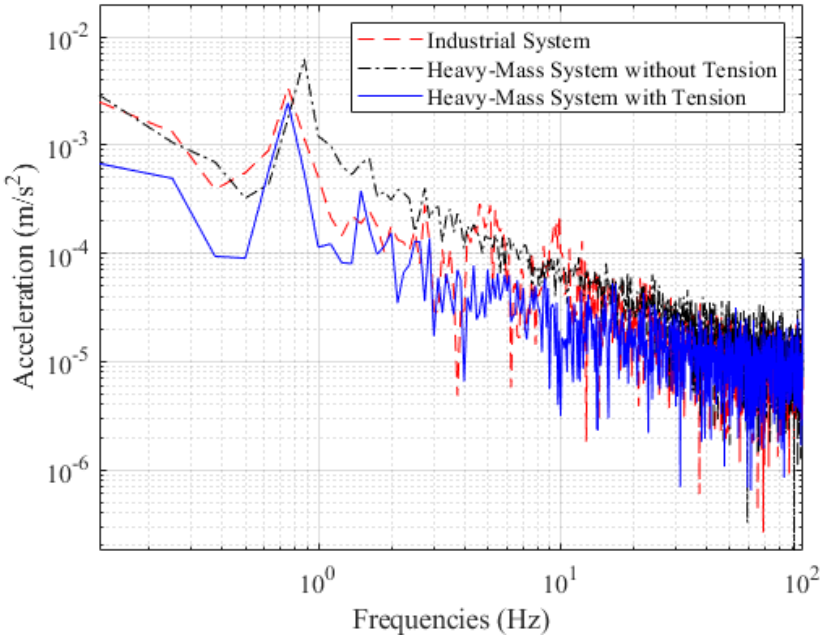

Figure 3.34. Experimental results of the torsional frequency spectrums of the industrial-type isolator and the heavy-mass system when the same tension force is applied to the light-mass system ($T = 64.6$ N).

For the light-mass and heavy-mass systems, the analytical and experimental values of ω_{xy} and ω_{zz} can be examined at different values of T. Figure 2.35 shows the comparison of the experimental ω_{xy} results obtained from the impact tests on the light-mass system with the analytical ω_{xy} results.

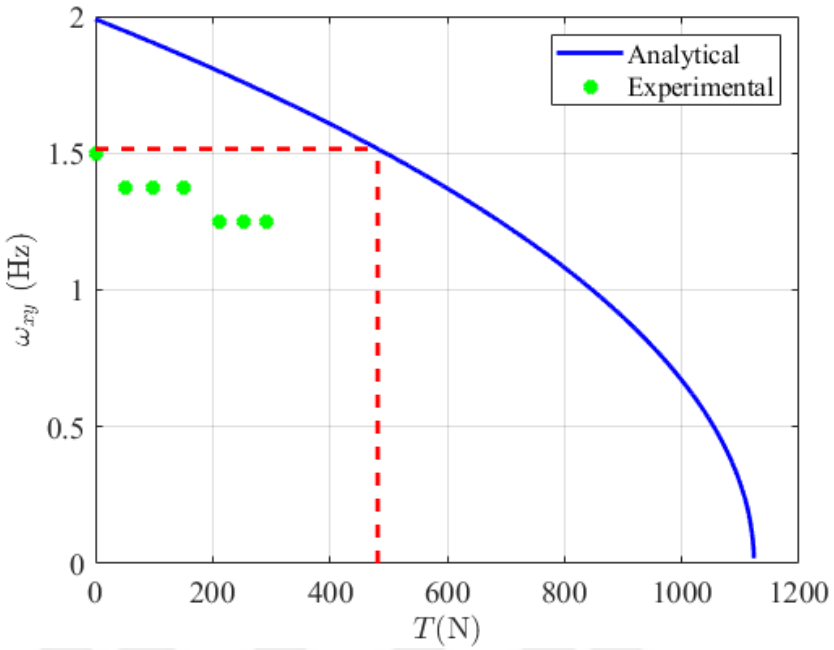

Figure 3.35. The comparison of the experimental ω_{xy} results obtained from the impact tests on the light-mass system with the analytical ω_{xy} results.

Similarly, Figure 3.36 shows the comparison of the experimental ω_{zz} results obtained from the impact tests on the light-mass system with the analytical ω_{zz} results. According to Figure 3.35 and Figure 3.36, it is seen that the experimental ω_{xy} and ω_{zz} values tend to decrease as the tension force T increases. In addition, the analytical ω_{xy} and ω_{zz} values are approximately 20 – 30 % larger than the experimental ω_{xy} and ω_{zz} values. As explained previously, since the base and top platforms are not rigid structures as assumed in the analytical models, the overall stiffness of the system is actually lower, leading to lower experimental results for ω_{xy} and ω_{zz} in the impact tests.

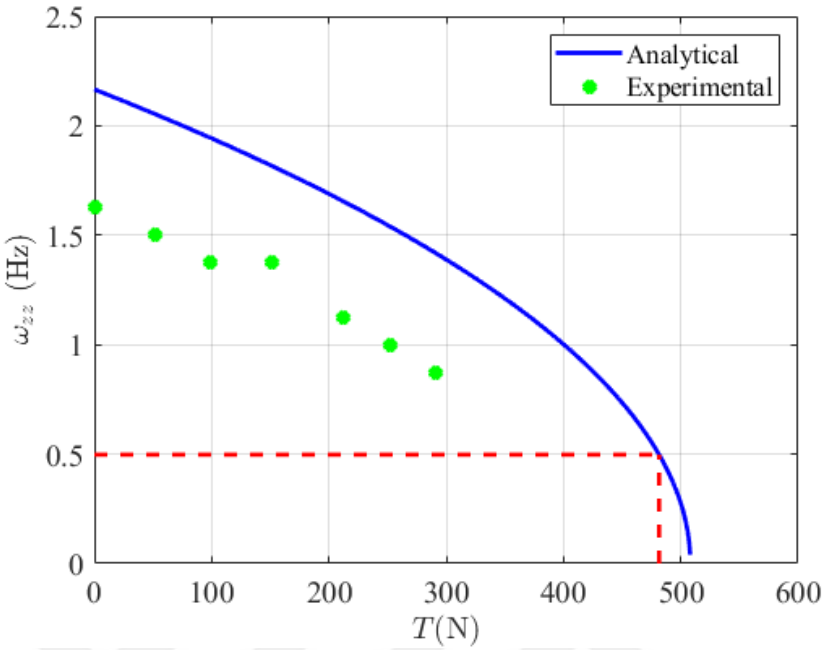

Figure 3.36. The comparison of the experimental ω_{zz} results obtained from the impact tests on the light-mass system with the analytical ω_{zz} results.

The similar observations can be made on the heavy-mass system. Figure 3.37 shows the comparison of the experimental ω_{xy} results obtained from the impact tests on the heavy-mass system with the analytical ω_{xy} results. Likewise, Figure 3.38 shows the same comparison for ω_{zz}. According to Figure 3.37 and Figure 3.38, the experimental ω_{xy} and ω_{zz} values decrease as the tension force T increases, and the analytical values are approximately 20 – 30 % larger than the experimental values for the heavy-mass system.

It is considered that the differences between the analytical and experimental results mainly stem from the assumptions made in the analytical model. Apart from the assumption that the base and top platforms are rigid, the assumption made on the boundary conditions of the beams may also lead to differences between the analytical and experimental values of ω_{xy} and ω_{zz}.

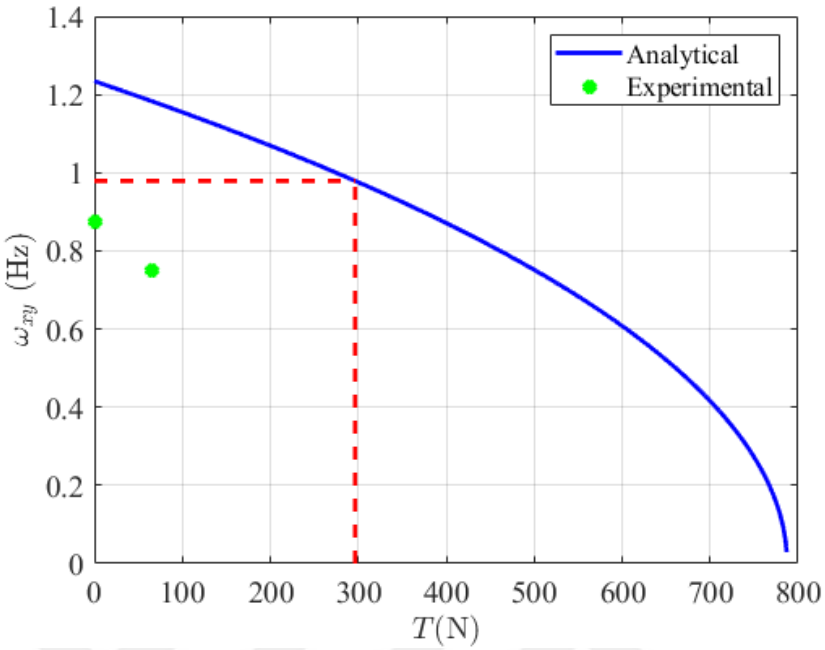

Figure 3.37. The comparison of the experimental ω_{xy} results obtained from the impact tests on the heavy-mass system with the analytical ω_{xy} results..

Although it is assumed in the analytical models that the mandrels are rigid structures, the experimental studies have shown that when the system vibrates under axial compressive loads, the mandrels flex slightly relative to the channel nuts to which they are fixed. For this reason, it is considered that the increased flexibility of the system decreases the experimental ω_{xy} and ω_{zz} values. Moreover, the factors such as beam curvature and eccentric loading of axial compressive forces on the beams, which are not taken into account in the analytical models, may lead to decreases in the actual values of $P_{cr,1}$, $T_{cr,xy}$ and $T_{cr,zz}$. Finally, it is considered that the measurement errors made in the natural frequency ($f_{s,1}$) estimations of the wire rope may result in these differences. In the experiments, since large deviations are observed in the measurements of $f_{s,1}$ values under the same conditions, the tension forces in the wire rope are averaged from the results obtained from Equation 2.71.

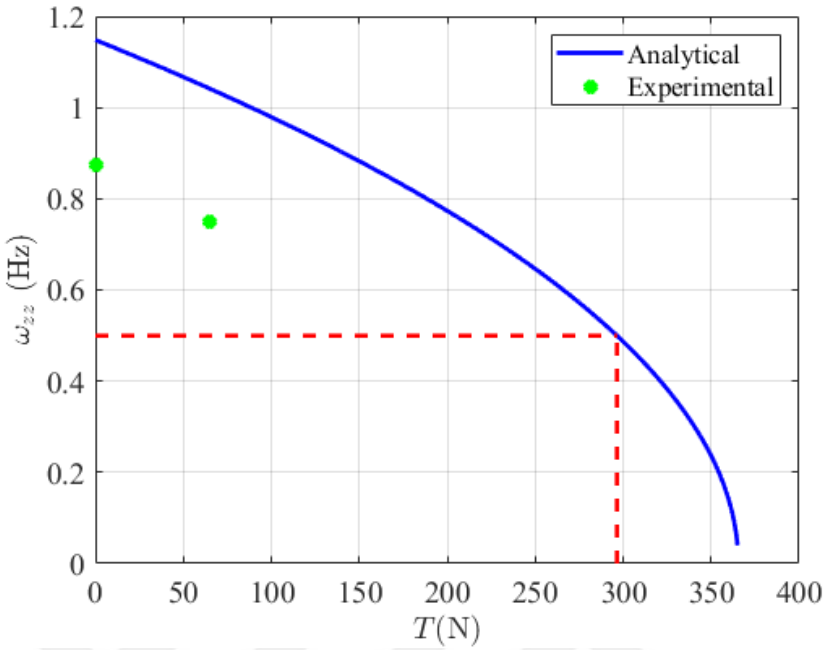

Figure 3.38. The comparison of the experimental ω_{zz} results obtained from the impact tests on the heavy-mass system with the analytical ω_{zz} results.

Despite all these reasons listed above, the test results obtained from Section 2.3 and Section 3.4 show that the translational and torsional stiffness of horizontal-motion isolators can be reduced to quasi-zero values even if they are under different loading conditions by adjusting their design parameters. As a result, compared to the existing industrial systems, the translational and torsional natural frequencies of the current design can be obtained at lower values when the wire tension and beam-slider mechanisms are used. Finally, the results also show that the isolation bandwidth of these isolators can be maximized when the middle part of the stepped beams are designed with thin-walled cylinders.

4. CONCLUSION

Analytical, numerical and experimental results show that depending on the payload being carried, the proposed wire tension and slide mechanisms can adjust the translational and torsional stiffness of horizontal vibration isolators to quasi-zero values. Therefore, even if the supported payload changes, the translational and torsional natural frequencies of the system can be kept at low and constant values, and the isolation performance of the system at low frequencies can be maintained along multiple axes. Moreover, in order to achieve the same isolation performance along translational axes, the beams must be designed with a circular cross-section.

The maximum payload mass that the system can support can be determined by calculating the critical buckling force of the system when the wire tension mechanism does not apply any force. In this case, the system achieves a quasi-zero-stiffness condition along translational axes. On the other hand, when the payload mass is below this maximum limit, the tension mechanism must be used to apply a certain force to the wire to bring the system into a quasi-zero stiffness condition along translational or torsional axes. When the tension mechanism is used, the buckling mode of the system may occur in two different modes. In the first mode, the system undergoes lateral buckling because the top platform only translates along horizontal directions. In the second mode, the system undergoes torsional buckling because the top platform only rotates about the central vertical axis of the system. Since the system may achieve a quasi-zero-stiffness condition under these buckling modes, the maximum value of this tension force is equal to the smaller of the critical values of the lateral and torsional buckling modes. These critical values can be defined as the lateral buckling tension and torsional buckling tension of the system.

Analytical and finite element models show that as the tension force is increased towards the lateral and torsional buckling tensions, the translational and torsional natural frequencies approach zero, respectively. However, if the difference between the lateral and torsional buckling tensions is large, the difference between these natural frequencies is also

large even if the maximum tension force enables the system to have a quasi-zero-stiffness condition along only translational or torsional axes. As a result, the isolation performance at low frequencies cannot be achieved at the same levels along multiple axes. For this reason, a slide mechanism is proposed to adjust the torsional natural frequency independently from the translational natural frequencies. This mechanism is used to adjust the distance of the beams from the central axis of the system. When axial compressive loads on the beams are not taken into account, an increase in the distance of the beams increases the torsional stiffness while reducing the torsional buckling tension. Thus, as the axial compressive loads on the beams increase from zero, the torsional natural frequency decreases from a larger initial value to zero more rapidly when the beams are positioned far from the center than when the beams are positioned close to the center. Under a given loading condition, if the torsional buckling tension is calculated to be considerably larger than the lateral buckling tension, the beams can be positioned further from the central axis to decrease the torsional buckling tension. If the opposite case occurs, the beams can be adjusted closer to the central axis. Therefore, when the tension mechanism is used with the slide mechanism, the natural frequencies of the system can be tuned more precisely to low values.

In order to maximize the isolation bandwidth of the system, the elastic stepped beams used in the constructed vibration isolators are created with a unique design; their thick middle parts are made of thin-walled cylinders with a larger outer radius than the lower and upper thin parts. In this way, the effective radius of gyration of the stepped beams with a hollow and thick middle part is larger than that of the stepped beams with a solid and thick middle part. When the radius of gyration is increased, the difference between the first and second bending natural frequencies of the beam also increases, resulting in a larger isolation bandwidth. The analytical models have shown that the system that is designed with stepped beams with a hollow and thick middle part has the largest isolation bandwidth for translational and torsional vibrations compared to the systems with uniform beams and stepped beams with a solid and thick middle part. Although the translational and torsional natural frequencies differ by some amount, the analytical and numerical frequency spectrums of the system have shown that the upper limit of the isolation bandwidth these two modes is the same, i.e., the first natural frequency of the stepped beam with clamped-clamped boundary conditions.

As the analytical models are validated by the finite element models and experimental studies, the optimization studies are performed to maximize the isolation bandwidth along multiple axes under several design constraints. In addition to determining the size of the system such as the height, length and width, the initial design constraint is to determine the maximum payload mass that the system can support. Considering most of the vibration isolation systems used in the industry, it is determined as 30 kg except the mass of the top platform. Moreover, it is also necessary to keep the maximum axial stress values in the beams and tension wire lower than their yield strengths of these members when the system is buckled using the tension mechanism and are exposed to a certain lateral deflection after being buckled. Since various beams and thin-walled cylinders purchased from the market are produced only in certain diameters, the genetic algorithm method is chosen to optimize the model. The advantage of this method over most optimization methods is that it allows the designer to find optimum parameters among a set of continuous and discrete variables. When the final system is constructed with these optimum design parameters, analytical, numerical and experimental results show that the system can have translational and torsional natural frequencies adjusted between 0.5 Hz and 1.5 Hz under any loading condition. Although the natural frequencies can be decreased further, they should be kept above 0.5 Hz in order for the system to maintain its elastic stability. Furthermore, the analytical and numerical results show that the system can achieve very large isolation bandwidths for translational and torsional vibrations. For instance, it is obtained analytically that $\omega_{xy}/\omega_u = 1.515/378.4 = 0.0040$ and $\omega_{zz}/\omega_u = 0.4930/378.4 = 0.0013$. Hence, the isolation bandwidth starts at $\sqrt{2}\omega_{xy}$=2.14 Hz and extends up to ω_u= 378.4 Hz for translational vibrations while the isolation bandwidth starts at $\sqrt{2}\omega_{zz}$=0.697 Hz and extends up to ω_u= 378.4 Hz for torsional vibrations. Since $\omega_{zz}/\omega_u < \omega_{xy}/\omega_u$, the system has a better isolation performance for torsional vibrations. Therefore, the proposed wire tension and slide mechanisms can be used in horizontal vibration isolators that protect vibration-sensitive mechanical, optical and electronic measuring devices used in industrial activities and laboratory studies in order to adjust their stiffness with respect changing payload weights.

REFERENCES

1. Barton, M. A., N. Kanda and K. Kuroda, “A low-frequency vibration isolation table using multiple crossed-wire suspensions”, *Review of Scientific Instruments*, Vol. 67, No. 11, pp. 3994–3999, 1996.

2. Liu, J., L. Ju and D. G. Blair, “Vibration isolation performance of an ultra-low frequency folded pendulum resonator”, *Physics Letters, Section A: General, Atomic and Solid State Physics*, Vol. 228, No. 4-5, pp. 243–249, 1997.

3. Chin, E. J., K. T. Lee, J. Winterflood, L. Ju and D. G. Blair, “Low frequency vertical geometric anti-spring vibration isolators”, *Physics Letters, Section A: General, Atomic and Solid State Physics*, Vol. 336, No. 2-3, pp. 97–105, 2005.

4. Garoi, F., J. Winterflood, L. Ju, J. Jacob and D. G. Blair, “Passive vibration isolation using a Roberts linkage”, *Review of Scientific Instruments*, Vol. 74, No. 7, pp. 3487–3491, 2003.

5. Takamori, A., P. Raffai, S. M´arka, R. DeSalvo, V. Sannibale, H. Tariq, A. Bertolini, G. Cella, N. Viboud, K. Numata, R. Takahashi and M. Fukushima, “Inverted pendulum as low-frequency pre-isolation for advanced gravitational wave detectors”, *Nuclear Instruments and Methods in Physics Research, Section A: Accelerators, Spectrometers, Detectors and Associated Equipment*, Vol. 582, No. 2, pp. 683–692, 2007.

6. Barton, M. A., T. Uchiyama, K. Kuroda, N. Kanda and H. Ishizuka, “Twodimensional X pendulum vibration isolation table”, *Review of Scientific Instruments*, Vol. 70, No. 4, pp. 2150–2154, 1999.

7. Winterflood, J., D. G. Blair and B. Slagmolen, “High performance vibration isolation using springs in Euler column buckling mode”, *Physics Letters, Section A: General, Atomic and Solid State Physics*, Vol. 300, No. 2-3, pp. 122–130, 2002.

8. Platus, D. L., “Negative-stiffness-mechanism vibration isolation systems”, *Optomechanical Engineering and Vibration Control*, Vol. 3786, No. September 1999, pp. 98–105, 1999.

9. Ibrahim, R. A., “Recent advances in nonlinear passive vibration isolators”, *Journal of Sound and Vibration*, Vol. 314, No. 3-5, pp. 371–452, 2008.

10. Araki, Y., T. Asai, K. Kimura, K. Maezawa and T. Masui, “Nonlinear vibration isolator with adjustable restoring force”, *Journal of Sound and Vibration*, Vol. 332, No. 23, pp. 6063–6077, 2013.

11. Tang, B. and M. J. Brennan, “On the shock performance of a nonlinear vibration isolator with high-static-low-dynamic-stiffness”, *International Journal of Mechanical Sciences*, Vol. 81, pp. 207–214, 2014.

12. Ho, C., Z. Q. Lang and S. A. Billings, “Design of vibration isolators by exploiting the beneficial effects of stiffness and damping nonlinearities”, *Journal of Sound and Vibration*, Vol. 333, No. 12, pp. 2489–2504, 2014.

13. Francisco Ledezma-Ramirez, D., N. S. Ferguson, M. J. Brennan and B. Tang, “An experimental nonlinear low dynamic stiffness device for shock isolation”, *Journal of Sound and Vibration*, Vol. 347, pp. 1–13, 2015.

14. Yan, B., H. Ma, C. Zhao, C. Wu, K. Wang and P. Wang, “A vari-stiffness nonlinear isolator with magnetic effects: Theoretical modeling and experimental verification”, *International Journal of Mechanical Sciences*, Vol. 148, No. 928, pp. 745–755, 2018.

15. Alabuzhev, P., A. Gritchin, L. Kim, G. Migirenko, V. Chon and P. Stepanov, *Vibration Protecting and Measuring Systems with Quasi-Zero Stiffness*, Hemisphere Publishing Corporation, 1989.

16. Carrella, A., M. J. Brennan, T. P. Waters and K. Shin, “On the design of a high- 9 static-low-dynamic stiffness isolator using linear mechanical springs and magnets”, *Journal of Sound and Vibration*, Vol. 315, No. 3, pp. 712–720, 2008.

17. Hoque, M. E., T. Mizuno, Y. Ishino and M. Takasaki, “A three-axis vibration isolation system using modified zero-power controller with parallel mechanism technique”, *Mechatronics*, Vol. 21, No. 6, pp. 1055–1062, 2011.

18. Sun, X., J. Xu, X. Jing and L. Cheng, “Beneficial performance of a quasi-zero-stiffness vibration isolator with time-delayed active control”, *International Journal of Mechanical Sciences*, Vol. 82, pp. 32–40, 2014.

19. Xu, J. and X. Sun, “A multi-directional vibration isolator based on Quasi-Zero-Stiffness structure and time-delayed active control”, *International Journal of Mechanical Sciences*, Vol. 100, pp. 126–135, 2015.

20. Zhu, T., B. Cazzolato, W. S. Robertson and A. Zander, “Vibration isolation using six degree-of-freedom quasi-zero stiffness magnetic levitation”, *Journal of Sound and Vibration*, Vol. 358, pp. 48–73, 2015.

21. Liu, S., L. Feng, D. Zhao, X. Shi, Y. Zhang, J. Jiang, Y. Zhao, C. Zhang and L. Chen, “A real-time controllable electromagnetic vibration isolator based on magnetorheological elastomer with quasi-zero stiffness characteristic”, *Smart Materials and Structures*, Vol. 28, No. 8, 2019.

22. Zhu, T., B. Cazzolato, W. Robertson and A. Zander, “The development of a 6 degree of freedom quasi-zero stiffness maglev vibration isolator with adaptive-passive load support”, *15th International Conference on Mechatronics Technology*, 2011.

23. Wang, Y., S. Li, C. Cheng and Y. Su, “Adaptive control of a vehicle-seat-human 10 coupled model using quasi-zero-stiffness vibration isolator as seat suspension”, *Journal of Mechanical Science and Technology*, Vol. 32, No. 7, pp. 2973–2985, 2018.

24. Sadeghi, S. and S. Li, “Fluidic origami cellular structure with asymmetric quasizero stiffness for low-frequency vibration isolation”, *Smart Materials and Structures*, Vol. 28, No. 6, 2019.

25. Karnopp, D., “Active and semi-active vibration isolation”, *Journal of Mechanical Design, Transactions of the ASME*, Vol. 117, No. B, pp. 177–185, 1995.

26. Kovacic, I., M. J. Brennan and T. P. Waters, “A study of a nonlinear vibration isolator with a quasi-zero stiffness characteristic”, *Journal of Sound and Vibration*, Vol. 315, No. 3, pp. 700–711, 2008.

27. Lan, C. C., S. A. Yang and Y. S. Wu, “Design and experiment of a compact quasi-zero-stiffness isolator capable of a wide range of loads”, *Journal of Sound and Vibration*, Vol. 333, No. 20, pp. 4843–4858, 2014.

28. Zhao, F., J. Ji, K. Ye and Q. Luo, “An innovative quasi-zero stiffness isolator with three pairs of oblique springs”, *International Journal of Mechanical Sciences*, Vol. 192, p. 106093, 2021.

29. Dao, P. T. and S. Huang, “A compact quasi-zero stiffness vibration isolator using flexure- based spring mechanisms capable of tunable stiffness”, *International Journal of Mechanical and Mechatronics Engineering*, Vol. 10, No. 8, pp. 1565–1574, 2016.

30. Zhou, J., X. Wang, D. Xu and S. Bishop, “Nonlinear dynamic characteristics of a quasi-zero stiffness vibration isolator with cam-roller-spring mechanisms”, *Journal of Sound and Vibration*, Vol. 346, No. 1, pp. 53–69, 2015.

31. Ye, K., J. C. Ji and T. Brown, “Design of a quasi-zero stiffness isolation system for supporting different loads”, *Journal of Sound and Vibration*, Vol. 471, pp. 1–21, 11 2020.

32. Ye, K., J. C. Ji and T. Brown, “A novel integrated quasi-zero stiffness vibration isolator for coupled translational and rotational vibrations”, *Mechanical Systems and Signal Processing*, Vol. 149, p. 107340, 2021.

33. Zhang, Q., S. Xia, D. Xu and Z. Peng, “A torsion–translational vibration isolator with quasi-zero stiffness”, *Nonlinear Dynamics*, Vol. 99, No. 2, pp. 1467–1488, 2020.

34. Plaut, R. H., H. M. Favor, A. E. Jeffers and L. N. Virgin, “Vibration isolation using buckled or pre-bent columns – Part 1: Two-dimensional motions of horizontal rigid bar”, *Journal of Sound and Vibration*, Vol. 310, No. 1-2, pp. 409–420, 2008.

35. Jeffers, A. E., R. H. Plaut and L. N. Virgin, “Vibration isolation using buckled or pre-bent columns – Part 2: Three-dimensional motions of horizontal rigid plate”, *Journal of Sound and Vibration*, Vol. 310, No. 1-2, pp. 421–432, 2008.

36. Liu, X., X. Huang and H. Hua, “On the characteristics of a quasi-zero stiffness isolator using Euler buckled beam as negative stiffness corrector”, *Journal of Sound and Vibration*, No. 14, pp. 3359–3376, 2013.

37. Robertson, W. S., M. R. Kidner, B. S. Cazzolato and A. C. Zander, “Theoretical design parameters for a quasi-zero stiffness magnetic spring for vibration isolation”, *Journal of Sound and Vibration*, Vol. 326, No. 1-2, pp. 88–103, 2009.

38. Xu, D., Q. Yu, J. Zhou and S. R. Bishop, “Theoretical and experimental analyses of a nonlinear magnetic vibration isolator with quasi-zero-stiffness characteristic”, *Journal of Sound and Vibration*, Vol. 332, No. 14, pp. 3377–3389, 2013.

39. Zheng, Y., X. Zhang, Y. Luo, B. Yan and C. Ma, “Design and experiment of a highstatic-low-dynamic stiffness isolator using a negative stiffness magnetic spring”, *Journal of Sound and Vibration*, Vol. 360, pp. 31–52, 2016.

40. Sun, X. and X. Jing, “Multi-direction vibration isolation with quasi-zero stiffness by employing geometrical nonlinearity”, *Mechanical Systems and Signal Processing*, Vol. 62, pp. 149–163, 2015.

41. Fulcher, B. A., D. W. Shahan, M. R. Haberman, C. C. Seepersad and P. S. Wilson, “Analytical and experimental investigation of buckled beams as negative stiffness elements

for passive vibration and shock isolation systems", *Journal of Vibration and Acoustics*, Transactions of the ASME, Vol. 136, No. 3, pp. 1–12, 2014.

42. Acar, M. A. and C. Yilmaz, "Design of an adaptive-passive dynamic vibration absorber composed of a string-mass system equipped with negative stiffness tension adjusting mechanism", *Journal of Sound and Vibration*, Vol. 332, No. 2, pp. 231–245, 2013.

43. Lang, Z. Q., X. J. Jing, S. A. Billings, G. R. Tomlinson and Z. K. Peng, "Theoretical study of the effects of nonlinear viscous damping on vibration isolation of sdof systems", *Journal of Sound and Vibration*, Vol. 323, No. 1-2, pp. 352–365, 2009.

44. Le, T. D. and K. K. Ahn, "A vibration isolation system in low frequency excitation region using negative stiffness structure for vehicle seat", *Journal of Sound and Vibration*, Vol. 330, No. 26, pp. 6311–6335, 2011.

45. Le, T. D. and K. K. Ahn, "Experimental investigation of a vibration isolation system using negative stiffness structure", *International Journal of Mechanical Sciences*, Vol. 2013, pp. 99–112, 2013.

46. Shen, Y., H. Peng, X. Li and S. Yang, "Analytically optimal parameters of dynamic vibration absorber with negative stiffness", *Mechanical Systems and Signal Processing*, Vol. 85, pp. 193–203, 2017.

47. Palomares, E., A. J. Nieto, A. L. Morales, J. M. Chicharro and P. Pintado, "Numerical and experimental analysis of a vibration isolator equipped with a negative stiffness system", *Journal of Sound and Vibration*, Vol. 414, pp. 31–42, 2018.

48. Wu, Z., X. Jing, B. Sun and F. Li, "A 6DOF passive vibration isolator using X-shape supporting structures", *Journal of Sound and Vibration*, Vol. 380, pp. 90–111, 2016.

49. Zhou, J., K. Wang, D. Xu, H. Ouyang and Y. Li, "A six degrees-of-freedom vi- 13 bration isolation platform supported by a hexapod of quasi-zero-stiffness struts", *Journal of Vibration and Acoustics, Transactions of the ASME*, Vol. 139, No. 3, pp. 1–5, 2017.

50. Zhou, J., Q. Xiao, D. Xu, H. Ouyang and Y. Li, “A novel quasi-zero-stiffness strut and its applications in six-degree-of-freedom vibration isolation platform”, *Journal of Sound and Vibration*, Vol. 394, pp. 59–74, 2017.

51. Hu, F. and X. Jing, “A 6-DOF passive vibration isolator based on Stewart structure with X-shaped legs”, *Nonlinear Dynamics*, Vol. 91, No. 1, pp. 157–185, 2018.

52. Minus K. Techonology, Inc., Inglewood, CA (US), BM-8 Bench Top Vibration Isolation Platform, 2009, https://www.minusk.com/documents/specsheets/bm1specsheetvibration isolationsystemsantivibrationtable.pdf, accessed in January 2021.

53. Platus, D. L., “*Vibration Isolation Systems*”, U.S. Patent 2014/0048989 A1, February 20, 2014.

54. Timoshenko, S., *Vibration Problems in Engineering*, D. Van Nostrand Company, Inc., 2 edn., 1937.

55. Timoshenko, S. P. and J. M. Gere, *Theory Of Elastic Stability*, McGRaw-Hill International Book Company, 2 edn., 1985.

56. Herzan, Laguna Hills, CA (US), ONYX ® Series, 2019, https://www.herzan.com/wp-content/uploads/2019/04/Onyx-Series-Data-Sheet.pdf, accessed in February 2021.

57. Herzan, Laguna Hills, CA (US), NDW Series Data Sheet, 2020, https://www.herzan.com/wp-content/uploads/2020/09/NDW-Series-Product-Guide.pdf, accessed in February 2021.